Thesis Title

Assessing opportunities for water savings in large-scale pressurized irrigation systems using actual evapotranspiration retrieved by surface energy balance and remotely sensed data

HASSAN AWADA

Tutor

Prof. Ing. Giuseppe Ciraolo

Dipartimento di Ingegneria Civile, Ambientale, Aerospaziale, dei Materiali—DICAM, Università degli Studi di Palermo, Viale delle Scienze, Bld. 8, 90128 Palermo, Italy

Co-Tutors

Prof. Ing. Giuseppe Provenzano

Dipartimento Scienze Agrarie, Alimentari e Forestali (SAAF), Università degli Studi di Palermo, Viale delle Scienze, Bld. 4, 90128 Palermo, Italy

Ing. Antonino Maltese

Dipartimento di Ingegneria Civile, Ambientale, Aerospaziale, dei Materiali—DICAM, Università degli Studi di Palermo, Viale delle Scienze, Bld. 8, 90128 Palermo, Italy

UNIVERSITÀ DEGLI STUDI DI PALERMO

DIPARTIMENTO DI INGEGNERIA CIVILE, AMBIENTALE, AEROSPAZIALE, DEI MATERIALI

DOTTORATO DI RICERCA IN INGEGNERIA CIVILE, AMBIENTALE, DEI MATERIALI

Settore Scientifico Disciplinare ICAR/02

ASSESSING OPPORTUNITIES FOR WATER SAVINGS IN LARGE-SCALE PRESSURIZED IRRIGATION SYSTEMS USING ACTUAL EVAPOTRANSPIRATION RETRIEVED BY SURFACE ENERGY BALANCE AND REMOTELY SENSED DATA

Dottorando
Ing. Hassan Awada

Coordinatore
Ch.ma Prof. Antonina Pirrotta

Tutor
Prof. Ing. Giuseppe Ciraolo

Co-Tutors
Prof. Ing. Giuseppe Provenzano
Ing. Antonino Maltese

CICLO XXX
A.A. 2016/2017

بِسْمِ اللَّهِ الرَّحْمَٰنِ الرَّحِيمِ

WE MADE FROM WATER EVERY

LIVING THING

صَدَقَ اللهُ العَلِيُّ العَظيم

Acknowledgments

This research was developed in the framework of a doctoral thesis conducted at the University of Palermo (Italy). The author would like to express his gratitude to the Department of Civil, Environmental, Aerospatial, Material Engineering of the University of Palermo, Italy, to the Regional Center for Water Research (CREA) of the University of Castilla-La Mancha, Spain. All gratitude to whom together made this research work possible; great thanks to Professors Miguel Angel Moreno, Giuseppe Provenzano, and Engineers Antonino Maltese, Fulvio Capodici and Juan Ignacio Còrcoles for the valuable assistance provided during all phases the research.

I would also acknowledge all those who have made possible the completion of the present work and in particular to Prof. Goffredo La Loggia, Director of the department to whom is addressed my gratitude. I sincerely thank my supervisor Prof. Eng. Giuseppe Ciraolo, for his supervision, advices, and guidance in all stages of this research thesis.

This thesis is dedicated to my family and especially to my father Ali Awada and my beloved wife Giusy Malta for their support, encouragement and constant love, that has sustained me throughout my life and my stay in Italy. Any of the success I may achieve in my life could not be possible without you.

Abstract:

Remote sensing allows the observation of large land stretches and the acquisition of worthwhile information that can be used efficaciously in agro-hydrologic systems. Satellite imagery associated to computational models provide a reliable resource in estimating evapotranspiration (*ET*) fluxes based on surface energy balance. On irrigated crops, quantifying the spatial distribution of actual *ET* enables a broad range of applications such as irrigation management, monitoring water distribution, assessing crop water status and irrigation system performance.

The general objective of the research was to propose a methodology to estimate *ET* by using Landsat Thematic Mapper (TM) images and surface energy balance (SEB) models, thus allowing the monitoring of current irrigation practices and crop water status. The proposed methodology was applied in the irrigation district of ‘‘SAT Llano Verde’’, Albacete, Castilla-La Mancha (Spain) characterized by annual horticultural crops, for irrigation seasons (from May to September) 2006, 2007 and 2008, as well as in the irrigation district 1/A, managed by “Consorzio di Bonifica Agrigento 3”, Castelvetrano, Sicily (Italy), characterized by sparse perennial vegetation (mainly olives and grape vines) during irrigation seasons 2009 and 2010.

Two satellite-based image-processing SEB models were used for estimating actual *ET*, i.e., the single source Surface Energy Balance Model for Land (SEBAL) and the Two-source Surface Energy Balance model (TSEB). The first model was applied on both case studies, while the second was applied only to the Italian case study, because of its suitability to sparse vegetation. The models were applied to quantify instantaneously, daily, monthly and seasonal actual *ET* over the available TM cloud-free images.

Successful applications of SEBAL model provided direct estimations of the spatial distribution of the main energy fluxes, at the instant of the satellite overpass. Daily Evapotranspiration values ($ET_{a,ID}$) were obtained from instantaneous values by assuming an invariable evaporative fraction for the entire day of acquisition. Monthly and seasonal ET values were then estimated from $ET_{a,ID}$, by assuming that the latter varies in

proportion to the reference evapotranspiration (ET_0) based on the data acquired by meteorological stations located in both the study-areas. In this way it was possible to account for day to day variations in meteorological forcing.

In the case of the SAT Llano Verde irrigation district, the model application allowed the comparison between the monthly water volumes distributed by each hydrant, as measured, with the corresponding actual evapotranspiration volumes, taking into account a value of irrigation efficiency equal to 85%, as indicated by the district irrigation management. This comparison allowed assessing the irrigation performance at both hydrant level and the whole irrigation district. It was shown that the majority of farmers use to apply amounts of water higher than those retrieved by SEBAL, with the exception of May in all investigated years, in which a significant amount of precipitation occurred. The comparison at seasonal time-scale evidenced that a considerable amount of water could have been saved, corresponding to 26.2, 28.0 and 16.4 % of total water consumption, evaluated respectively for years 2006, 2007 and 2008.

On the other hand, the application of TSEB did not provide convincing results due to several factors, among which I believe the high sensitivity of this method to uncertainties in satellite radiometric temperature retrievals, as well as to the additional input parameters required to run the model.

In the irrigation district 1/A (Italy) the actual *ET* fluxes retrieved by SEBAL were also compared to the corresponding estimated by the eddy covariance tower located in an olive orchard within the district. The comparison evidenced the general reliability of daily *ET* retrieved by the model and consequently the validity of the self-preservation hypothesis applied to upscale instantaneous *ET* values.

However, the temporal upscaling between acquisition dates strongly depended on the number of cloud-free available images and, mainly in the Italian case-study, failed to take into account preceding and succeeding rainfall and/or irrigation events. Finally, the comparison between SEBAL outputs and the maximum daily crop evapotranspiration (ET_c) estimated with the FAO 56 Penman-Monteith approach for the

image acquisition days, evidenced remarkable stress levels on both the investigated crops, with the exception of May during which significant rainfall events occurred in both the considered years.

Keywords: Remote sensing, surface energy balance, actual evapotranspiration, irrigation, water saving, Irrigation monitoring, crop water status.

في حالة منطقة الري الأسبانية، سمح التطبيق بمقارنة الكميات الشهرية للمياه الموزعة بواسطة كل صنبور مع كميات التبخر الفعلية المقابلة، مع الأخذ بعين الاعتبار قيمة كفاءة الري التي تساوي 85٪ كما هو مبين في إدارة الري. وقد سمحت هذه المقارنة بتقييم أداء الري علي صعيد المنطقة المروية بأكملها وعلى صعيد المساحة المروية بواسطة كل صنبور. وقد تبين أن أغلبية المزارعين يستخدمون كميات من المياه أعلى من تلك التي تم إحتسابها بواسطة النموزج سيبال، باستثناء شهر مايو في جميع السنوات التي تم التحقيق فيها، والتي حدثت فيها كمية كبيرة من الأمطار. وأظهرت المقارنة على نطاق زمني موسمي أنه كان من الممكن توفير كمية كبيرة من المياه ، أي ما يعادل 26.2 و 28.0 و 16.4 في المائة من إجمالي استهلاك المياه، في السنوات 2006 و 2007 و2008 على التوالي.

من ناحية أخرى، لم يقدم تطبيق نموزج تيسب نتائج مقنعة بسبب عدة عوامل، من بينها حساسية النموزج العالية من أي خطأ بسيط أو عدم اليقين في استنتاج درجة الحرارة الإشعاعية المستشعرة عن بعد ، فضلا عن المعلومات و المدخلات الإضافية اللازمة لتشغيل النموذج.

وفي منطقة الري 1/A (إيطاليا)، تمت مقارنة كميات التبخر الفعلية التي تم تقديرها بواسطة سيبال بالتبخرالذي تم تقديره ببرج التغاير الدوامي (Eddy Covariance Tower) الموجود في بستان الزيتون داخل المنطقة المدروسة .أثبتت هذه المقارنة الموثوقية العامة لكميات التبخر اليومية التي تم تقديرها من قبل النموذج، كما اثبتت صحة فرضية ثبوت العامل التبخري المستخدمة في تحصيل قيم التبخر الفعلي اليومي من القيم اللحظية.

ومع ذلك، فإن التقدير الزماني لكميات التبخر بين تواريخ إلتقاط الصور الجوية تعتمد بشدة على عدد الصور المتاحة الخالية من السحاب، ولا سيما في دراسة الحالة الإيطالية، بحيث أن المنهجية فشلت في مراعاة أحداث هطول الأمطار و الري السابقة واللاحقة ليوم إلتقاط الصور الجوية بسبب محدودية كمية الصور المتاحة للإستخدام. وأخيرا، تمت المقارنة بين نواتج سيبال والحد الأقصى من التبخر اليومي للمحصول (ET_0) لأيام إلتقاط الصور الجوية الذي تم تقديره بطريقة بنمان-مونتيث (FAO 56 Penman-Monteith) حسب توصيات منظمة الأغذية والزراعة. أظهرت المقارنة ، مستويات إجهاد ملحوظة على كل من المحاصيل في منطقة الدراسة، باستثناء شهر مايو بحيث سجلت كمية أمطار يعتد بها في كل من السنتان الموضوعتين تحت الدراسة.

الكلمات المفتاحية: الاستشعار عن بعد، توازن الطاقة السطحية، التبخر الفعلي، الري، توفير المياه، مراقبة الري، وتقييم الاستهلاك المائي للمحاصيل.

نبذة مختصرة:

تتيح تقنيات الاستشعار عن بعد رصد مساحات كبيرة من الأراضي والحصول على معلومات جديرة بالاهتمام ويمكن استخدامها بكفاءة في النظم الزراعية الهيدرولوجية. توفر صور الأقمار الصناعية المرتبطة بالنماذج الحسابية موردا موثوقا به في تقدير تدفقات التبخر التي تستند إلى توازن الطاقة السطحية. فيما يتعلق بالمحاصيل المروية، فإن القياس الكمي للتوزيع المكاني لكمية التبخر الفعلي يتيح مجموعة واسعة من التطبيقات مثل إدارة الري، و مراقبة توزيع المياه، وتقييم الحالة المائية للمحاصيل ، وتقييم أداء أنظمة الري.

إن الهدف العام من هذا البحث هو اقتراح منهجية لتقدير كميات التبخر باستخدام الصور الملتقطة عبر المستشعرات ثيماتيك مابر (Thematic Mapper) المحمولة على القمر الصناعي لاندسات (Landsat TM) ، مصحوبة بنماذج توازن الطاقة السطحية، مما يسمح بمراقبة ممارسات الري الحالية وتقييم الاستهلاك المائي للمحاصيل. تم تطبيق المنهجية المقترحة في منطقة الري في 'سات لانو فيردي'، الباسيتي ، كاستيلا-لا مانتشا (إسبانيا) التي تتميز بمحاصيل البستنة الحولية، خلال مواسم الري (من مايو إلى سبتمبر) 2006 و 2007 و 2008، وكذلك تم التطبيق في منطقة الري 1/A التي يديرها "كونسورزيو دي بونيفيكا أغريجينتو 3"، كاستلفترانو، صقلية (إيطاليا) والتي تتميز بالنباتات الدائمة (الزيتون والكروم العنب) خلال مواسم الري 2009 و 2010 .

وقد استخدم نموذجان من النماذج التي تعتمد أساسا على معادلة موازنة الطاقة على الأرض لمعالجة صورالأقمار الإصطناعية وتقدير كميات التبخر الفعلي . النموزج الأول هو نموذج توازن الطاقة السطحية للأرض سيبال (SEBAL) الذي يتعامل مع البيكسل على أنها سطح متجانس، أما النموذج الثاني هو نموزج توازن الطاقة السطحية ذي المصدرين تيسب (TSEB) الذي يتعاما مع المكونات المختلفة داخل البيكسل.

تم تطبيق النموزج الاول على منطقتي البحث في إيطاليا وإسبانيا أما النموذج الثاني فقط تم تطبيقه فقط في الحالة الإيطالية، بسبب ملاءمة النموزج للتطبيق على الغطاء النباتي المتناثر. وقد طبقت النماذج لتقديرالتبخر الفعلي اللحظي واليومي والشهري والفصلي بإستخدام الصور الفضائية الخالية من السحاب والتي تم الحصول عليها بواسطة مستشعرات الأقمار الصناعية. وقد وفرت التطبيقات الناجحة لنموذج سيبال تقديرات لحظية ومباشرة للتوزيع المكاني لتدفقات الطاقة الرئيسية وبالتالي الحصول على قيمة التبخرالفعلي لحظة إلتقاط الصور الجوية . بعد ذالك تم تقدير كميات التبخر اليومية من القيمة اللحظية تحت فرضية ثبوت العامل التبخري خلال يوم إلتقاط الصور الجوية . أما قيمة التبخر الشهري والموسمي فتم حسابها أستناداً لفرضية أن التبخر في يوم إلتقاط الصورة الجوية يتبع نسق التغيرات في *التبخر*- نتح *المرجعي* التي تم الحصول عليها من قبل محطات الأرصاد الجوية الموجودة في كل من المنطقتين الموضوعتين تحت الدراسة.

List of Figures

List of Tables

Chapter 1: Introduction and Background

1.1 Problematic and Overview

1.1.1 Irrigated Agriculture, Water and Energy

Water is among the most valuable natural Earth resources. Water resources are becoming increasingly insufficient in meeting the current water demand. Agriculture accounts for 70% of total global freshwater withdrawals and represents the largest user of fresh water. Shortly, it is estimated that the total global water withdrawals for irrigation purposes are projected to increase by 10% by 2050 (FAO, 2011). An integrated and rational management of water resources must be considered a priority; indeed in this context, and especially in arid regions, irrigated agriculture is particularly vulnerable, due to high water demands and

contextual water scarcity. Crop water requirements have to be determined accurately, taking into account water availability, land size, irrigation systems, and crop productivity (Rinaldi and He, 2014). In southern Europe and in Mediterranean countries, characterized by semi-arid or arid climate, irrigation agencies and water users associations are being questioned about the current levels of water use efficiency, and are continuously asked to improve the performance of irrigation conveyance and delivery systems (D'Urso, 2001).

Improvement of water use efficiency in irrigated agriculture, from engineering and agronomic aspects, can be addressed by quantifying the products production per unit of water applied (Howell et al., 2001). A more efficient use of water for agricultural purposes would undoubtedly lead to save both water and energy. A reduction of the energy bill in agriculture can be primarily achieved through a contextual reduction of irrigation water use; accordingly, Khadra et al. (2016) showed that the adoption of reliable, integrated and efficient irrigation approaches could build synergies between water and energy use. Irrigation water and energy interactions are complex; a rational, integrated management of natural resources should consider the dynamic and interrelated nexus between water and energy. The first trade-off between water and energy can lead to more efficient energy practices, since energy is required in agricultural applications, such as water pumping, transporting, extracting, collecting, discharging and treating applications.

1.1.2 Evapotranspiration and Remote Sensing of land surface

Evapotranspiration (*ET*) represents the key variable in linking ecosystem functioning, carbon and climate feedbacks, agricultural management, and water resources (Fisher et al., 2017). Modeling *ET* has many applications in agricultural water management. Land-surface *ET* represents one of the primary components of the hydrologic cycle; its accurate estimation is mandatory to optimize agricultural water management. Water managers and policymakers, with the aim to optimize irrigation management, need to dispose of accurate estimations of the real (actual) water volumes to apply with irrigation (Droogers et al., 2010). Usually, for irrigation purposes, crop evapotranspiration is computed by conventional methods based on meteorological data: commonly collected meteorological data are used to compute reference evapotranspiration (ET_0) and then

maximum crop evapotranspiration (ET_c), that is estimated by using site-specific crop coefficients. Toureiro et al. (2017) showed that remote sensing based methodologies can estimate actual evapotranspiration with an easier approach and at a lower cost if compared to the traditional crop coefficient method recommended by FAO. Better estimations of *ET* can certainly contribute to reducing irrigation water use. Several detailed mathematical models have been developed to simulate land surface energy fluxes and crop actual evapotranspiration by using energy balance approach.

Because the process of evapotranspiration is controlled by the energy exchanges at the soil-plant-atmosphere system and is limited by available energy at the surface, it is possible to estimate evapotranspiration by applying the energy conservation concepts and remotely sensed data.

Satellite images and Remote Sensing (RS) techniques enable analyzing and mapping *ET* over large areas, so to identify the temporal and spatial evolution of vegetation and water consumption. Advances in computing technology with the free or low-cost availability of satellite images have promoted the development of RS utility in modeling *ET*. Among several major contributions related to remote sensing, Courault et al. (2017) mentioned the potential of the fine spatial and temporal resolutions of remotely sensed data to provide decision support for precision farming activities. Senay et al. (2017) retrieved remote sensing-based field-scale *ET* maps by using historical data. These retrievals were useful in characterizing water use patterns and assessing crop performance over long time periods, which has a great potential in planning water resource allocation and managing water rights.

Khanal et al. (2017) reviewed current and potentials thermal remote sensing applications in precision agriculture. The review demonstrated the usefulness of thermal remote sensing data in irrigation scheduling and other agricultural applications. Kustas et al. (2003) considered remotely sensed surface temperature as the key boundary condition in most, if not all, RS based energy balance models used to estimate *ET*. These RS models can be utilized and applied to large areas and can be distributed spatially by using surface brightness temperature (T_b), and some ancillary data retrieved from satellite remotely sensed imagery (Ciraolo et al., 2006).

Remote sensing approaches use the surface energy balance (SEB) to estimate the energy corresponding to *ET* process. The SEB approach estimates *ET* as a residual of the surface energy balance equation after calculating all the other energy balance components. Satellite-based RS models are intensively used to estimate actual *ET* based on the land surface energy balance components.

Several SEB models can be used to provide an instantaneous estimation of the latent heat flux (λET) at the time of the satellite overpass. Single source SEB model deals with the land surface as one layer, and thus don't differentiate between different pixel components. Several single sourse SEB models are widely used (Wagle et al., 2017 and Bhattarai et al., 2016). Among which; Mapping ET with Internalized Calibration model (METRIC) (Allen et al., 2007), the Surface Energy Balance Algorithm for Land (SEBAL) (Bastiaanssen et al., 1998a), the Surface Energy Balance System (SEBS) (Su, 2002), the Simplified Surface Energy Balance Index (S-SEBI) (Roerink et al., 2000), and the operational Simplified Surface Energy Balance (SSEBop) (Senay et al., 2013).

Another SEB based models such as the the Two-Source Energy Balance Model (TSEB) (Norman et al., 1995) and the Hybrid dual-source scheme and Trapezoid framework-based ET Model (HTEM) (Yang and Shang, 2013) can even partition the energy fluxes into soil and canopy fluxes and as a result can differentiate vegetation transpiration fluxes from surface evaporation.

1.2 Thesis Objectives

Use of remote sensing to analyze water and energy balance in the soil-plant-atmosphere are numerous. The general objective of the thesis was to address the possibilities of using remotely sensed data in analyzing irrigation practices. The temporal and spatial modeling of energy balance components retrieved by satellite remote sensing acquisitions and ancillary meteorological data have been used to assess actual evapotranspiration in two large-scale irrigation districts, either on field and irrigation district scales, under typical Mediterranean climate.

This research has two main objectives:

- The primary objective was to assess the potential of remote sensing satellite-based approaches and surface energy balance models in retrieving actual crop evapotranspiration and the ability of moderate resolution Landsat Thematic Mapper platform to model actual evapotranspiration over large irrigation districts.
- The secondary objective was to assess the applicability of remote sensing-based techniques and surface energy balance models in the framework of monitoring water consumption in large-scale irrigation systems to assess the trade-offs between irrigation water and energy consumptions.

1.3 Thesis Structure

The thesis is organized into six chapters; the first is an introductive chapter reporting the problematic and the thesis objectives. The remaining chapters are divided into three main parts: i) theoretical background, ii) materials available, iii) methodology and experimental applications and iv) results of applied methodologies and the related discussion. The last chapter reports the conclusions and findings of the research, as well as some recommendations based on the achieved results.

Chapter 1: Introduction

This chapter is divided into three main parts; the first outlines the problem of water scarcity, the water and energy interactions and the contribution of remote sensing in hydrological modeling and evapotranspiration retrieval. The second part describes the main objectives of the thesis, and the third reports the outline of the thesis structure and explains its organization.

Chapter 2: Theoretical Background

The second chapter describes the theoretical background. It is divided into eleven main sections. The first outlines the water balance in the soil-plant-atmosphere (SPA) continuum, whereas the second describes the evapotranspiration (*ET*) process, methods to measure *ET* and the interaction between water, mass and energy balance in the SPA continuum, with particular emphasis on the evapotranspiration process. The 3rd and 4th sections demonstrate the interaction between land surfaces

with overlying atmosphere, with particular attention to the wind profile and, heat and momentum transfers. The 5rth section highlights the theoretical basis of surface energy balance and remote sensing based modeling, with special emphasis on the Surface Energy Balance Algorithm for Land (SEBAL) model and the Two-Source Energy Balance (TSEB) model. The 6th section deals with the flux tower micro-meteorological measurements and the surface energy balance closure. The 7th section illustrates the temporal upscaling of instantaneous latent heat flux and the evaporative fraction self-preservation hypothesis. In sections 8 and 9 the optical atmospheric correction and the thermal radiometric calibration of remote sensing data is discussed. The last two sections illustrate the Surface Albedo and Vegetation indices used in modeling the Surface energy balance.

Chapter 3: Materials

The third chapter initially describes the study area with regard of localization, climatic characteristics, vegetation distribution and other characteristics. The first case study is the irrigation district of SAT Llano Verde, Albacete, in Castile-La Mancha region (Spain), that was investigated for irrigation seasons 2006-2008; the second case study is irrigation district 1/A managed by "Consorzio di Bonifica di Agrigento 3", located in Castelvetrano, Sicily (Italy), studied for irrigation seasons 2009-2010. Then, the chapter describes instruments and tools used for the research in both the case studies, such as meteorological stations, micro-meteorological flux tower (Castelvetrano district) and remote sensing satellite images, and deals with the characteristics of the used materials.

Chapter 4: Methods

This chapter represents the core of thesis and describes methodologies used in the research application. It describes the remote sensing-based approach and reports indications on pre-processing and elaboration of Landsat TM images. Pre-processing includes atmospheric corrections, radiometric calibrations, as well as the retrieval of parameters used for applications (e.g., surface reflectance, surface albedo, vegetation indices, land surface emissivity and surface radiometric temperature). The second part describes the methodologies adopted in modeling the surface energy fluxes, such as net radiation and soil sensible and latent heat fluxes. In

particular, the section describes the single (SEBAL) and dual source (TSEB) approaches to retrieve surface energy fluxes and reports, also, information on data to estimate the evaporative fraction (Λ) and to apply the self-preservation hypothesis of Λ. Moreover, methodologies for temporal upscaling of single and two source instantaneous evapotranspiration to daily and seasonal time-step are also described. Finally, the last section details the use of the remote sensing *ET* to develop an irrigation performance index, later considered for both irrigation districts.

Chapter 5: Results and Discussion

In this part, results are outlined and critically analyzed. The chapter focuses mainly on the applications of the residual energy balance, single and two-source models and specifically on the retrieval of latent heat flux. It also emphasizes the potential of using remote sensing satellite-based applications in monitoring large-scale irrigation systems. The results achieved by application of SEBAL and TSEB are compared to flux tower measurements. Finally, the chapter analyzes the upscaling of evapotranspiration to obtain daily and seasonal values and the utility of these estimations in monitoring water consumption in large-scale irrigation systems.

Chapter 6: Conclusions

The chapter summarizes main results and evidences the potentials and limits of the applied methodology. Some recommendations for further works and possible future developments in this research line are also indicated.

Chapter 2: Theoretical Background

2.1 Interactions in the Soil-Plant-Atmosphere system

Several biological and physical processes control the water balance in the soil-plant-atmosphere system (SPA) at different levels such as underground transmission zone, land surface crop and atmosphere. The soil, plant and atmosphere system is considered as a continuum, where mass and energy fluxes are connected. In SPA continuum, interactions between components can be schematized as balances representing the equilibrium between system's inputs and outputs (Figure 2.1).

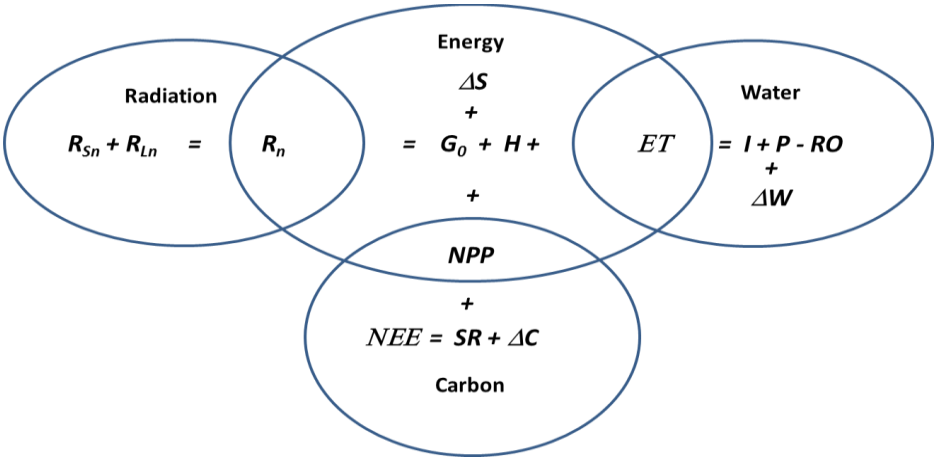

Figure 2.1: Schematic representation of Soil-Plant-Atmosphere system. The overlap regions indicate interconnections between the different balances.

2.1.1 The Radiation Balance

The radiation balance explains how the net surface radiation flux (R_n) is associated to the net amounts of shortwave radiation (R_{Sn}) and longwave radiation (R_{Ln}) of the electromagnetic spectrum (Figure 2.1). The emitted solar radiation that reaches the earth's surface is mainly controlled by earth-sun relative location and atmospheric conditions (Iqbal, 1983). The overall land surface radiation balance scheme is represented in figure 2.2, where the incoming radiant energy components are in blue highlighted, whereas the outgoing ones are in red.

A portion of solar radiant energy arriving at the top of the atmosphere is absorbed, scattered and reflected by the atmospheric particles. The remaining solar radiation reaching the earth surface is known as "incoming shortwave radiation" ($R_{S\downarrow}$), that includes the direct and diffused solar radiant energy. The former represents the solar incoming shortwave radiation penetrating the earth atmosphere and reaching the earth surface, while the diffused radiation accounts for the portion of the total incident radiation that, originating from atmospheric scattering, arrives to the earth surface. A portion of $R_{S\downarrow}$ is absorbed by the surface, and the remaining is reflected. The surface albedo (α) (dimensionless) is the percentage of incoming shortwave electromagnetic radiation reflected by the surface in the shortwaves. The albedo is influenced strongly by the

land cover; indeed, it is controlled by the "color" and type of soil or vegetation, surface water content and surface roughness (Campbell and Norman, 2012).

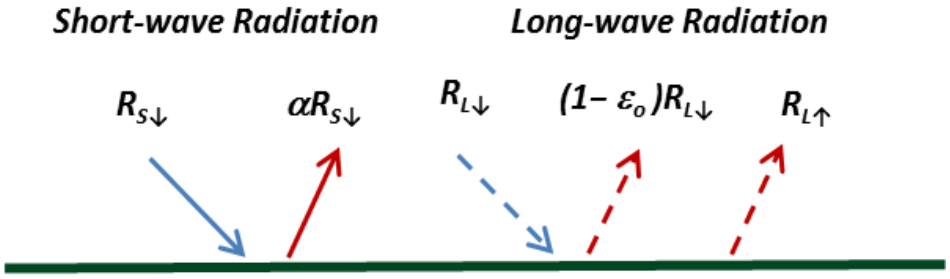

Figure 2.2: The overall radiation balance scheme at land surface

The longwave radiation (R_L) is the electromagnetic radiation emitted from earth's surface or the atmosphere. R_L originates from the incident solar electromagnetic radiation that is absorbed by the atmosphere or land surface and then re-emitted. The incoming longwave radiation ($R_{L\downarrow}$) represents the atmospheric downward originated thermal radiation. $R_{L\downarrow}$ is in function of near-surface air temperature and atmospheric emissivity, ε_0. The term $(1 - \varepsilon_o)R_{L\downarrow}$ represents the fraction of incoming long-wave radiation reflected from the surface proportionally to the land surface thermal emissivity (ε_o). The outgoing longwave radiation ($R_{L\uparrow}$) represents the upwelling thermal radiation emitted to atmosphere from land surface.

2.1.2 The Water Balance

The soil water balance represents the connection among the water flux inputs and outputs over a period of time in the SPA system. The dynamic of water fluxes can be analyzed by means of hydrological inputs and losses. The water balance, schematized in figure 2.3, reproduces the different terms of water balance in the SPA continuum constituted by a vegetated soil. Inputs to the system are precipitation (P), irrigation (I), horizontal subsurface water transfer into the root zone (SF_{in}) and water transported to root zone by capillary rise (CR). On the other hand, outputs are surface runoff (RO), deep percolation to soil layers beneath the root zone (DP), horizontal subsurface flow out of the root zone (SF_{out}), as well as soil evaporation (E_s) and canopy evapotranspiration (ET_c).

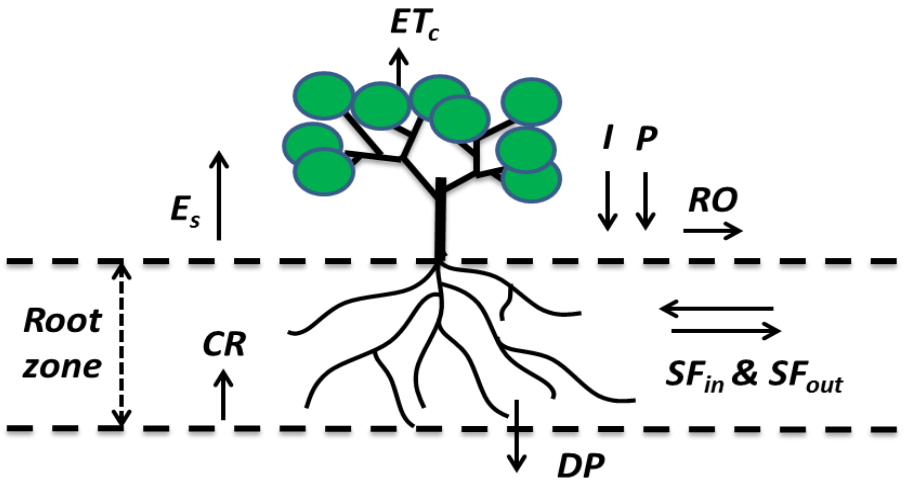

Figure 2.3: Soil water balance with schematization of water fluxes (inflow and outflow)

Soil evaporation (E_s) and canopy evapotranspiration (ET_c) are the primary sources of water loss from the plant's root zone and are usually combined in a single term, *ET*. For a fixed time interval, if all the incoming and outgoing fluxes in the plant root zone are known, *ET* can then be deduced by the change of soil water content, $\Delta\theta$, as follows:

$$ET = I + P + CR + SF_{in} - RO - DP - SF_{out} + \Delta\theta \quad (2.1)$$

2.1.3 The Carbon Balance

The carbon cycle reproduces the soil-plant respiration (*SR*), the net photosynthesis (*NPP*), the net ecosystem exchange (*NEE*) and the carbon dioxide storage (ΔC). Regarding the energy partitioning, it is not crucial to consider the energy involved in the carbon cycle since it is much smaller than other mentioned balance terms.

2.1.4 The Surface Energy Balance

The most critical variable of energy balance system is the net radiation (R_n). R_n is the net amount of radiation energy available for heating soil and air, or for evaporating soil water. R_n is the driving force of all the processes occurring in any SPA system. The sensible heat flux (*H*)

arising from surface represents the rate of heat loss in the air by convection and conduction due to differences in temperatures, and it is involved in heating and cooling the system. The soil heat flux (G_0) is the rate of soil heat storage due to conduction. ΔS is the rate at which the heat is stored in the canopy. As an energy term, *NPP* represents the biological energy consumption. The last component of the energy balance is the Latent Heat Flux λET, which represents the evaporative energy able to change the state of water and to transfer energy in the form of latent heat. In SPA system, λET is the most important variable related to water consumption, and it represents the rate of latent heat loss from the surface due to evapotranspiration processes.

Usually, the energy terms such as the heat stored or released in the plant and the energy used in the plant's metabolic activity, are usually neglected in the surface energy balance equation. Gates (1980) and Larcher (1983) showed that the energy used for plant's metabolic activity accounts for a tiny portion of the total energy and could be considered negligible in comparison to other energy terms. Similarly, the rate of heat storage, ΔS, is considered negligible even if it can reach a percentage of about 5% of the global radiation on a sunny summer day (Brutsaert, 2005). Based on these assumptions, the surface energy balance equation considers only four components of energy fluxes:

$$Rn - G_0 - H - \lambda ET = 0 \qquad (2.2)$$

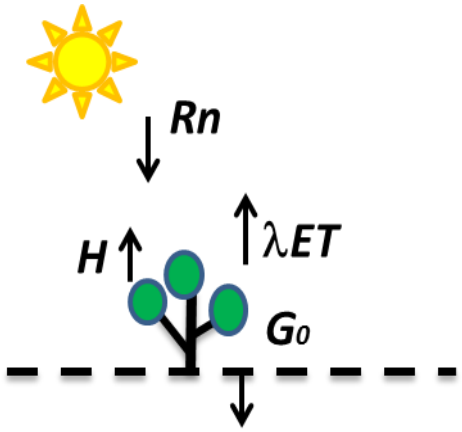

Figure 2.4: Main components of surface energy balance

The surface energy balance considers the diurnal net radiation (R_n) during clear sky hours as a positive component directed downward to a specific surface, to which supplies energy, while the remaining components, removing energy from that surface, are negative when directed away from the surface (Fig. 2.4). Water evaporation process requires supplying sensible energy or radiant energy to transform water molecules into vapor. Therefore, the process of evapotranspiration is controlled by the amount of energy available and the energy transfer at vegetation and soil surface. Because the energy exchange in the SPA system controls the evapotranspiration process, for a fixed time interval, incoming energy on a surface must be equal to the outgoing energy. The latent component of the energy balance can be estimated by applying the concepts of energy conservation by subtracting G_0 and H from the surface net radiation flux (indeed, ET is calculated as residual of the surface energy balance).

2.2 Evapotranspiration

Land-surface evapotranspiration (ET) represents the primary component in the hydrologic cycle; its accurate estimation is mandatory in optimizing agricultural water management. ET is a combination of two separate processes: the first refers to the evaporation from soil and, to a lesser extent, from vegetation surface; the second considers the transpiration from vegetation. The processes of evaporation and transpiration are simultaneous and difficult to be distinguished (Allen et al. 1998). Evaporation can be defined as the process whereby liquid water is converted to vapor and removed from the evaporating surface. Changing the state of liquid water to vapor requires energy, that is usually provided by direct solar radiation and, to a lesser extent, by the air emissions in the longwaves. Water evaporates from a variety of surfaces, such as lakes, rivers, pavements, soils and wet vegetation.

Only a tiny fraction of water absorbed by the plant roots is then used by the plant, while the rest is lost by transpiration. The latter represents the process of vaporization of water contained in plant tissues, that is converted from the liquid state to vapor. This process occurs at leaf scale and is controlled by the leaf stomata and stomatal aperture. To assess evapotranspiration, it is necessary to consider meteorological variables, such as solar radiation, air temperature, relative air humidity, air vapor

pressure and wind speed (Allen et al. 1998). When assessing *ET*, it is also important to consider the source area of latent heat fluxes,.

The assessment of the combined loss of water from the soil (through evaporation) and vegetation (through transpiration) in important in agricultural management (Pereira et al., 2015); indeed, *ET* assessment is mandatory in optimizing agricultural water consumption.

ET measuring/estimating methods include lysimeters, scintillometers, Eddy Covariance micrometeorological towers (*EC*) and energy and water balance methods; this latter can be applied by means of remote sensing acquisitions in order to retrieve *ET* spatial distribution.

Even though measurements of actual *ET* with weighing lysimeters are characterized by high precision, they are too expensive and time-consuming for continuous acquisitions; moreover, they are representative of a very small area and cannot be used for large-scale regional applications. Understanding local-scale *ET* can be achieved through micrometeorological observation techniques such as eddy correlation, Bowen ratio, and scintillometry. These techniques are also characterized by high precision and have been commonly accepted to assess actual evapotranspiration, at local-scale, in a wide range of land conditions. However, the application of these methodologies on wider scales is extremely limited and expensive. As an example, micrometeorological methods allow estimating *ET* over small footprints only; thus, its extrapolation at a wider scale is not practicable due to land surface heterogeneity and the dynamic nature of the energy transfer processes (Moran and Jackson, 1991; French et al., 2005).

It is important to notice that evapotranspiration takes place at the potential rate (ET_p) under well-watered conditions (absence of crop water deficit) and therefore when water is not limiting the crop growth. Potential ET_p is not constant and varies depending on crop conditions. Indeed, *ET* strongly decreases during a natural or induced crop water stress as the plant's stomata opening is reduced to decrease the loss of water through the transpiration processes. When this kind of stress occurs, the rate at which *ET* takes place is known as actual evapotranspiration (ET_a).

In agricultural applications and for irrigation purposes, especially when it is difficult to obtain field measurements, crop evapotranspiration is

computed by conventional methods based on meteorological observations. In particular, standard meteorological data are used to compute evapotranspiration of a reference crop, ET_0, (Allen et al. 1998); then maximum crop evapotranspiration (ET_p) is estimated by using site-specific crop coefficients. One of the most used equation to estimate ET_0 is the FAO Penman-Monteith, which determines the values of evapotranspiration of a hypothetical grass reference surface, characterized by an albedo equal to 0.23 and surface resistance of

70 s.m^{-1}. The equation recommended as the standard method to compute ET_0 in [mm day^{-1}], can be written as (Allen et al. 1998):

$$ET_o = \frac{0.408\Delta(R_n - G_0) + \gamma \frac{900}{T+273.16} u_2 (e_s - e_a)}{\Delta + \gamma(1 + 0.34u_2)} \quad (2.3)$$

where R_n [MJ m^{-2} day^{-1}] is the net radiation, G_0 [MJ m^{-2} day^{-1}] is the soil heat flux, T [°C] is the air temperature at reference height of 2 m, u_2 [m s^{-1}] is the wind speed at the reference height, e_s and e_a [kPa] are saturation and actual vapor pressure, being e_s-e_a the saturation vapor pressure deficit, Δ [kPa °C^{-1}] is the slope of vapor pressure curve and γ [kPa °C^{-1}] is the psychrometric constant.

ET_0 determined by Penman-Monteith equation provides standard values for the reference crop, which can be multiplied by the crop coefficient (K_c) to determine the maximum evapotranspiration (ET_p) of a specific crop under standard conditions:

$$ET_p = K_c ET_0 \quad (2.4)$$

Although ET_p has been widely studied and applied, its calculation is still complicated, since many agricultural areas lack all the necessary ground data needed as inputs to calculate ET_0. Usually, the meteorological data are obtained from stations located far away from the site of interest; thus, leading to inadequate and incorrect outputs also because of difficulties of an accurate K_c estimation.

2.3 Roughness parameters and wind profile

The interaction between soil surface or a vegetative surface with the overlying atmosphere is due to momentum and heat fluxes and air moisture. Thus, the parameterization of this interaction can be done after defining a roughness parameter, which is often considered as the more critical among the required inputs by the surface energy balance (SEB) models, because it increases air mixing and turbulence. The zero plane displacement length (d_0) [m] and the momentum roughness length (z_{om}) [m] represent the roughness lengths governing the momentum transfer with the atmosphere.

Under the hypothesis of logarithmic wind profile, the sum between d_0 and z_{0m} represent the height above ground where wind speed is theoretically reduced to zero.

For a bare soil, since roughness occurs at the surface itself, d_0 is set to zero, and the roughness is fixed to a typical value of z_{0m} = 0.01 m. Estimation of wind velocity above plant canopy requires the assessment of d_0 and z_{0m} from the canopy height. Modeling wind speed in the presence of canopy requires dividing the vertical canopy profile into 3 layers. The first (Layer I) is above the canopy, where wind speed can be modeled by using the logarithmic profile. The second (Layer II) is within the canopy space, where wind speed decreases in function of the density of leaves. The third (Layer III, z_s) corresponds to the bottom of the canopy, which is usually assumed as 10% of canopy height. In the latter layer, a different profile is developed based on the soil surface characteristics. Figure 2.5 shows the wind speed profiles in these three layers (I, II and III).

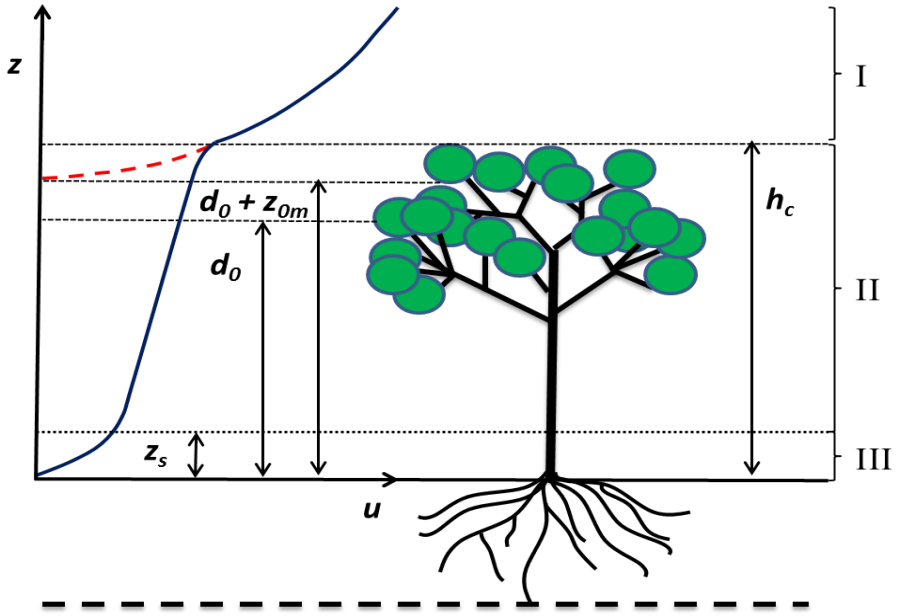

Figure 2.5: Wind speed profiles in the three layers (I, II and III) in which the vertical canopy profile is divided

2.4 Momentum transfer and atmospheric stability

It is crucial to define some exchange parameters between the soil surface and the lower layers of the atmosphere. Atmospheric Boundary Layer (ABL) represents the lower layer that interacts with the earth's surface. The atmospheric transport processes of mass and heat in this layer is assumed turbulent. Turbulence in the atmosphere can be caused by fluctuations of wind speed and direction, temperature differences, the concentration of atmospheric gases and can be associated with eddies. The atmospheric stability has a significant impact on turbulent fluxes such as latent and sensible heat fluxes. Three stability conditions of air are generally defined (Allen et al., 2002) as:

- Unstable, occurring when an air mass is warmer than the surrounding air, and the temperature gradient generates an upward force on the air mass.
- Neutral, when no force occurs, and the air mass temperature has the same temperature of the surrounding air.

- Stable, when the surrounding air is warmer than the considered air mass and a downward force is generated on the air mass.

Figure 2.6 shows the three air stability conditions when an adiabatic lapse rate occurs (the dry air mass decreases its temperature of 1 °C for each 100 m movement in elevation).

In SEB model, stability corrections are applied to account for non-adiabatic conditions where the sensible heat flux can produce or reduce thermal turbulence by changing the temperature gradient to a non-adiabatic condition. Negative heat flux can lower air temperature near the surface, which will decrease the vertical turbulence and mixing. A positive, sensible heat flux can increase air temperature near the surface, which enhances vertical turbulence and reduces aerodynamic resistance. The effect of thermally produced turbulence is an important aspect that should be taken into account in characterizing non-adiabatic conditions.

2.5 Land surface SEB models and Remote sensing based Evapotranspiration

Modelling *ET* as a residual term of the energy balance leads to actual evapotranspiration (ET_a) assessment; ET_a represents the real amount of water loss by the soil-vegetation system. Satellite imagery is usually employed to estimate ET_a spatial distribution (Singh et al., 2015).

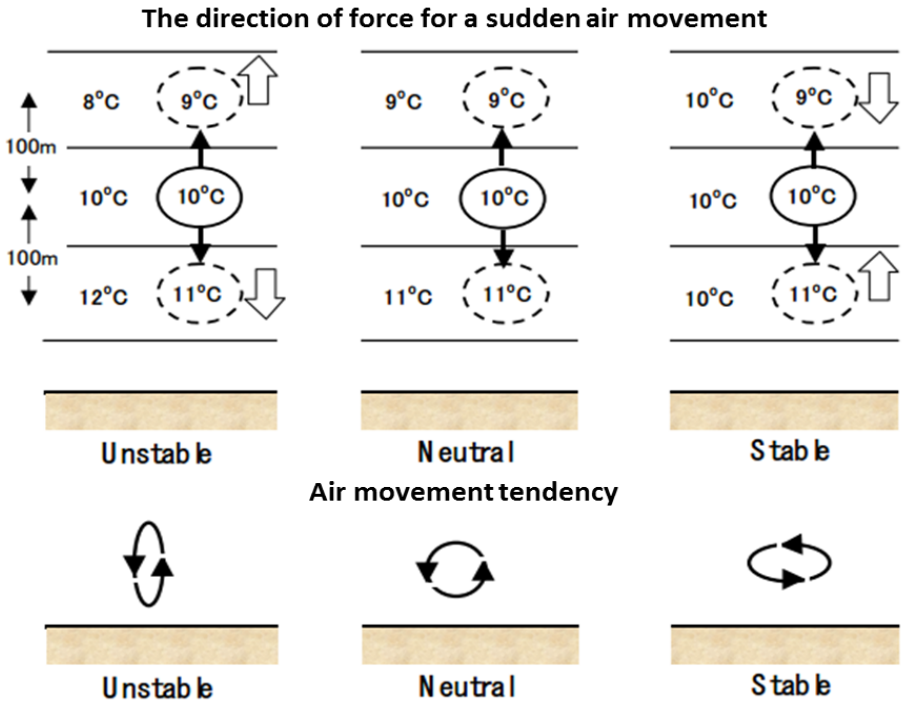

Figure 2.6: Schematic description of unstable, neutral and stable atmospheric conditions (Allen et al., 2002)

The image spatial resolution is represented by the single pixel size, whereas the temporal resolution is given by the frequency in which the satellite sensors overpass or the revisiting frequency over a specific location. Low spatial resolution satellite sensors such as the Moderate Resolution Imaging Spectroradiometer sensor (*i.e.* MODIS), onboard both the Terra and Aqua satellites, offers the advantage of high temporal resolution (two daytime acquisitions per day), even if their low spatial resolution is not suitable to analyze fields of a few hectares. Moderate to high-resolution sensors such as Landsat 5 thematic mapper (TM), Landsat 7 Enhanced Thematic Mapper Plus (ETM+), Landsat 8 Operational Land Imager (OLI), Thermal Infrared Sensor (TIRS) and the Advanced Spaceborne Thermal Emission and Reflection Radiometer (ASTER) even if characterized by low temporal resolution, are suitable for evapotranspiration assessment at crop basis. The use of the moderate to high-resolution images is valuable for water rights management,

irrigation scheduling, as well as discrimination of *ET* among crop types (Allen et al., 2007b).

Among the SEB models, the Surface Energy Balance Algorithm for Land (SEBAL), developed by Bastiaanssen et al. (1998a) and the two-source energy balance model (TSEB) initially developed by Norman et al. (1995) are the widely used. Both models have been validated under a range of environmental conditions (Anderson et al., 2007; Bastiaanssen et al., 2005; Crow and Kustas, 2005) and are used to estimate instantaneous λET as the residual term of energy balance equation at the time of image acquisition. These models use the surface radiometric temperature as the primary variable allowing estimating instantaneous energy fluxes to solve the surface energy balance equation. Both models consider that available energy, obtained as the difference between total R_n and G_0, is partitioned into turbulent fluxes H and λET. The main difference between SEBAL and TSEB is how they parameterize interactions between land surface and the surrounding atmosphere. SEBAL is a single-source model, which does not differentiate between soil-vegetation components. On the other hand, TSEB uses a two-source modeling schemes to separate the energy fluxes between canopy and soil components.

SEBAL is a satellite-based image-processing model developed by Bastiaanssen et al. (1998a). It is one of the RS models that have been increasingly used worldwide. The theoretical and computational basis of SEBAL has been widely described by Bastiaanssen et al. (1998), (2000) and (2005).

SEBAL has the advantage of requiring little ground-based meteorological data, making it suitable for those places where such data are limited. The model can be used to estimate ET_a without any preliminary knowledge of field conditions such as soil type, crop distribution, and management practices (Bastiaanssen et al., 2005). Because of SEBAL is a single-source model it is most appropriate in the case of uniform vegetation coverage (Minacapilli et al., 2009).

In SEBAL model, R_n is computed using pixel-wise narrow-band reflectance and emittance data. The soil heat flux (G_0) is empirically estimated from the net radiation, surface temperature, and vegetation indices. The sensible heat flux (H), considered as a physically based

single-layer transfer, is estimated from land surface temperature, surface roughness, and wind speed by using buoyancy correction (Singh et al., 2015). *H* is a function of the near surface to air temperature gradient ΔT and the aerodynamic resistance to heat transport (r_{ah}) (Bastiaanssen et al., 1998 and 2005). As a single-source model, SEBAL uses only one resistance and assumes that all the components inside a pixel can be represented by a single temperature value (Huntingford et al., 2000). The SEBAL model schematization is shown in figure 2.7.

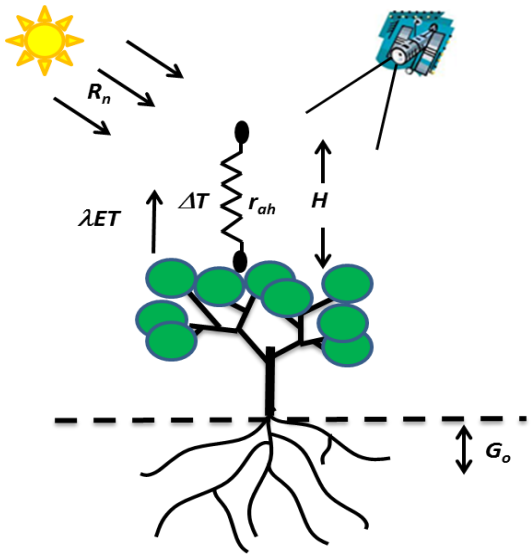

Figure 2.7: Aerodynamic resistance rah and surface energy balance variables used in SEBAL

ΔT represents the temperature difference between the land surface and the air above the canopy. To retrieve these variables, SEBAL firstly assumes that a pixel reproduces a homogenous transfer layer and, secondly, that ΔT varies linearly with radiometric temperature (T_{rad}) in all pixels; thus, the determination of ΔT is achieved after taking two extremes "calibration pixels" which are supposed always present in any full image scene. The first calibration pixel is called hot pixel as it is a dry bare soil surface where λET is considered negligible (thus it is characterized by a very high surface temperature); whereas, the second is called cold pixel as it is a well watered vegetated surface in which the sensible heat flux can be considered negligible (thus it is characterized by

a very low temperature). As result of this assumption, SEBAL estimates *H* and applies an iterative flux profile method (Gieske, 2003), necessary to establish the atmospheric stability conditions. Finally, the instantaneous latent heat flux (λET) is obtained as the residual of the energy budget equation without discriminating canopy and soil components. Figure 2.8 shows the flow chart of SEBAL model, including input and output variables.

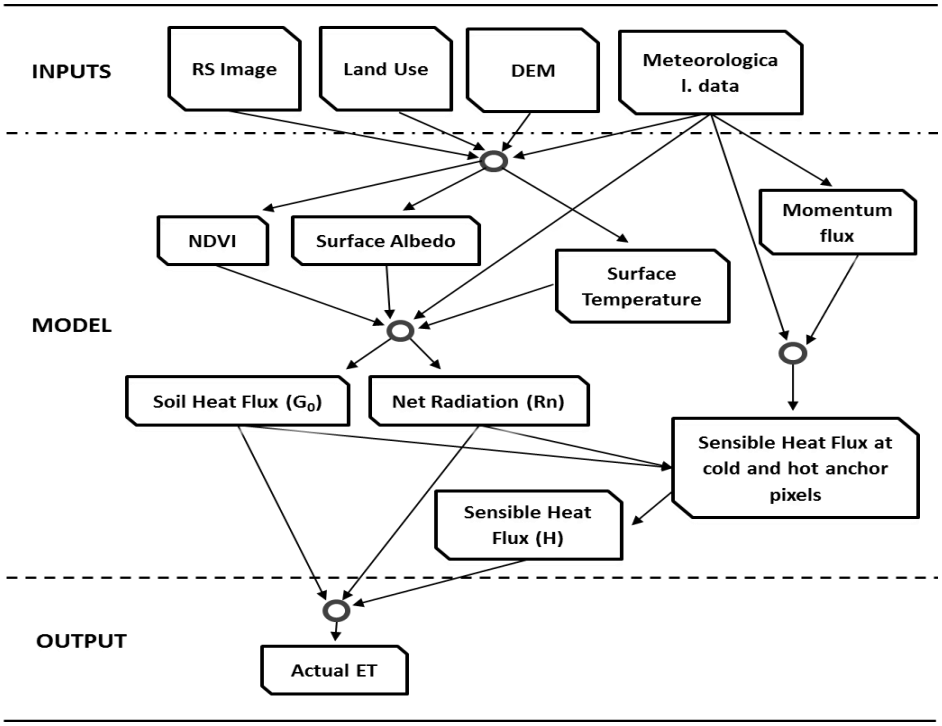

Figure 2.8: Flow chart of the main inputs and output of SEBAL model

The SEBAL model has been widely used under different field and crop conditions with a typical assessment error of 15% at field scale and on a daily basis (specific satellite image date) which decreases to 5% on a seasonal basis (Bastiaanssen et al., 2005). SEBAL was proved as an efficient, accurate, and inexpensive procedure to estimate actual evaporation fluxes from irrigated lands throughout growing seasons (Allen e al., 2007). Bastiaanssen et al., 1998 verified SEBAL outcomes in a set of experiments carried out in Castilla la Mancha region (Spain).

These authors validated instantaneous SEBAL estimations by using the evaporative fraction; it was proven that the differences between the evaporative fraction (Λ), representing the ratio between λET and the available energy ($R_n - G_0$) estimated by remote sensing, and the corresponding values obtained by an eddy covariance tower were characterized by RMSE values ranging between 0.10 to 0.20 for a single footprint (over a footprint of several hundreds of meters). These authors also demonstrated that RMSE is substantially reduced to 0.05 if several flux tower footprints were aggregated to a length scale of a few kilometers. The same study, demonstrated that the overall difference of evaporative fraction is negligible when considering the watershed scale (Bastiaanssen et al., 1998).

2.5.1 The Two-Source Energy Balance model

Another satellite-based image-processing model used to estimate actual *ET* is the Two-Source Energy Balance Model (TSEB), initially developed by Norman et al. (1995) and further modified by Kustas and Norman (1999) and Kustas et al. (2004). The TSEB model partitions the energy fluxes and the surface temperature between canopy and soil (Shuttleworth and Gurney, 1990; Kustas, 1990). The two-source model overcomes a defect of the single source SEB model which deals with vegetation and soil as one layer; thus, it can be applied especially in areas characterized by sparse vegetation and non-full vegetation cover. Similarly to the single source energy balance algorithms, TSEB retrieves the main energy fluxes, such as *Rn*, G_0, and *H*, and then estimates λET as residual of the surface energy budget. Additionally to the capability of TSEB of partitioning the energy fluxes into soil and canopy fluxes, the approach used to retrieve the sensible heat flux is different. The flux partitioning is mainly driven by using vegetation indices to split the soil and canopy components.

Values of *H* are estimated on the basis of physically-based temperatures gradient, and resistances approaches, by means of an iterative procedure. TSEB assumes initially that vegetation is not stressed and therefore transpires at the potential rate, so that canopy sensible and latent heat fluxes are estimated under potential conditions. After obtaining the canopy sensible heat flux (H_c), it is used to estimate the components of temperatures by using the fractional cover (f_c) to retrieve the vegetation

and soil components of H based on an iterative process. As a result, TSEB retrieves the soil component of the sensible heat flux and thus computes the evaporation from soil (λE_s) as a residual of the energy budget. If the estimated λE_s is positive, it confirms the assumption of potential transpiration, while a negative result means that the soil is dry and then the vegetation is under water stress conditions. In this case, the λE_s is set to zero, and a new iteration starts assuming the absence of soil evaporation. As result of this iterative approach, TSEB retrieves actual evaporation and transpiration components of total latent heat flux.

TSEB differs from SEBAL also in the estimating the gradients of temperatures and the corresponding resistances. With the advantage to consider separately aerodynamic temperature and radiometric temperatures (Norman et al., 1995). In TSEB temperatures are divided into three components: soil temperature (T_s), canopy temperature (T_c) and air temperature above the canopy (T_{ac}); accordingly, it also takes into account three resistances: the first refers to the canopy-air boundary layer (r_x), the second to the heat flow in the soil–canopy boundary layer just above the soil surface (r_s) and the third is the aerodynamic resistance for heat and water vapor (r_a). Figure 2.9 schematizes the main energy balance variables of a TSEB model with "in-series" resistances.

Similarly to the single-source model, TSEB provides instantaneous values of λET that can be upscaled to daily values by assuming the self-preservation hypothesis of the evaporative fraction (Λ). The TSEB approach was found to be valuable in estimating surface energy fluxes (Colaizzi et al., 2012); in addition, it is less sensitive to roughness length (Chirouze et al. , 2014). The theoretical and computational basis of TSEB is described in Norman et al. (1995) and Kustas and Norman (1999).

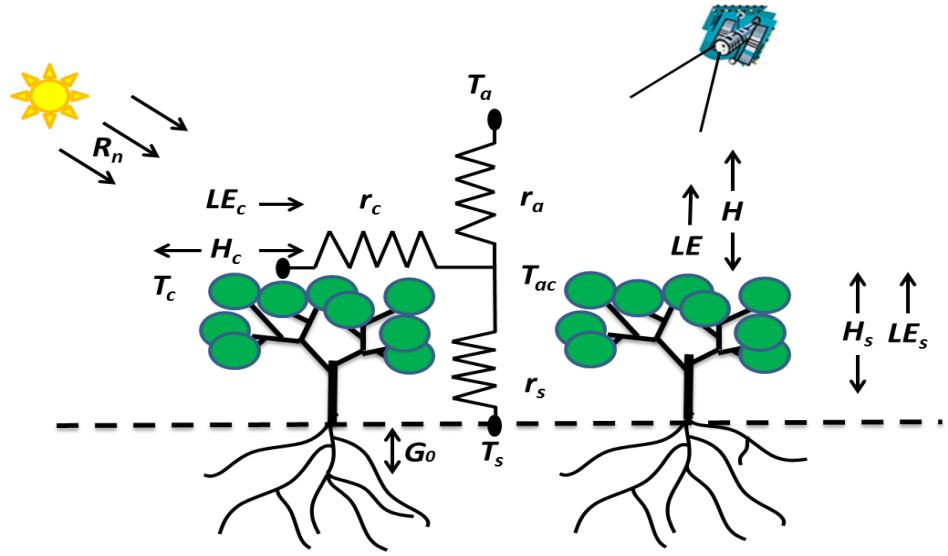

Figure 2.9: The main energy balance variables of a TSEB model with "in-series" resistances

2.6 Flux tower measurements and closure of energy balance

Eddy covariance systems are widely used to provide measurements of both λET and H fluxes over plant canopies. Additional instruments such as net radiometers and soil heat flux plates can be deployed to measure net radiation and ground heat flux. A well-equipped flux tower provides measures of all the surface energy balance components; thus, usually pointing out an imbalance between the turbulent fluxes measured by eddy correlation system ($H + \lambda ET$) and the independent measurement of net radiation and soil heat flux, known as the available energy ($R_n - G_0$); imbalancing (Wilson et al., 2002; Culf et al. 2004; Foken et al. 2006).

The reasons for failure in the energy balance closure can be due to the different instruments accuracies and footprint. Moreover, some terms of the balance, such as the energy storage involved in biomass production, metabolic activity, and heat storage are neglected and therefore contribute to the global error (Foken and Wichura, 1996). Another factor

contributing to the energy balance closure failure is linked to land surface heterogeneity (Panin et al., 1998).

Among the measurements of energy balance components, the most accurate measurements are commonly considered net radiation R_n and G_0. Foken (2008) found that errors on λET and H are respectively in the ranges of about 10–20% and 5–15%, while the error in net radiation measurement is of about 6%. In the same study, it was highlighted that even if G_0 measurements are usually less accurately assessed it is characterized by the lowest values (≈ 15 W m^{-2} for canopies full cover). For these reasons, it is highly recommended to assess the energy balance closure (Cr) by rationing available energy ($R_n - G_0$) to the turbulent flux components ($H + \lambda ET$) (Wilson et al., 2002).

A common practice is adjusting the turbulent energy components (H and λET) by forcing the energy closure targeting to preserve the Bowen ratio (β) as an indicator of energy partition (Prueger et al., 2005 and Twine et al., 2000). This indicator, originally developed by Bowen (1926), is computed as the ratio of H to λET ($H/\lambda ET$). The knowledge of β allows partitioning available energy between H and λET by computing the correction closure errors ΔH and $\Delta\lambda ET$ as follows:

$$\Delta\lambda ET = \frac{(Rn - G_0) - (1+\beta)\lambda ET}{(1+\beta)} \tag{2.5}$$

$$\Delta H = \beta(\lambda ET + \Delta\lambda ET) - H \tag{2.6}$$

This approach allows separating the closure error between the most uncertain measured data (H and λET) proportionally to the magnitude of energy of these fluxes itself. Somma (2003) showed that β varies during the daytime in the range of 0 -1 for well-watered areas and can reach up to 10 for dry areas. Brutsaert (2013) showed that the values of β can be negative close to dawn and sunset when fluxes are small, which makes it a poor descriptor of energy partitioning at these above mentioned times.

2.7 Temporal upscaling of instantaneous latent heat flux

Computing actual ET over extended time intervals, such as irrigation seasons, is useful in water resources management. SEB models estimate instantaneous actual ET at the satellite overpass time. Quantifying actual

evapotranspiration on seasonal basis involves two steps: the first involves estimation of *ET* on daily bases at image acquisition dates, by extrapolating daily from instantaneous values; whereas, the second allows extending daily values to periods between satellite overpasses.

Several methods have been proposed to up-scale instantaneous estimates of λET into longer time-steps, such as daily (ET_D) estimations (Chávez et al., 2008). One of them assumes the theory of diurnal self-preservation of evaporative fraction (Λ). Another method uses the incoming shortwave radiation, R_s as upscaling reference variable (Jackson et al., 1983).

2.7.1 The self-preservation hypothesis and the evaporative fraction

The latent heat flux and other components of the energy balance equation show a significant diurnal variability near the surface. However, the relationship between those fluxes shows relative perseverance during daytime (Shuttleworth et al., 1989; Bastiaanssen et al., 1996; Jackson et al., 1983). The main assumption of self-preservation hypothesis is that the ratio of most of the daily fluxes is often assumed to be consistent and invariable during daytime (Hoedjes et al., 2008). This assumption has been documented in several publications (e.g., Bastiaanssen et al., 2005; Crago et al., 1996; Brutsaert et al., 1992, Shuttleworth et al.,1989, Brutsaert and Sugita, 1992; Brutsaert and Chen, 1996).

Monteith and Unsworth, (1990) have demonstrated the potentials and the limits of using the evaporative fraction. The applicability of the self-preservation hypothesis is limited only to daylight hours when fluxes are widely estimated; the technique is not applicable at dawn or sunset and at night when the energy fluxes are relatively low, and the advective fluxes are strong (Brutsaert and Sugita,1992). However, such a limitation generally does not hinder the practical application of the self-preservation hypothesis because at night, except for rare cases, the latent heat flux is negligible or low, and evapotranspiration can be neglected, as documented by Sugita and Brutsaert (1991) and by Kustas and Norman (1996).

The evaporative fraction (Λ) is the ratio of the instantaneous latent heat flux (λET) to the available energy chosen as a reference integration variable ($\Lambda = Rn - G_0$) (Anderson et al. 1997).

The evaporative fraction is determined from instantaneous surface energy balance fluxes as follows:

$$\Lambda = \frac{\lambda ET}{Rn - G_0} \tag{2.7}$$

The self-preservation hypothesis makes Λ (dimensionless, ranging between 0 and 1) a proxy variable to integrate λ*ET* at hourly or daily scale from λ*ET* instantaneous values; thus, the daytime integration is a straightforward approach as the daily G_0 is negligible compared to daily R_n and the instantaneous value of Λ is supposed to be equal to the average daytime value (e.g., Maltese et al., 2013). Shuttleworth et al. (1989) analyzed Λ by using the data of four clear days on a relatively homogeneous lown showing that values of Λ at midday could well approximate the average daily value. Nichols and Cuenca (1993) found similar results using 72-day experimental data. Zhang e Lemeur (1995) found that in the absence of cloud cover, Λ is constant during daytime and Crago (1996) stated that the constant Λ hypothesis is surprisingly robust. However, varying cloud conditions and proximity to surface discontinuities may cause a significant change in Λ. Stewart et al. (1998) affirmed that upscaling methods using Λ are the best methods due to the possibility of using RS techniques in the estimation of actual evapotranspiration.

2.7.2 Incoming shortwave radiation as an upscaling reference variable

An alternative method to upscale λ*ET* is to use the proportionality between *ET* and incoming shortwave radiation, R_s, at daily scale (Jackson et al., 1983) as the solar radiation is the main source of energy for *ET*. This method uses R_s as an integrating factor, assuming that evapotranspiration variations are proportional to the incoming shortwave radiation, ($ET \propto R_s$):

$$\frac{ET_i}{ET_D} = \frac{Rs_i}{Rs_{24}} \tag{2.8}$$

where ET_i is the instantaneous evapotranspiration, ET_D is the daily evapotranspiration and $R_{s24,}$ and R_{si} are the mean daily and instantaneous

shortwave net radiations respectively. Although this method requires R_s as an additional input data, it has the advantage to be applicable even on partially cloudy days.

2.7.3 Upscaling daily evapotranspiration to longer periods using the reference evapotranspiration as an integration factor.

Reference evapotranspiration (ET_0) obtained at the meteorological stations can be used to further up-scales daily evapotranspiration over days within consecutive satellite images acquisitions (i.e. within a temporal window).

This approach assumes that actual daily evapotranspiration, computed at the image acquisition time, varying accordingly to the reference evapotranspiration (at the meteorological station) within a temporal window. Thus, ET_0 is used only as an index of the relative change in weather. As result, continuous daily ET values can be obtained and summed over a temporal window. Allen et al. (2007a) mentioned that one satellite image per month is sufficient to infer seasonal evapotranspiration value. However, Allen et al. (2007a) mentioned that during periods of rapid vegetation change, a more frequent image interval may be desirable.

2.8 Remote sensing optical Atmospheric Correction

Raw satellite sensors data are recorded as digital numbers (DNs); single raw images are recorded for each band of the electromagnetic spectrum (depending on the sensor spectral resolution). The digital number should be subjected to a series of correction preprocesses, that transform them into accurate retrievals surface reflectance.

In particular, sensors measure the electromagnetic energy reflected by earth that arrives to the satellite sensor itself. This measurement depends on the target reflectance, the incoming irradiance and it is also affected by atmospheric interaction. Thus, the calibration and the atmospheric correction process are required to convert DNs into reflectance values. Electromagnetic radiation interacts with the atmosphere in both visible and thermal parts of the electromagnetic spectrum.

In order to assess accurately the reflectance measured from a satellite sensor, the relative position between the sun and the sensor, the features of observed target and the atmospheric interaction should be taken into consideration.In the ideal case of absence of atmospheric contribution, the measured reflected energy only depends on the properties of the surface: a fraction of incident electromagnetic energy is absorbed, and the remaining is reflected back to space. However, within the atmosphere, two main processes modify the incoming and reflected solar radiation: absorption, and diffusion (scattering).

The electromagnetic radiation can be absorbed and converted to other forms of energy (mainly heat) by atmosphere gases components, such as water vapour (H_2O), ozone (O_3), oxygen (O_2), carbon dioxide (CO_2), methane (CH_4) and nitrous oxide (N_2O) and the other components as aerosols (e.g. dust) and liquid or solid water particles (e.g. cloud droplets and snow particles).

The scattering process is caused by aerosols and molecules present in the atmosphere where the electromagnetic energy changes its propagation direction due to interactions with the above-mentioned components. Scattering can be defined according to the dimensions of the particles forming a certain medium and their properties.

In addition, the surface could be Lambertian or non-Lambertian. The former reflects perfectly the entire incident radiation equally and uniformly into all directions with respect to the normal to the surface; on the contrary, a non-Lambertian surface need to be characterized by bidirectional reflectance functions (to be determined acquiring in situ spectral measures at different viewing angles). Figure 2.10 shows how surface and atmospheric scattering can affect the signal arriving at the remote sensing platform and, particularly the cases: I) when incident solar radiation component is wholly reflected by the surface and then directly transmitted to the sensor; II) the radiant energy arriving to the sensor is the result of diffusion at the surface and then directly transmitted to the sensor; III) the direct incident energy can be reflected by the surface and then diffusely transmitted to the platform sensor; IV) the energy transmitted to the sensor is the result of surface and atmospheric diffusion; V) the retrieved signal is the pure contribution of atmosphere.

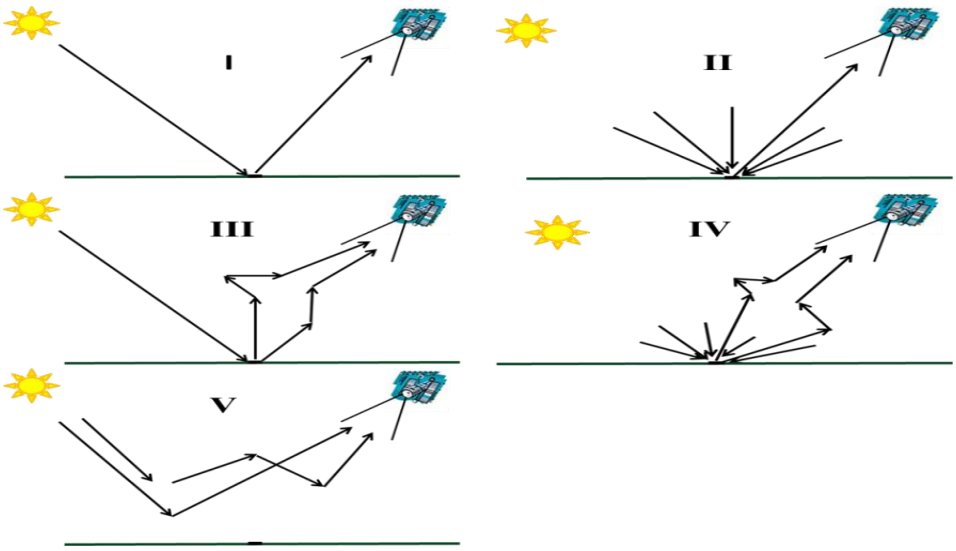

Figure 2.10: Effects of atmospheric and surface scattering on the signal retrieved by satellite

The following section illustrates the theoretical basis of atmospheric correction applied after the optical radiometric calibration of satellite remote sensing images. The atmospheric correction implies modeling of atmospheric effects, based on scattering and the absorption processes, as well as on interaction between these two processes.

Reflectance from a Lambertian surface will be defined by using the viewing direction zenith angle (θ_v) the azimuth angle (ϕ_v), the sun incidence angles (θ_s) and azimuth (ϕ_s), as shown in figure 2.11

The corrections for atmospheric interference are based on the state of the atmosphere. One of the most used models is the "Second Simulation of a Satellite Signal in the Solar Spectrum" (6S code). This code is used to assess the influence of atmosphere on the radiance recorded by the sensor and to simulate interactions between radiation and atmosphere (Vermote et al., 1997; Kotchenova et al., 2006, 2007 and 2008). The 6S code represents the most important and sophisticated model that can be applied for different satellite sensors (Tachiri, 2005) because it can estimate the atmospheric scattering better than other models (Zhao et al., 2000).

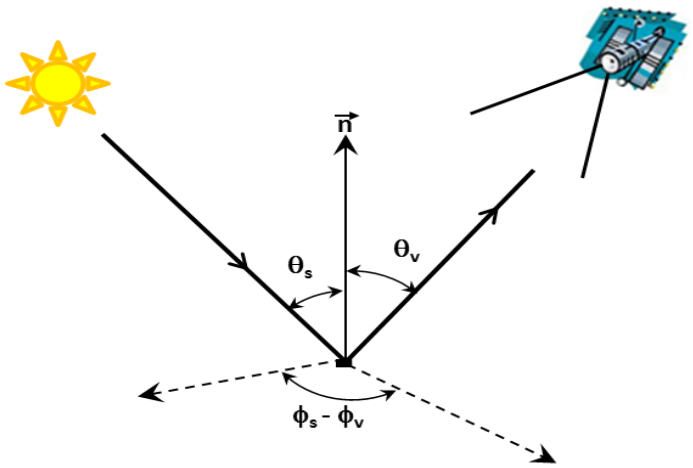

Figure 2.11: Reflectance defined by viewing angle θ_s and solar incidence angle θ_v

Research carried out by Sharma et al., (2008) evidenced that application of 6S has a great significance in deriving quantitative information from the satellite data.

Considering a Lambertian surface, gaseous absorption, and atmospheric conditions, the 6S code retrieves the surface atmospherically corrected reflectance value ρ_{ac} as follows:

$$\rho_{ac}(\theta_s, \theta_v, \phi_s - \phi_v) = \frac{\rho'_{ac}}{1+s\rho'_{ac}} \tag{2.9}$$

where the parameter ρ'_{ac} is defined as:

$$\rho'_{ac} = \frac{\frac{\rho_{TOA}(\theta_s,\theta_v,\phi_s-\phi_v)}{T_{gas}(\theta_s,\theta_v)} - \rho_{r+a}(\theta_s,\theta_v,\phi_s-\phi_v)}{T_{\downarrow}(\theta_s)T_{\uparrow}(\theta_v)} \tag{2.10}$$

where $\rho_{TOA}(\theta_s, \theta_v, \phi_s\text{-}\phi_v)$ is the at sensor apparent reflectance (top of atmosphere reflectance), $T\downarrow(\theta_s)$ and $T\uparrow(\theta_v)$ are the atmospheric transmittances in relation to the atmospheric path of the sun, the incidence solar zenith angle θ_s, the satellite viewing zenith angle θ_v; $T_{gas}(\theta_s, \theta_v)$ is the gaseous transmission and s is the spherical albedo of atmosphere and, finally, $\rho_{r+a}(\theta_s, \theta_v, \phi_s\text{-}\phi_v)$ is the atmospheric intrinsic reflectance (molecule +aerosol).

The top of atmosphere reflectance (ρ_{TOA}) is expressed as:

$$\rho_{TOA} = \frac{\pi . L_\lambda}{ESUN_\lambda . cos\,\theta_s . d_r} \quad (2.11)$$

where $ESUN_\lambda$ is the mean solar extra-atmospheric solar irradiance for each band, θ_s is the solar incidence angle (from nadir), and d_r is the inverse squared relative earth-sun distance. L_λ is the pixel value of spectral radiance at the sensor's aperture, obtained for the multispectral data from the DNs using the calibration *Gain* and *Bias* specific values provided by the owner of the satellite data.

The intrinsic atmospheric reflectance represents the aerosols and the Rayleigh scattering contributions. The aerosol scattering effect is not considered for the near-infrared bands (NIR) or at large θ_s and θ_v angles since the scattering effect is small.

For a Lambertian (isotropic) scattering, and without considering absorption, the molecular (Rayleigh) atmospheric reflectance (ρ_r) is expressed as (Chandrasekhar, 1960):

$$\rho_r(\mu_s, \mu_v, \phi_s - \phi_v) = \rho_r^1(\mu_s, \mu_v, \phi_s - \phi_v) + \left(1 - e^{-\tau/\mu_s}\right)\left(1 - e^{-\tau/\mu_v}\right)\Delta(\tau) \quad (2.12)$$

where μ_s is the cosine of the solar zenith angle (μ_s=cosθ_s), μ_v is the cosine of the viewing zenith angle (μ_v=cosθ_v), τ is the optical thickness of the atmosphere, $e^{-\tau/\mu}$ is the direct transmittance from surface to the sensor and from sun to surface defined with μ_s and μ_v, and $\rho_r(\theta_s, \theta_v, \phi_s\text{-}\phi_v)$ is the single scattering contribution and the second term of the equation accounts roughly for higher orders of scattering (Vermote et al., 2006).

The transmission function represents two streams (incident and reflected path) and is obtained using the delta-Eddington method as follows:

$$T_{(\mu)} = \frac{\left(\frac{2}{3} + \mu\right) + \left(\frac{2}{3} - \mu\right)e^{-\tau/\mu}}{\frac{4}{3} + \tau} \quad (2.13)$$

where μ is the cosine of the solar and viewing zenith angle.

Spherical albedo for conservative molecular scattering is given by:

$$s = 1 - \int_0^1 \mu T(\mu)\, d\mu \qquad (2.14)$$

Aerosol scattering occurs because of the effect of small aerosol particles suspended in the atmosphere. Aerosol scattering $\rho_a(\theta_s, \theta_v, \phi_s\text{-}\phi_v)$ is important to consider as a part of the atmospheric intrinsic reflectance. Vermote et al. (1997) mentioned that scattering properties of the aerosol layer can be calculated using the Sobolev (1975) multiple scattering approximations, and the transmittance can be obtained as addressed in Zdunkowsky et al. (1980). In 6S the spherical albedo is obtained by using a semi-empirical formula (Vermote et al., 2006). In order to correct the effects of gaseous absorption, different procedures have been suggested. Water absorption is assessed using a random exponential band as suggested by Goody (1952), whereas absorption of other gases are assessed by the random exponential band model developed by Malkmus (1967) whereas the total transmission is equal to the product of each gas transmission (Vermote et al., 2006).

2.9 Thermal radiometric calibration

Land surface temperature (*LST*) retrieval is crucial in SEB applications as it is one of the more important input in SEB models. Uncertainties in its estimation can lead to inaccurate retrieval of surface energy fluxes. Goetz et al. (1995) presented numerous factors that should be taken into account in order to assess the accuracy of surface temperature retrieval. Among them are the satellite sensor radiometric calibration, the atmospheric correction of the at-sensor signal and the correction for surface emissivity.

2.9.1 Sensor radiometric calibration

The thermal band is calibrated internally and onboard by a single onboard cavity blackbody and a black highly emissive shutter (Markham et al., 1997). The blackbody sits off the optical axis at a controlled temperature, and the shutter has on it a toroidal mirror, which reflects radiation from the blackbody onto the optics and through to the cooled focal plane. The non-mirror part of the shutter is coated with a high-

emissivity paint and sits at the instrument ambient temperature (Barsi et al., 2010). The internal calibration of the thermal band is done by using the gain and offset of the instrument.

The gain of the full system (G) is calculated from the internal gain determined by the calibration system (G_{in}) and the per-detector prelaunch-determined gain ratio (a):

$$G = aG_{in} \tag{2.15}$$

Moreover, the internal instrument gain is calculated from the blackbody and the shutter radiant exitances as follows:

$$G_{in} = \frac{Q_{bb} - Q_{sh}}{L_{bb} - L_{sh}} \tag{2.16}$$

where Q_{bb} is the average digital number of the internal calibration blackbody, Q_{sh} is the average digital number of the shutter, L_{bb} is the spectral radiant exitance of the blackbody calculated from the blackbody temperature, and L_{sh} is the spectral radiant exitance of the shutter calculated from the shutter temperature.

The offset (or biases) or the response of the system to zero radiance, (B), is calculated from per-detector prelaunch coefficients, the dark shutter responses, and the internal gain (G_{in}) as:

$$B = Q_{sh} - G_{in}(bL_{sh} - c) \tag{2.17}$$

where b and c are per-detector prelaunch-determined constants.

The obtained instrument gains (G) and biases (B) are used to convert the raw digital numbers (Q) in sensor's aperture scene spectral exitance (L_λ) as follows:

$$L_\lambda = \frac{(Q - B)}{G} \tag{2.18}$$

2.9.2 Atmospheric correction of the at-sensor signal

Signal emitted in the thermal region from an on-ground target is both weakend or enhanced by the atmosphere. The atmospheric correction,

used to remove the effects of the atmosphere in the thermal region, is an essential step to obtain the actual exitance of the surface. Atmospheric correction accounts for the fact that part of exitance of an observed object can be intercepted by the atmosphere, and that the part of the arriving signal to the satellite sensor can result from atmospheric or non-target contributions.

With an appropriate knowledge of the atmosphere and the presence of some ancillary meteorological data it is possible to estimate the transmission, the upwelling radiance, and the downwelling radiance and as a result, correct the surface-leaving radiance of a blackbody target at a kinetic temperature (T_B) from the at-sensor radiance. Barsi et al. (2003) developed a web-based tool (Atmospheric Correction Parameter Calculator) to obtain scene-based atmospheric correction parameters. It was shown that without atmospheric correction, surface temperatures could be misestimated within the range of ±2-3°K difference.

2.9.3 Surface radiometric temperature and correction for surface emissivity

The Stefan-Boltzmann law expresses the relationship between the radiation of an observed object and the surface temperature:

$$B = sT_B{}^4 \tag{2.19}$$

where B is exitance of a black body, s is the Stefan Boltzman constant [$5.67 * 10^{-8}$W.m^{-2}K^{-4}], and T_B is surface temperature of a black body [K].

Since the thermal band (band 6) of Landsat TM is too narrow to be used in the Stefan Boltzmann relationship (that considers a range 3.0 – 300 µm), the Plank theory has to be used:

$$B_\lambda = \frac{2\pi hc^2}{\lambda^5 \exp\left(\frac{hc}{k\lambda T_B}\right) - 1} \tag{2.20}$$

where B_λ is the intensity of spectral exitance of a black body per unit wavelength λ, h is the Plank constant [$6.626*10^{-34}$ J.s], c is the speed of light [$2.998*10^8$ m.s^{-1}], k is Boltzman constant [$1.381*10^{-23}$ J.K^{-1}].

The surface brightness temperature can be derived from the sensor's band 6 spectral exitance (*L6*) using a relationship analogous to the Planck formula (Markham and Barker, 1986).

Blackbody radiance corresponds to the radiation from a body in thermal equilibrium, and the emissivity of a black body is ε_o=1. The emissivity is used to account for the difference between natural surfaces and the theoretical black body. The gray body theory is used to indicate a deviation from ideality.

The land surface emissivity (ε_o) is the ratio of the thermal energy radiated by the surface to the thermal energy radiated by a blackbody at the same temperature. It is an indicator of the ability of a surface to emit energy, and its value ranges between 0 and 1. It is an important parameter in deriving the land surface temperature. This estimation of ε_o is curtailed since the lack of knowledge of emissivity can introduce an error to the *LST* retrievals. Prata et al. (1995) showed that the errors due to surface emissivity corrections could be twice the errors due to the atmospheric correction. The emissivity coefficient can be obtained in the absence of field data through an empirical relationship, by using the Normalized Difference Vegetation Index (NDVI).

2.10 Surface Albedo

Surface albedo (α) is the ratio between outgoing and incoming electromagnetic radiation, and it depends on the material of the reflecting surface; it is unit-less variable, ranging between 0 and 1, depending on the wavelength of the incident radiation. The surface albedo represents an important variable in SEB modeling because it is used to retrieve R_n; it is dependent on surface's reflectance signature, the angle of incidence and atmospheric characteristics.

Typical surface albedo range from 0.8, over a pure snow-covered area, to 0.1, over vegetation during the snow-free period (Jin et al., 2002) and to 0.05 for wet bare soil. Vegetated surfaces can have albedo values of about 0.20-0.25. (Allen et al. 1998). Table 2.1 shows the typical values of surface albedo (Morse et al., 1992).

Table 2.1: Typical values of surface albedo

Fresh snow	0.80 – 0.85
Old snow and ice	0.30 – 0.70
Black soil	0.08 – 0.14
Clay	0.16 – 0.23
White-yellow sand	0.34 – 0.40
Gray-white sand	0.18 – 0.23
Grass or pasture	0.15 – 0.25
Corn field	0.14– 0.22
Rice field	0.17 – 0.22
Coniferous forest	0.10 – 0.15
Deciduous forest	0.15 – 0.20
Water	0.25 – 0.348

2.10.1 Surface albedo obtained by RS Satellite Data

Kimes et al. (1984) showed how the error in obtaining spectral reflectance (ρ_λ) from values of nadir reflectance varies as a function of wavelength, solar zenith angle, LAI and structure of vegetation. Robinson, (1966) also verified the effect of solar zenith angle on albedo retrievals, especially for tall sparse canopies. The effect of solar elevation on surface reflectance was quantified by Menenti et al. (1989). Field measurements in the range of 0.3 to 2.5 μm on different types of surfaces have detected variations of α during the day.

For a given solar height, α can be expressed as:

$$\alpha = \int_{0.3}^{2.5} \frac{\left[\int_0^{2\pi}\int_0^{\pi/2} R_{s\uparrow}(\theta_s,\phi_s,\lambda).cos\,\theta_s.sin\,\theta_s d\theta_s d\phi_s\right]}{K_{\downarrow}(\lambda)} d\lambda \quad (2.21)$$

where 0.3 μm and 2.5 μm represent the integration limits over the solar spectrum (0.3–2.5 μm), $K_{\downarrow}(\lambda)$ [$Wm^{-2}sr^{-1}\mu m^{-1}$] is the incoming extraterrestrial radiance at the wavelength λ and $R^{\uparrow}(\theta_s, \phi_s, \lambda)$ indicates the solar reflected radiance [$Wm^{-2}sr^{-1}\mu m^{-1}$] at a wavelength λ that can be expressed as a function of the observation zenith angle (θ_s) [rad] and the azimuth (ϕ_s) [rad].

From an operational point of view, the evaluation of albedo can be done multiplying short-wave top-of-atmosphere reflectance, ρ_{TOA}, at some bands of the VIS-NIR region and corresponding weighting factors as:

$$\alpha_{TOA} = \sum_{i=1}^{n} \omega_i \cdot \rho_{TOAi} \quad (2.22)$$

where *n* represents the total number of sensor spectral bands (i).

The weighting factors (ω_i), estimated for an irregular distribution of solar radiation in the electromagnetic spectrum, are estimated as:

$$\omega_i = \frac{K_i^{\downarrow}}{\sum_n K_i^{\downarrow}} \quad (2.23)$$

where $K_i^{\downarrow}$ [$Wm^{-2}sr^{-1}\mu m^{-1}$] is the incoming extraterrestrial radiance for the specific band (i), derived from the theoretical extraterrestrial solar spectrum.

In order to obtain ground surface albedo, an atmospheric correction of α_{TOA}, is required. This is done by considering short wave one-way atmospheric transmissivity (τ_{sw}) and by subtracting from the α_{TOA} the $\alpha_{path\_radiance}$ which is approximately 0.03 as follows:

$$\alpha = \frac{\alpha_{TOA} - \alpha_{path-radiance}}{\tau_{sw}^2} \quad (2.24)$$

where the $\alpha_{path\_radiance}$ is the radiance resulting from backscattering by the atmosphere's particles and molecules.

2.11 Vegetation indices

Vegetation indices (VI) allow characterizing vegetated surface characteristics (e.g. biomass); they are used as a base input data for several environmental, hydrological, agricultural modeling processes. The vegetation indices can be measured in the field or can be estimated using remotely sensed images. Among vegetation indices largely used in remote sensing, SEB model considers the Normalized Difference Vegetation Index (NDVI), the Leaf Area Index (LAI) and the Vegetation Fractional Cover (f_c).

2.11.1 Normalized Difference Vegetation Index

The Normalized Difference Vegetation Index (NDVI) is computed by using the reflectivity values of VIS and NIR bands; thus it can be determined from multispectral images as presented by Rouse et al. (1974).

In particular, solar radiation is substantially absorbed by the plants in the wavelengths of the visible spectrum (380-780 nm). Chlorophyll in leaf tissues absorbs energy at all visible wavelengths and a little less in the green and, for this reason, the plants appear green. Whereas infrared radiant energy is not used by leaves, causing a peak of reflection. The more the vegetation is lush, the more energy is reflected in the near infrared (0.8 μm) so that decreases the reflection in the red region. This spectral response can be an indication of vegetation health where the difference between energy reflected in infrared and red increases proportionally to the health state of vegetation.

The Normalized Difference Vegetation Index can be defined as follows (Colwell, 1974):

$$\mathrm{NDVI} = \frac{(\rho_{NIR} - \rho_{RED})}{(\rho_{NIR} + \rho_{RED})} \tag{2.25}$$

Where ρ_{NIR} and ρ_{RED} are the near-infrared and red bands reflectance values respectively.

NDVI can be a valuable index to discriminate vegetated from bare soils and bare soil from water bodies. It ranges between -1 and 1, and it is an

indicator of green vegetation health status. NDVI is the most commonly used vegetation index.

2.11.2 Leaf Area Index

Leaf Area Index (LAI) is the ratio of vegetation leaf surface and a unit ground surface to which vegetation is projected. LAI is a dimensionless variable [m^2 m^{-2}]. As vegetation cover increases, LAI increases. It is an important ecological index that defines the vegetation structural properties. If computed as a function of VI it is related to the green vegetation area that interacts with the atmosphere, thus the interface area for energy and mass exchange (LSASAF, 2008). LAI is an important indicator used to monitor the dynamic of vegetation and to define processes such as evapotranspiration, rainfall interception and photosynthesis.

Techniques to estimate LAI can be "destructive" by collecting and measuring vegetation leaves (e.g., Thom, 1971) and "non-destructive", by measuring light crossing vegetation with optical tools. In the latter case LAI is estimated by the fraction of solar radiation transmitted below a canopy and the intercepted solar radiation above the canopy (Miller, 1967).

As shown by numerous studies, an alternative method using NDVI can provide good estimations of LAI (Colombo et al. 2003; Van Wijk and Wilk et al., 2005; Steltzer and Welker 2006).

2.11.3 Vegetation fractional cover

Vegetation fractional cover (f_c) accounts for the fraction of soil surface area covered by green vegetation normalized over a unit area. It is an important parameter that reflects the spatial degree of vegetation distribution and therefore the fraction of vegetation in each pixel. This variable can assume values ranging between 0 and 1 and can be estimated based on NDVI (Choudhury et al., 1994).

The fractional cover is an important variable in SEB models employed to differentiate between evapotranspirating vegetative surface and evaporating soil surface. The latter, that is proportional to f_c, allows evaluating evapotranspiration from vegetation, whereas the former, proportional to (1- f_c) allows evaluating soil evaporation.

Chapter 3: Materials

In this chapter, the two experimental sites will be described. The first site is the "SAT Llano Verde" agricultural irrigated district, located in the Spanish province of Albacete analyzed for three years. The second irrigation district is located near to the city of Castelvetrano, province of Trapani, Italy. This irrigation district, named "1/A" and managed by "Consorzio di Bonifica di Agrigento 3", was examined for two years. This chapter firstly depicts the geographic location, irrigated areas, irrigation system, climatic characteristics, crop distribution, irrigation water consumption of both the studied areas. Then, the satellite multispectral dataset used for the SEB applications is finally described.

3.1 The SAT Llano Verde irrigated district

3.1.1 Case study localization

The study area, represented by the irrigation district SAT Llano Verde, is located in the province of Albacete (Central Spain), in Castilla-La Mancha region.

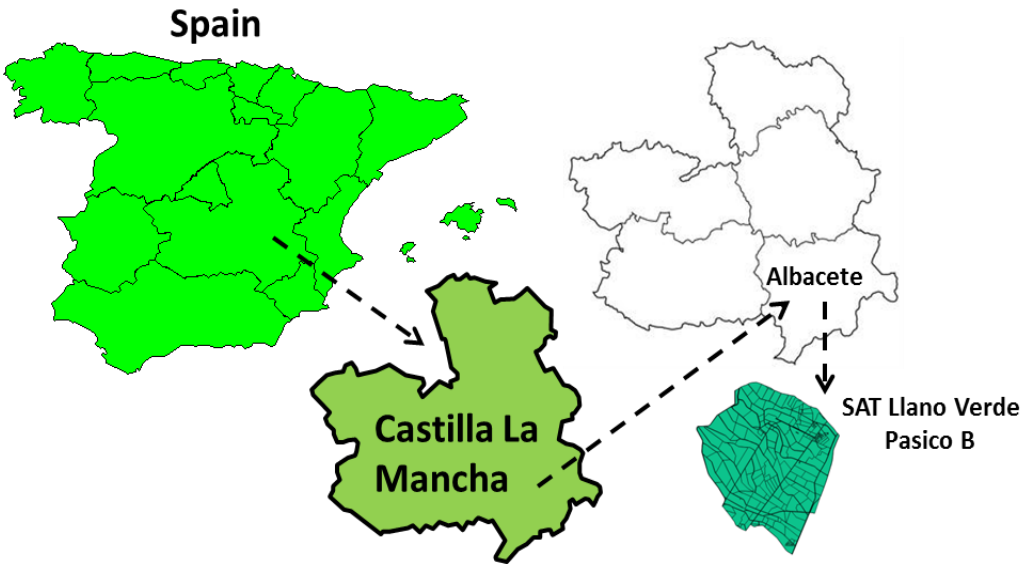

Figure 3.1: Location of Sat Llano Verde irrigation district in Albacete province, region of Castilla la Mancha, Central Spain.

3.1.2 Irrigated area characteristics

Irrigation district consists of two collective pressurized irrigation networks fully automated, watering an area of 1506 ha characterized by a flat landscape. The district is divided into two independent sectors, named “Pasico A” and “Pasico B” (643 and 863 ha, respectively).

The study is carried out on Pasico B sector, where predominant farm sizes (51%) extend more than 5 ha, with only 21% exceeding 8 ha. The average plot size is 5.52 ha, with a wide range of plots extended from 0.13 to 19 ha.

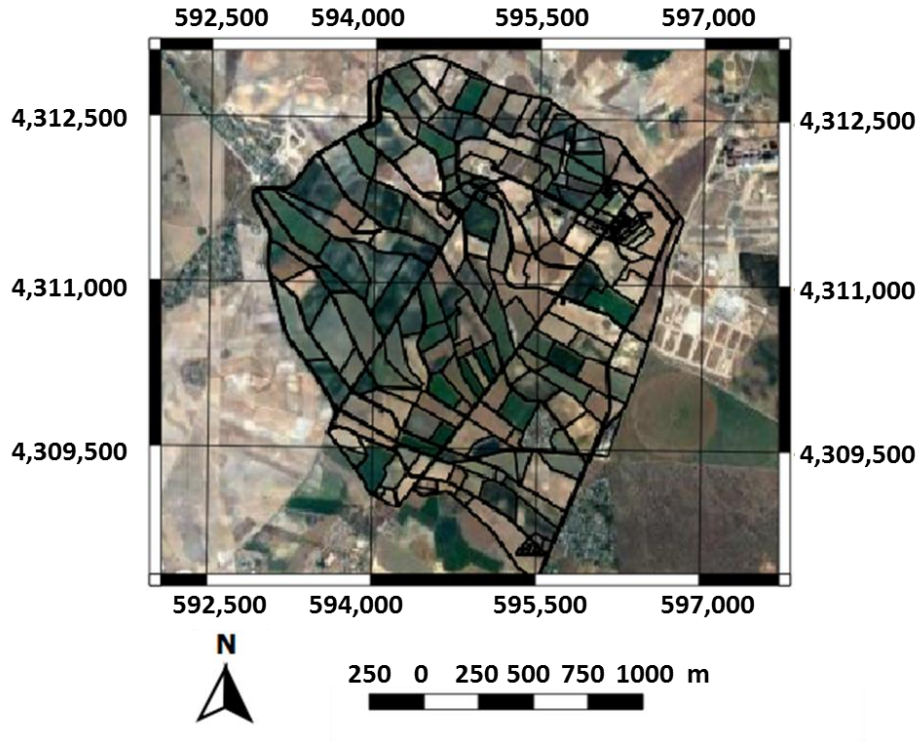

Figure 3.2: Geographic location (UTM-ED50, Zone 30 N) of SAT Llano Verde irrigation district.

Groundwater represents the primary source of water for irrigation. Water is extracted through three wells, and it is stored in a reservoir having a capacity of 130,000 m^3, used to feed the network during the periods of maximum demand. The extraction is carried out by using submerged pumps, characterized by power ranging between 320 and 380 kW. Water is pumped to the network from a pumping station in which 11 pumps of 154 kW are installed in parallel; one of them operates with a variable speed drive, while the remaining with electronic starters. Manometric regulation is applied in the region with pressure transducer set to 5.3 bar at the output of the collector pipe.

Irrigation network is designed to distribute in turn. The degree of automation in the area is high, up to the level of hydrants. Irrigation network consists of Polyvinyl chloride (PVC) pipes, with diameters

variable from 160 and 400 mm, as well as fiber cement, for larger diameters up to 900 mm. Most of the area (99%) is irrigated by sprinklers and only a small percentage by drip irrigation systems. The figures below show the irrigated fields and the irrigated crops distribution in the district during irrigation seasons 2006, 2007 and 2008.

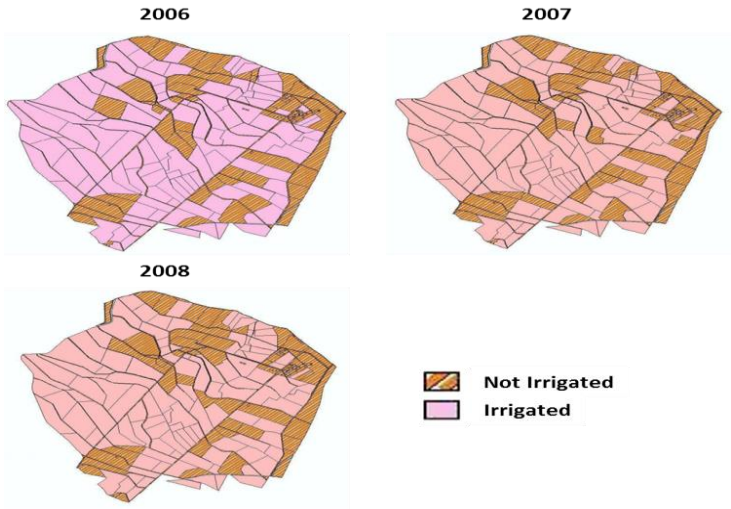

Figure 3.3: Irrigated and non-irrigated fields of SAT Llano Verde irrigation scheme during irrigation seasons 2006, 2007 and 2008.

3.1.3 Crop distribution and irrigation water consumption

Main cultivations are corn, alfalfa, barley, onion and wheat, with few vine groves (figure 3.4). Crops are usually cultivated in rotation with more than one cycle per year.

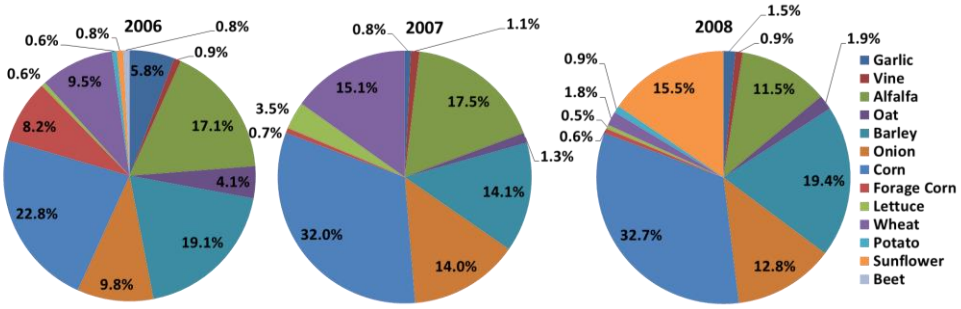

Figure 3.4: Crop distribution (% of irrigated surface) in irrigation seasons 2006, 2007 and 2008.

The total irrigation water consumption monthly distributed in the district is shown in figures 3.5, 3.6 and 3.7

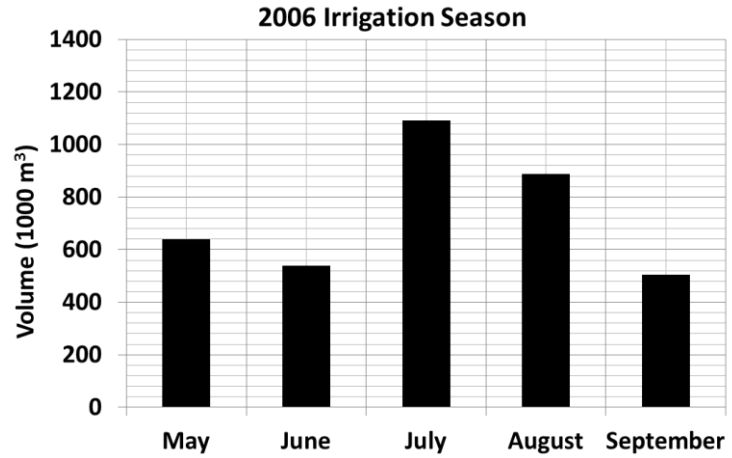

Figure 3.5: Monthly irrigation water consumption measured at SAT Llano Verde district during irrigation season 2006.

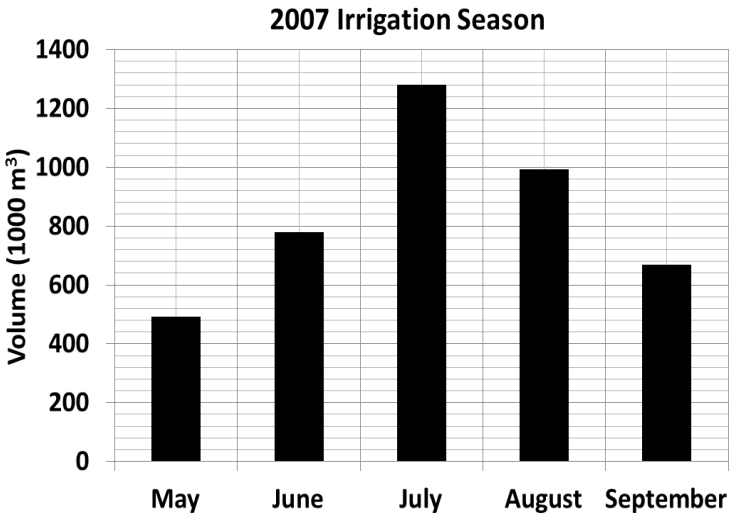

Figure 3.6: Monthly irrigation water consumption measured at SAT Llano Verde district during irrigation season 2007.

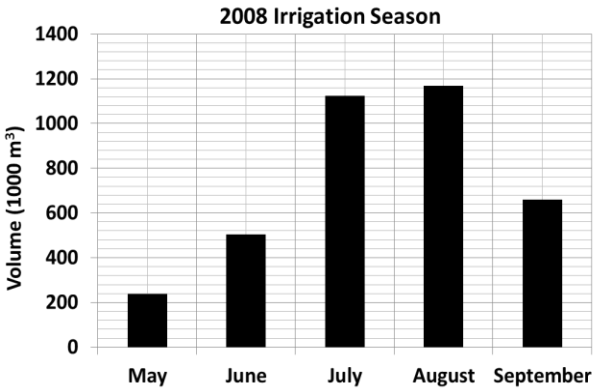

Figure 3.7:Monthly irrigation water consumption measured at SAT Llano Verde district during irrigation season 2008.

3.1.4 Climatic characteristics and meteorological data

A typical temperate Mediterranean climate characterizes the study area. According to the climatic classification, the local climate is semiarid, with dry, hot summers and relatively moderate wet winters. On average, August is the month characterized by the mean minimum precipitation and the mean highest temperatures 9.18 mm and 32.89 °C, respectively, while May is usually characterized by the occurrence of the highest precipitation (41.83 mm).

In the SAT Llano Verde irrigation district, meteorological data were obtained from the Irrigation Advisory Service (IAS) (Oretga et al., 2005). This network consists of 361 stations, 42 of which are located in Castilla-La Mancha region. In the present thesis, hourly weather data collected by the agrometeorological station located in "Los Llanos," in the province of Albacete, were used (UTM **X:** 595166 and **Y:** 4311730). The weather station is composed of a set of devices to monitor standard meteorological variables, such as air temperature, relative air humidity, precipitation, wind speed and direction and solar radiation. Meteorological daily data registered during irrigation seasons (from May to September) 2006, 2007 and 2008, are shown in figures 3.8, 3.9 and 3.10, respectively.

For each year, in particular, the mean daily air temperature, *T* (°C), air relative humidity, *Hr* (%), global solar radiation, *Rs* (MJ m^{-2}), wind speed, *V* (m s^{-1}), as well as reference evapotranspiration, ET_0 (mm), are shown. The latter variable was determined according to the Penman-Monteith equation (Allen et al. 1998). Vertical black bars identify the days of satellite images acquisitions.

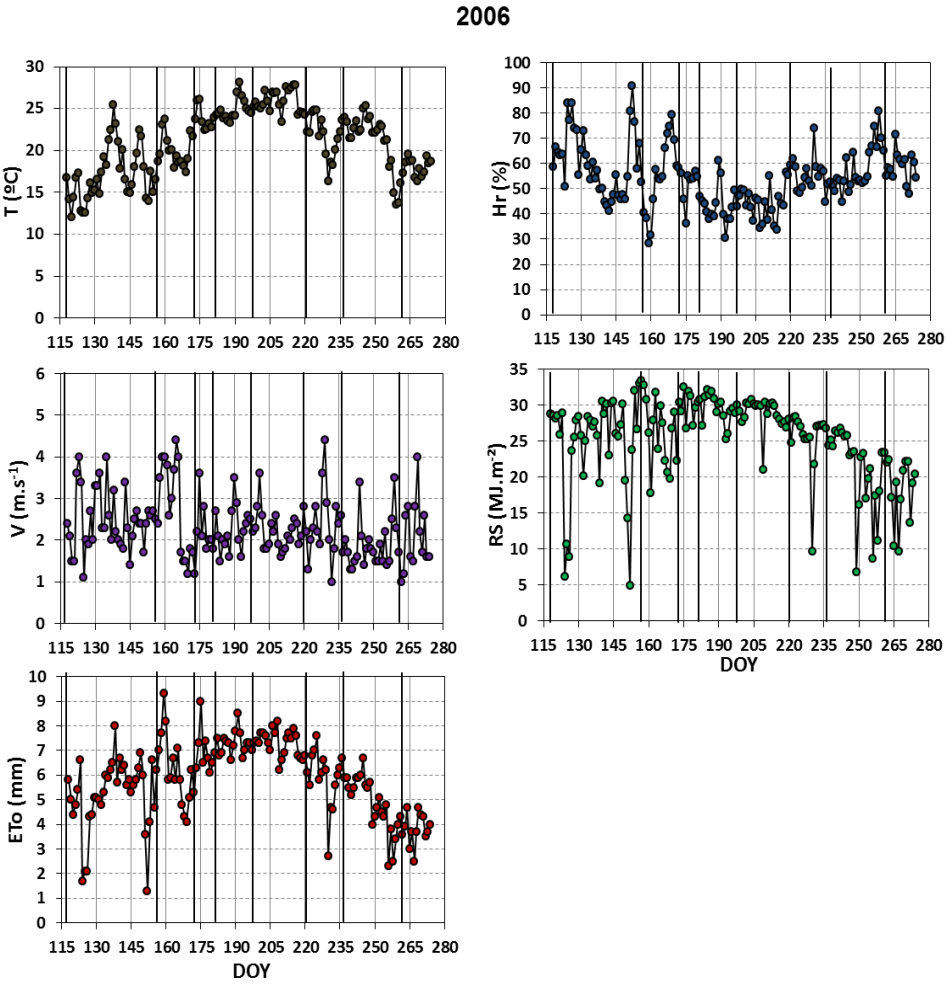

Figure 3.8: Los Llanos Albacete meteorological data for Irrigation season 2006. Vertical black bars identify the satellite images acquisition days.

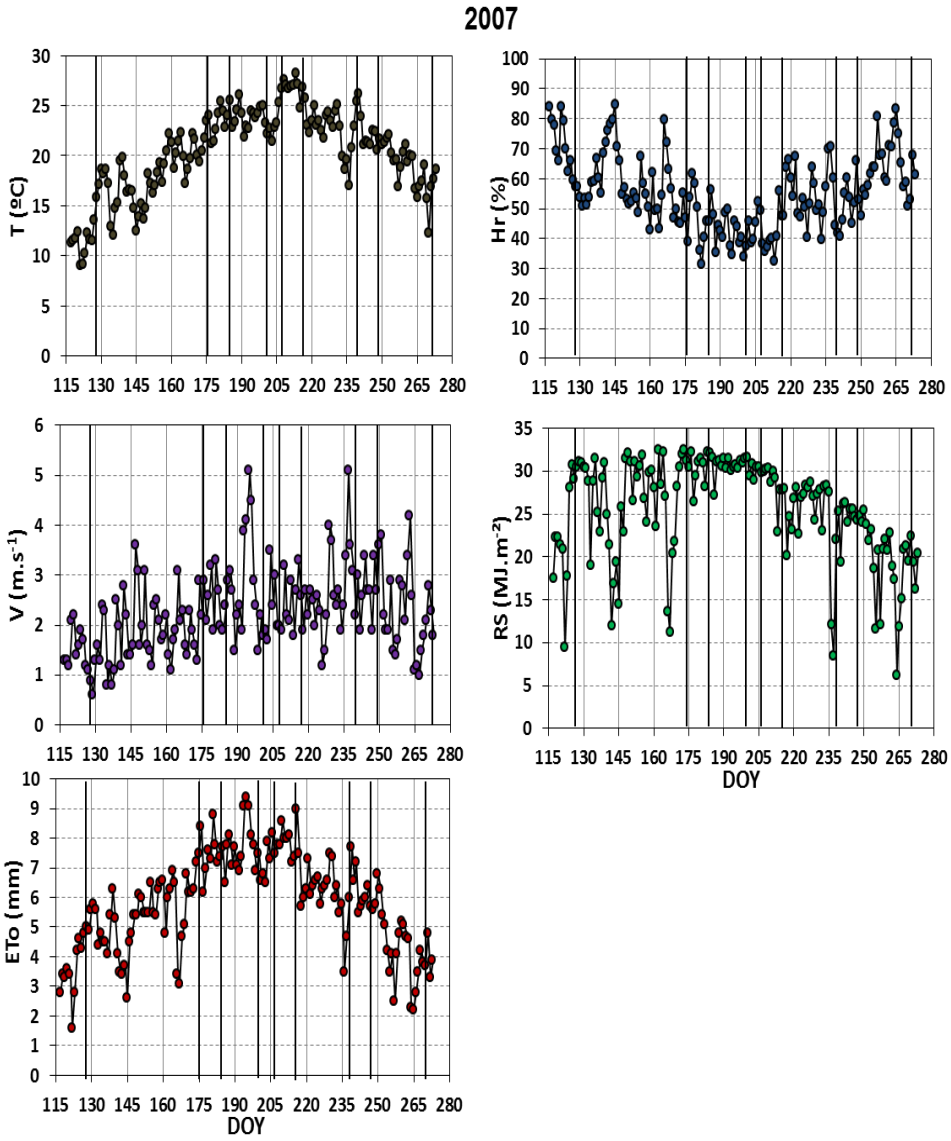

Figure 3.9: Los Llanos Albacete meteorological data, Irrigation season 2007. Black vertical bars identify the satellite images acquisition days.

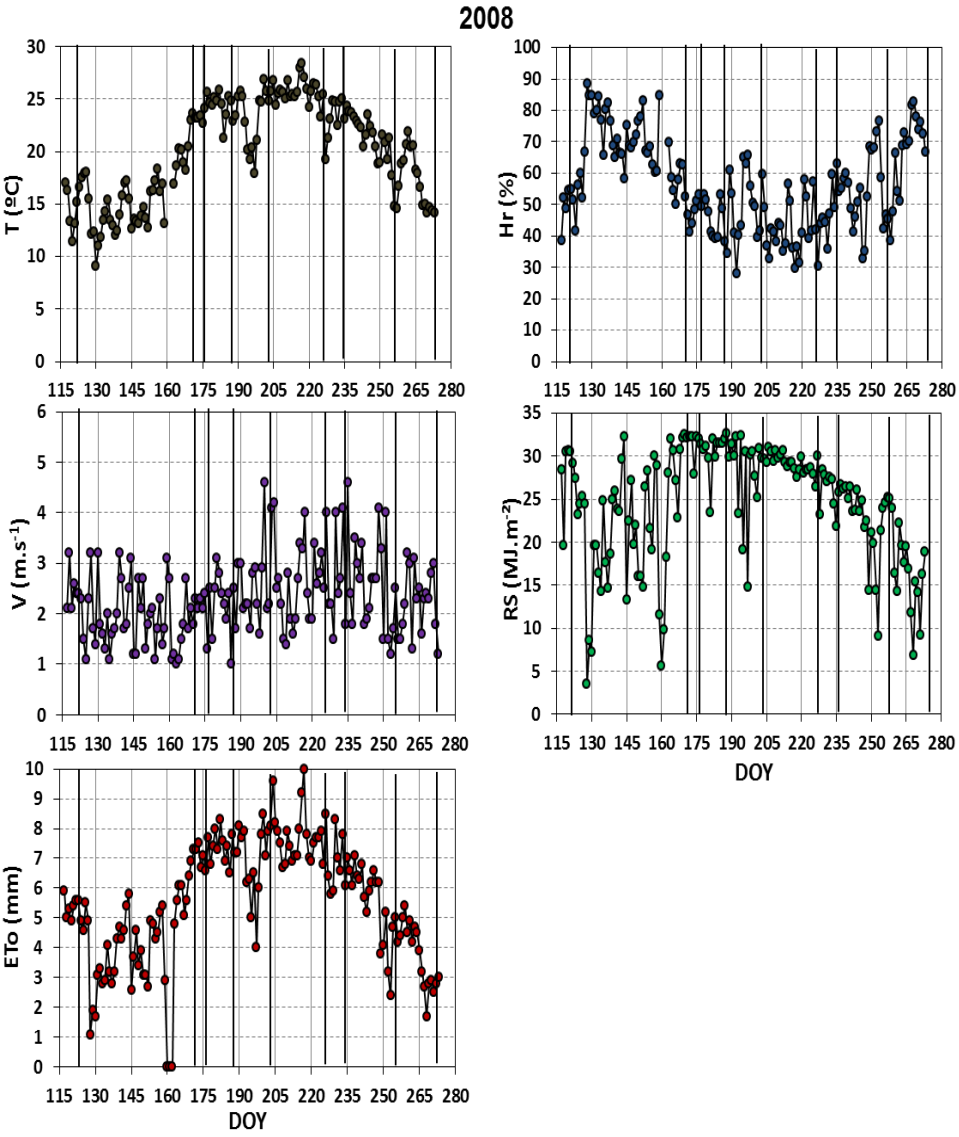

Figure 3.10: Los Llanos Albacete meteorological data, Irrigation season 2008. Black vertical bars identify the satellite images acquisition days.

3.2 Consorzio di Bonifica "Agrigento 3."

3.2.1 Localization of the study area

The study area is represented by a district, named "1A", managed by Consorzio di Bonifica "Agrigento 3". The district is located near to the town of Castelvetrano, in South-West of Sicily island, Italy.

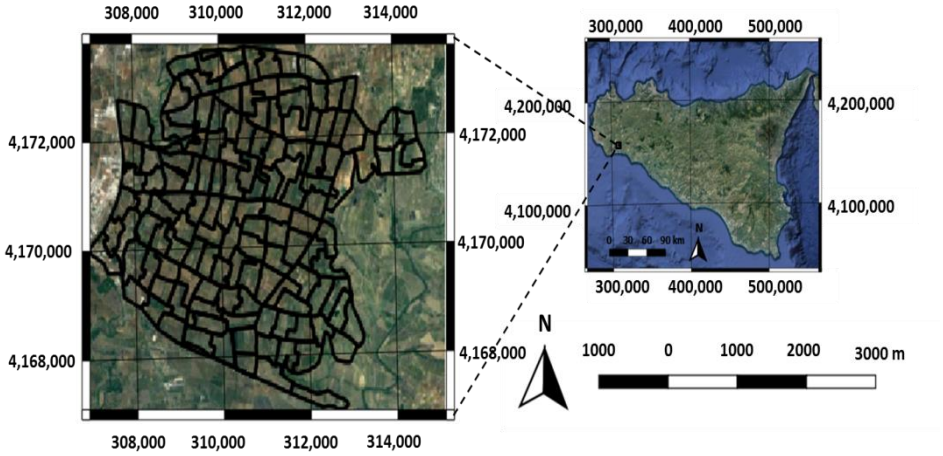

Figure 3.11: Geographic location (UTM-ED50, Zone 33N) of District 1A managed by Consorzio di Bonifica "Agrigento 3", Sicily, Italy.

3.2.2 Characteristics of irrigated area

The district 1A is part of a larger extension (9079 ha) managed by the Consortium, interesting fractions of the territories of Partanna, Castelvetrano and Campobello di Mazara municipalities, in the province of Trapani. District 1A, falls on the northern side of the irrigated area and covers a surface of 2745 hectares.

The irrigation service was activated in 1992 after the construction of a dense pipe-network extending approximately 214 km, and designed to deliver water from the reservoir to hydrants. The network is divided into main, secondary and tertiary pipelines with different materials (steel, Glass Fiber Reinforced Plastic (PRFV), asbestos cement and PVC and various diameters.

Irrigation network is feeded, by gravity, by two loading reservoirs, the first of which named 1/A1 has a volume about 24,000 m^3 and is located at about 240 m a.s.l., whereas the second, named 1A/2, placed at 190 m a.s.l., is characterized by a volume of about 27,000 m^3.

Water derived from the main adductor of the Garcia lake is pumped into the two reservoirs by a set of pumps working with variable speed drive installed at the "Zangara" pumping station.

The water distribution network serves 139 sectors for a total of more than 2,000 water users. The distribution network was designed for on the rotational water distribution in each irrigation sector, that means that the whole flow is diverted to the hydrants according to a fixed turn. Hydrant discharge is equal to 15 l s^{-1}, with a minimum pressure of 2.5 bars. Water distribution management is totally automated through a remote control system. Volumetric water consumptions distributed in each sector are controlled and registered by a central control unit. The most common farm distribution system is drip and secondly sprinkler irrigation.

3.2.3 Crop distribution and irrigation water consumption

The area is characterized by highly fragmented agriculture, predominantly cultivated with olive orchards, vineyards with the sporadic presence of citrus and fruit orchards. Distribution of irrigated crops in 2009 and 2010 is illustrated in figure 3.12.

The water volumes delivered in each hydrant located within the district is registered on a paper format user card. For each user, the personnel of the Consortium located in Castelvetrano registers a paper sheet, containing all the user's information necessary to draw up an effective irrigation plan for each irrigation season. In each form, information regarding the location of the farms within the district, the crop distribution, the date of irrigation and the volume of water delivered are registered. Fig. 3.13 shows an example of one user form.

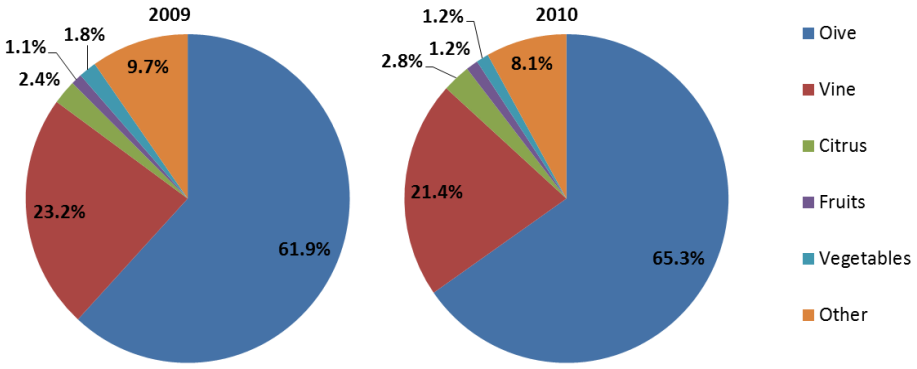

Figure 3.12: Crop distribution (% of irrigated surface) in the district 1A during irrigation seasons 2009 and 2010.

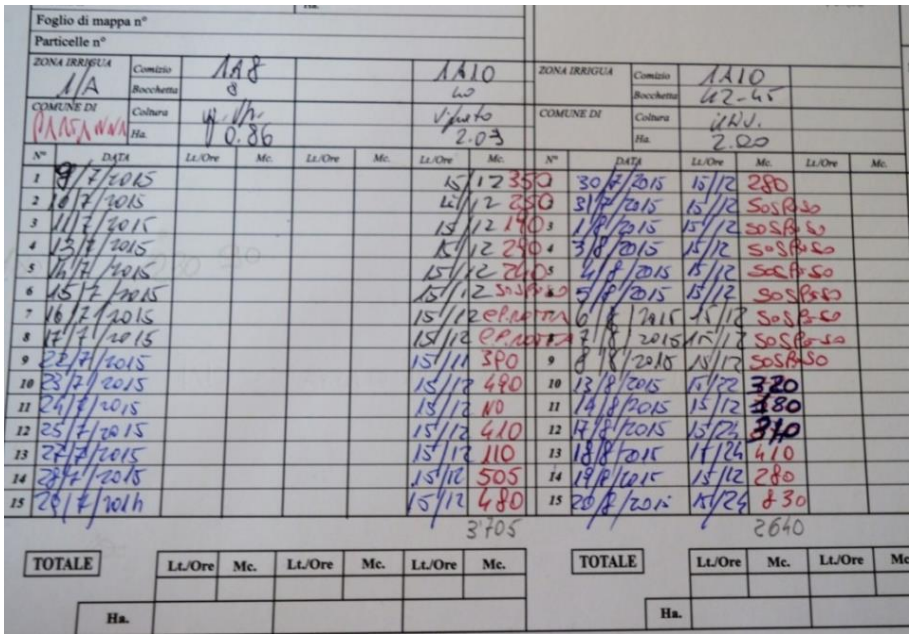

Figure 3.13: Example of the paper sheet referred to one user.

The total monthly water consumption distributed by the hydrants installed in the district is shown in figures 3.14 and 3.15.

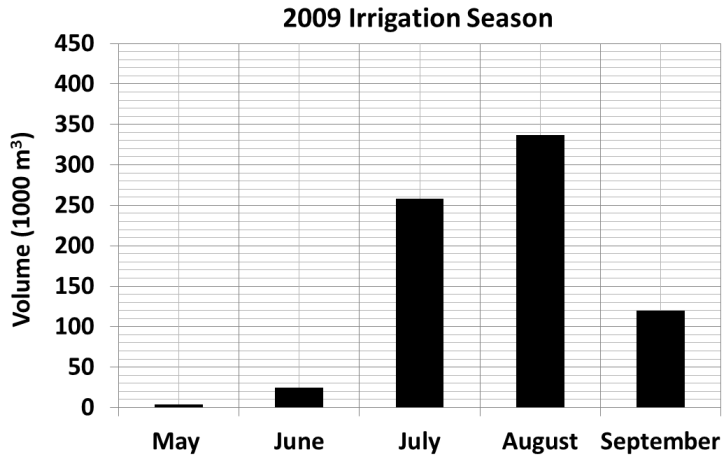

Figure 3.14: Monthly irrigation water consumption measured in District 1A during irrigation season 2009.

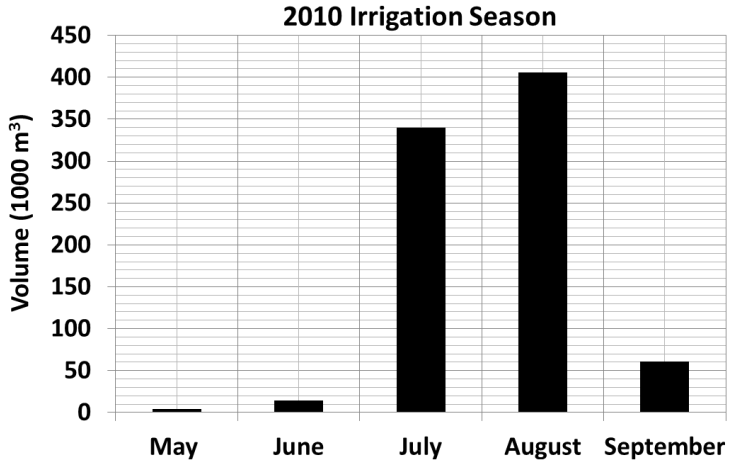

Figure 3.15: Monthly irrigation water consumption measured in District 1A during irrigation season 2010.

3.2.4 Climatic characteristics and meteorological data

The island of Sicily is located in the Mediterranean basin. In the island, the annual precipitation ranges between 350 and 1,200 mm, whereas temperature varies between 4 and 36°C. This variability is related to the different altitude and exposure.

From a climatic standpoint, the study area of Castelvetrano is characterized by a phase shift between the crop phenological (growth) cycle and the rainfall events; there is generally high evaporative demand during summer and the contextual absence of precipitation. On average, the total annual rainfall in the study area is variable between 450 and 1000 mm, with annual reference evapotranspiration, evaluated according to the methodology indicated in the FAO-56 paper (Allen et al., 1998), slightly higher than 1000 mm.

3.2.4.1 Castelvetrano agro-meteorological station

Meteorological variables were recorded within the study areas by an automatic weather station during two irrigation seasons (from 1st of May to 30th of September), 2009 and 2010. The meteorological station belongs to the Sicilian Agrometeorological Information Service (SIAS) and is part of a network of 94 remotely controlled weather stations installed throughout the island. The weather station provides standard meteorological variables, such as air temperature, relative air humidity, precipitation, wind speed and direction, atmospheric pressure and global solar radiation. In this area, reference evapotranspiration is calculated by using meteorological data. In order to estimate actual evapotranspiration and to assist farmers and agricultural technicians for irrigation water management, SIAS suggests the use of a web platform in which a simplified agro-hydrological model, IRRISIAS, is implemented. The model is based on the "dual crop coefficient" procedure described in the FAO-56 paper (Allen et al., 1998).

Meteorological data obtained from the station of Castelvetrano for irrigation seasons 2008 and 2009 are shown in figures 3.16 and 3.17, in which T (°C) is the mean air temperatures, Hr (%) is the mean relative humidity, V is the mean wind speed (m s^{-1}) at 2.0 m height, R_s (MJ.m^{-2}) is the mean global solar radiation and finally, ET_0 (mm) is the daily

Penman-Monteith reference evapotranspiration. The black vertical bars identify the days of satellite images acquisition.

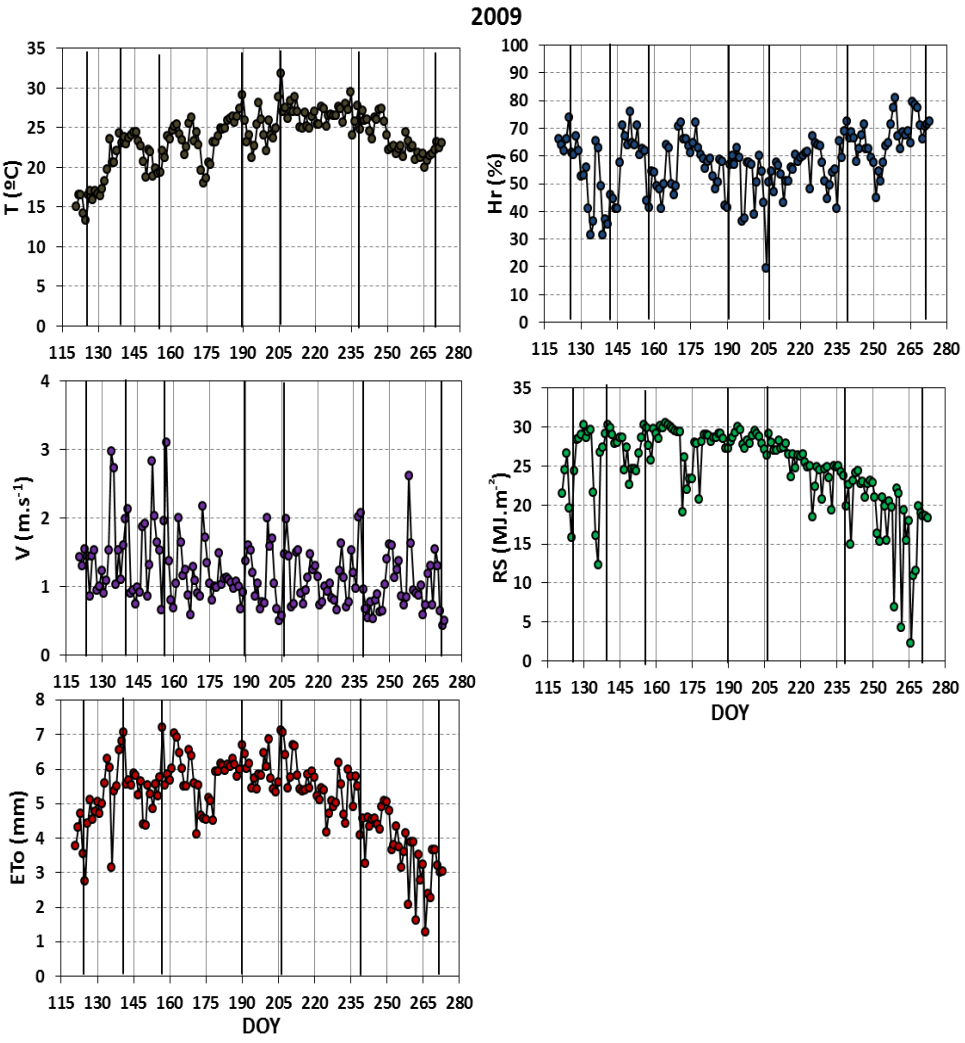

Figure 3.16: Climate daily data registered by the weather station of Castelvetrano, during irrigation season 2009. Black vertical bars identify the satellite images acquisition days.

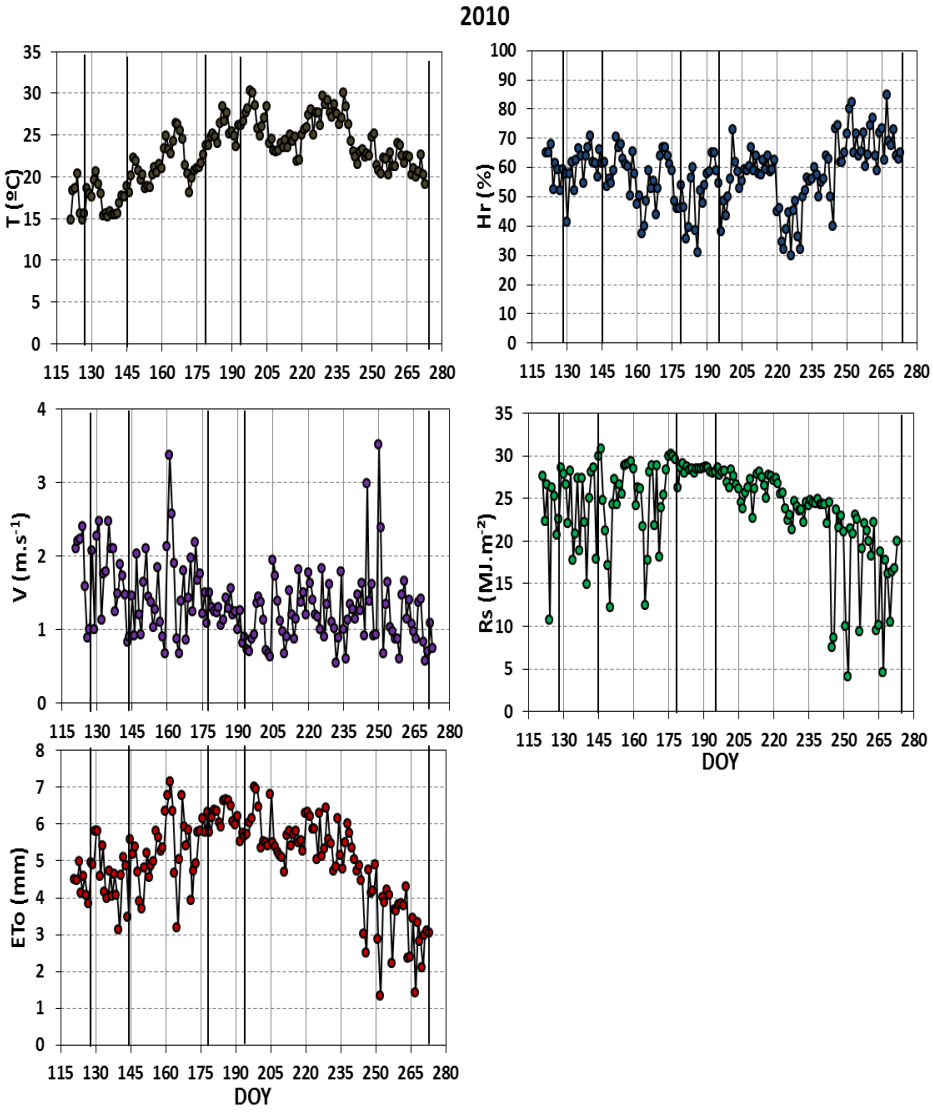

Figure 3.17: Climate daily data registered by the weather station of Castelvetrano, during irrigation season 2010. Black vertical bars identify the satellite images acquisition days.

3.2.4.2 Flux Tower (FT) and Micro-Meteorological measurements

In 2009 and 2010, micro-meteorological variables were also monitored by a flux tower. For research purposes, the tower, having a height of about 10 m, was installed in an olive orchard having coordinates of (UTM WGS84 33S 310044 m E, 4168419 m) and an elevation of 121 m a.s.l. Data acquired by the FT, allowed monitoring H and λET by using the Eddy Covariance (EC) technique with an integration time-step of 30 minutes. The flux tower, shown in fig. 3.18, was equipped with:

- A three-dimensional sonic anemometer (CSAT3-3D, Campbell Scientific Inc. - Logan, UT, USA) providing high-frequency (20 Hz) wind speed at 5.6 m a.g.l.
- An open-path infrared gas analyzer (LI7500, Li-cor Biosciences Inc. Lincoln, NE, USA) installed at the height of 5.6 m a.g.l., registering the fluctuation of vertical wind speed and the densities of water vapor and carbon dioxide with a frequency of 20 Hz.
- Four components net radiometer (*CNR1*, Kipp & Zonen-The Netherlands) positioned 8.5 m a.g.l., measuring the direct shortwave radiations, the reflected shortwave radiations, the direct longwave radiations, and the reflected longwave radiations.
- Sensors to monitor relative air humidity and air temperature.
- Two Pyranometers (IR Precision Infrared Thermocouple Sensor, IRTS-P, Campbell Scientific Inc.) installed at 4.80 m a.g.l. and measuring the soil and vegetation surface radiometric temperatures.
- Two self-calibrated soil heat flux plates (HFP01, Hukseflux) installed 0.1 m below ground level measuring the ground heat flux.
- A reflectometer (CS-616, Campbell Scientific Inc.) measuring the volumetric soil water content at a soil depth of 0.25 m.

Figure. 3.18: Flux tower installed in the study area

Regarding the flux tower, it is essential to mention the presence of data gaps in the periods from 11th to 20th of June and from 3rd to the 15th of August in 2009, and from 4^{rth} to 10th of July, from18th to 20th July and from 25th to 20th of September in the season 2010. The lack of data was often due to power failures.

3.3 Images data acquisition and setting up

Land Remote Sensing Satellite (LANDSAT) has been one of the primary operational Earth observation satellites over the past three decades. Landsat images have been widely used in estimating *ET* from field to regional scale. The images collected by Landsat are used in this research application. Landsat repository provided moderately high-resolution images valuable for the estimation and the discrimination of *ET* among crops and fields within the irrigation districts, SAT Llano Verde and district 1A. Fields size are typically on the order of few hectares in both the study areas. The coarser pixel resolution characterizing satellite images could not be used to discriminate *ET* of individual small fields. Landsat-5 Thematic Mapper (TM) images of both study cases were selected from nearly cloud-free scenes. One satellite image per month is usually considered sufficient for estimating seasonal *ET*, since monthly estimates are based on only one or two satellite images per month (Allen et al., 2007a).

The TM sensor images consist of 6 bands covering the visible and near-infrared (NIR) wavelengths (Bands 1-5 and 7) with a spatial resolution of 30 meters. The sensor also has a thermal band (Band 6), acquired at the 120-m spatial resolution and, after resampling, provided at 30-m resolution. The approximate scene size is 170 km in North-South direction and 183 km in East-West direction. More detailed information on Landsat 5 TM bands, wavelengths and resolution is shown in table 3.1.

Table 3.2: Landsat Thematic Mapper (TM) sensor bands, wavelengths and spatial resolution.

Landsat TM Band	Wavelength (μm)	Spatial Resolution (m)
Band 1 – Blue	0.45-0.52	30
Band 2 – Green	0.52-0.60	30
Band 3 – Red	0.63-0.69	30
Band 4 – Near Infrared (NIR)	0.76-0.90	30
Band 5 – Shortwave Infrared (SWIR) 1	1.55-1.75	30
Band 6 – Thermal Infrared	10.40-12.50	120* (30)
Band 7 – Shortwave Infrared (SWIR) 2	2.08-2.35	30

Landsat-5 has a revisit period of 16 days. In the SAT Llano Verde irrigation scheme, a total of 26 satellite images (Path 199 and 200, Row 33) were select to represent the three irrigation seasons (2006, 2007 and 2008). As the study area is covered by two scenes, it is possible to obtain more than two images per month. For district 1A, instead, only 7 images (Path 190 and Row 34) were selected to analyze the irrigation seasons 2009 and 2010. The TM images (cloud-free over the case study) were downloaded from the United States Geological Survey (USGS) Earth Explorer website; detailed information on the TM images used in both the case study are presented in Tables 3.2 and 3.3.

Table 3.3: Landsat TM images representing the SAT Llano Verde (Spain) during irrigation seasons 2006, 2007 and 2008.

Image	Acquisition Date (dd/mm/yyy)	Acquisition Time UTC (Scene Center) (hh:mm)	Pass	Row	Cloud Cover (%)	Sun Azimuth (° CW from North)	Sun Elevation Angle (°)
1	27/04/2006	10:35	199	33	2	136.7	58.5
2	05/06/2006	10:42	200	33	0	125.1	65.3
3	21/06/2006	10:42	200	33	3	122.4	65.4
4	30/06/2006	10:36	199	33	0	122.2	64.9
5	16/07/2006	10:36	199	33	0	124.3	63.3
6	08/08/2006	10:43	200	33	4	131.6	59.4
7	24/08/2006	10:43	200	33	29	138.3	55.7
8	18/09/2006	10:37	199	33	33	148.3	48.5
9	07/05/2007	10:44	200	33	2	134.7	61.3
10	24/06/2007	10:43	200	33	0	122.6	65.5
11	03/07/2007	10:37	199	33	0	122.7	64.9
12	19/07/2007	10:37	199	33	6	125.1	63.0
13	26/07/2007	10:43	200	33	0	127.1	61.9
14	04/08/2007	10:37	199	33	0	130.1	60.3
15	27/08/2007	10:43	200	33	30	139.3	55.0
16	05/09/2007	10:36	199	33	47	143.0	52.5
17	28/09/2007	10:42	200	33	0	151.4	45.3
18	02/05/2008	10:32	199	33	4	133.8	59.5
19	19/06/2008	10:31	199	33	1	120.5	64.6
20	26/06/2008	10:37	200	33	0	120.1	64.2
21	05/07/2008	10:30	199	33	0	120.4	63.5
22	21/07/2008	10:30	199	33	9	123.2	61.4
23	13/08/2008	10:35	200	33	2	131.0	57.1
24	22/08/2008	10:29	199	33	27	134.7	55.0
25	14/09/2008	10:34	200	33	1	143.9	48.6
26	30/09/2008	10:34	200	33	5	149.4	43.5

Table 3.4: Landsat TM images representing the district 1A (Italy) during irrigation seasons 2009 and 2010.

Image	Acquisition Date (dd/mm/yyy)	Acquisition Time UTC (Scene Center) (hh:mm)	Pass	Row	Cloud Cover (%)	Sun Azimuth (° CW from North)	Sun Elevation Angle (°)
1	05/22/2009	9:36	190	34	0	124.42	63.9
2	06/07/2009	9:36	190	34	3	119.77	65.2
3	07/25/2009	9:37	190	34	0	122.55	61.9
4	08/26/2009	9:37	190	34	0	135.83	55.5
5	05/09/2010	9:39	190	34	0	130.10	62.1
6	06/26/2010	9:38	190	34	0	118.15	65.3
7	07/12/2010	9:38	190	34	0	119.59	63.9

Chapter 4: Methods

4.1 Satellite images pre-processing

For both case study, Landsat Thematic Mapper (TM) images (cloud-free over each case study) were used to create subset images that were processed to produce layered spectral band images, necessary to apply the SEB models. For each pixel, Landsat TM sensors capture a signal proportional to the spectral radiance (shortwave bands) and to the spectral exitance (longwave bands), taking advantage of the photoelectric effect. This electrical signal represents the Top Of Atmosphere (TOA) reflected solar electromagnetic energy (shortwave bands) and the ground plus atmosphere thermal emission (longwave band). Radiance and exitance are quantized into unsigned 8-bit numerical value, known as Digital Numbers (DN), thus ranging between 0 and 255. The Digital

Number is assigned to a square pixel (originally 30 and 120 m for shortwave and longwave bands, respectively) via a resampling algorithm (cubic convolution). Hence, this DN, in each pixel, represents optical characteristics for given shortwave spectral bands (Bands 1-5 and 7) and thermal characteristics for the longwave band (Band 6).

Pre-processing remotely sensed images includes spectral reflectance calibration and shortwave atmospheric correction and thermal band calibration and longwave atmospheric correction. This process is critical because the accuracy of physical indicators used in SEB models, such as the albedo, vegetation indices, emissivity and land surface temperature depend on this calibration.

4.1.1 Optical images calibration and processing

Spectral radiometric calibration allows determining, from the quantified numeric DN provided by the satellite sensors, a physical variable representing the radiative properties of observed pixels.

4.1.1.1 Spectral Radiance and Top-of-Atmosphere Reflectance

To convert DN value into TOA reflectance, firstly, the DN obtained for the multispectral data acquired by Bands 1-5 and 7 has to be converted into spectral radiance.

The spectral radiance for each band represents the outgoing radiation energy of the band observed at TOA and is computed using the gain and bias values specific of each scene.

$$L_\lambda = (Gain \times DN) + Bias \quad (4.1)$$

where L_λ is the pixel value of Spectral radiance at the sensor's aperture, the *Gain* and *Bias* are specific values for each band, which are included in the header file provided with the image metadata.

The second step is to convert the L_λ data into top-of-atmosphere reflectance (R_{TOA}) by using the rescaling coefficients provided in the image metadata file. The reflectivity for each band at the top of atmosphere (ρ_{TOA}), which corresponds to the ratio of the surface reflected radiation flux to the incident radiation flux, is computed as follows:

$$\rho_{TOA} = \frac{\pi.L_\lambda}{ESUN_\lambda.\cos\theta.d_r} \quad (4.2)$$

where π is ≈ 3.14159, $ESUN_\lambda$ ($Wsr^{-1}\mu m^{-1}m^{-2}$) is the mean solar exo-atmospheric solar irradiance for each band, θ is the solar incidence angle (from nadir), and d_r (-) is the inverse squared relative earth-sun distance.

Here, the term d_r is defined as $1/d_{e\text{-}s}^2$, in which $d_{e\text{-}s}$ represents the relative earth-sun distance in astronomical units (-). The term d_r can be calculated as a function of the sequential day of the year (Julian date) (*DOY*) using the equation provided in the FAO-56 paper (Allen et al., 1998):

$$d_r = 1 + 0.033\cos\left(DOY\frac{2\pi}{365}\right) \quad (4.3)$$

4.1.1.2 Surface Reflectance

To derive reliable values of reflectance at the earth surface, atmospheric correction has to be applied. The R_{TOA} is the reflectance measured by a space-based sensor flying higher than the earth's atmosphere and the band calculated reflectivity values will include contributions from thin clouds and atmospheric aerosols and gases. The corrections for atmospheric interference are based on the state of the atmosphere itself. Atmospheric correction models allow removing the effects of atmospheric scattering and absorption. The Second Simulation of a Satellite Signal in the Solar Spectrum code (6S code) was used for atmospheric correction (Vermote et al., 1997). The Surface Reflectance is calculated by equation 4.4 taking into consideration the *6S* code as follows:

$$\rho_{ground} = \frac{\rho_{TOA} - \rho_{atm}}{s\times\rho_{toa} - s\times\rho_{atm} + T_{gas}\times T_{s\uparrow}\times T_{s\downarrow}} \quad (4.4)$$

where ρ_{TOA} refers to the top of the atmosphere reflectance, ρ_{atm} is the intrinsic atmospheric reflectance, *s* is the spherical atmospheric albedo and takes into account the energy reflected from the target and that is trapped by the back-scattering illuminating the target, T_{gas} refers to the transmittance of the gas in the atmosphere and finally, $T_{s\uparrow}$ and $T_{s\downarrow}$ are atmospheric transmittance related to atmospheric path in descent and ascent direction, respectively (Vermote et al., 1997; Kotchenova et al., 2006, 2007 and 2008).

4.2 Surface Albedo

Surface shortwave albedo (α) is determined through a linear combination of the reflective bands by integrating reflectivity (ρ_λ) from shortwave bands (1-5 and 7) of Landsat TM, after applying an atmospheric correction by multiplying with weighting coefficients (ω_λ) (Tasumi et al., 2007; Starks et al., 1991). The weighting coefficients are estimated by calculating the ratio between the incident irradiance for each band and the sum of the irradiance of all the bands. Then, α is computed as follows:

$$\alpha = \sum(\omega_\lambda \times \rho_\lambda) \tag{4.5}$$

4.3 Vegetation indices

4.3.1 Normalized Difference Vegetation Index (NDVI)

The time series of spectral surface reflectance have been used to generate the NDVI profiles in each pixel of the area. NDVI is expressed as the difference in reflectance between the near-infrared ($\rho 4$) and red ($\rho 3$) bands, normalized with respect to their sum, as shown in equation 4.6:

$$NDVI = \frac{(\rho_4 - \rho_3)}{(\rho_4 + \rho_3)} \tag{4.6}$$

4.3.2 Leaf Area Index (LAI):

LAI can be estimated indirectly through a remote sensing vegetation index (VI):

$$\text{LAI} = -\frac{1}{k} ln\left(\frac{\text{VI} - \text{VI}_\infty}{\text{VI}_0 - \text{VI}_\infty}\right) \tag{4.7a}$$

where VI_0 is the value of VI for null LAI, VI_∞ is the value of VI for LAI tending to-infinitive, k is a combination between an extinction factor and diffusion of the radiation within the canopy.

Here an approach similar to that proposed by the CLAIR semi-empiric model (Clevers, 1989) by employing the weighted difference vegetation

index (WDVI) was used. According to Cammalleri (Ph.D. thesis), within this research, we used the NDVI to retrieve *LAI* maps (eq. 4.7).

$$\text{LAI} = -\frac{1}{0.75} ln\left(1 - \frac{\text{NDVI}}{0.95}\right) \quad (4.7b)$$

where the coefficients 0.75 and 0.95 were locally calibrated over the study area.

4.3.3 Vegetation Fractional Cover (f_c)

The vegetative fraction coverage maps were generated by using the following formulation proposed by Choudhury et al. (1994):

$$f_c = 1 - \left(\frac{\text{NDVI}_{\max} - \text{NDVI}}{\text{NDVI}_{\max} - \text{NDVI}_{\min}}\right)^{0.9} \quad (4.8)$$

where $\text{NDVI}_{\min}$ represents an entirely bare surface, whereas $\text{NDVI}_{\max}$ represents a fully covered surface.

4.4 Land surface emissivity

The broad-band surface thermal emissivity (ε_o) is dimensionless. Emissivity retrieval here does not take into account differences within a particular pixel that can occur due to the presence of different components inside the considered pixel and particularly the percentage of vegetative cover and bare soil. For NDVI values higher than 0.3, Land surface emissivity was retrieved from NDVI based on the following logarithmic relationship (Van de Griend and Owe, 1993):

$$\varepsilon_o = 1.009 + 0.047 \times ln(\text{NDVI}) \quad (4.9)$$

whereas, it was assumed equal to 0.96 for 0 < NDVI < 0.3 and equal to 0.98 for NDVI < 0 (Bastiaanssen et al., 1998).

4.5 Surface radiometric temperature and thermal atmospheric correction

Equation 4.1 was used to convert DN into the at-sensor top of atmosphere radiance (L_{TOA}). In order to remove the atmospheric

correction for the thermal band, as addressed by Barsi et al. (2003) the scene based atmospheric correction parameters (τ, L_u and L_d) were obtained from a Web-Based Tool (Atmospheric Correction Parameter Calculator) http://atmcorr.gsfc.nasa.gov. The atmospheric correction was applied to convert the top of atmosphere radiance to a surface-leaving radiance of a blackbody target at a kinetic temperature T (L_T) as follows:

$$L_T = \frac{L_{TOA} - L_u - \tau(1-\varepsilon_o)L_d}{\tau * \varepsilon_o} \quad (4.10)$$

where τ is the band average atmospheric transmission, ε_o is the emissivity of the surface, L_u is the effective upwelling or atmospheric path radiance, L_d is the effective down welling or sky radiance.

The surface brightness temperature (T_b) can be derived from L_T by using a relationship similar to the Planck formula in which two thermal constants (K_1 and K_2) are provided in the metadata file of Landsat images (Markham and Barker, 1986):

$$T_b = \frac{K_2}{ln\left(\frac{K_1}{L_T}+1\right)} \quad (4.11)$$

The surface radiometric temperature (T_{rad}) is one of the key parameters in the surface energy balance physics. T_{rad} is calculated from T_b and ε_0. The surface emissivity is taken into account to differentiate between the considered surface and theoretical black body. The surface radiometric temperature was obtained as follows:

$$T_{rad} = \frac{T_b}{\varepsilon_0^{0.25}} \quad (4.12)$$

4.6 Roughness parameters

The roughness parameters are important indicators in the retrieval of H. The zero plane displacement (d_0), and momentum roughness length (z_{0m}) parameters depend on the roughness and geometry of the considered surface. For a bare soil, d_0 is assumed equal to zero since the effects of roughness occur directly on the soil surface and the roughness is assumed constant and equal to z_{0m} = 0.01 m, representing the soil surface

roughness. For a uniform vegetated surface, the following widely used formulation, suggested by Brutsaert (1985), uses the canopy height to assess d_0 and z_{0m} as following:

$$d_0 = \frac{2}{3} h_c \tag{4.13}$$

$$z_{0m} = \frac{1}{8} h_c \tag{4.14}$$

where, h_c is the canopy height retrieved as ground-truth data.

The pixels values of roughness length for heat transport are computed from z_{0m} as follows:

$$z_{0h} = 0.1\, z_{0m} \tag{4.15}$$

4.7 The Single Source Surface Energy Balance (SEBAL) model

In SEBAL, instantaneous net radiation (R_n) and soil heat flux (G_0) are estimated from remote sensing data and some ancillary climatic variables. The instantaneous sensible heat flux (H) estimation requires the evaluation of near-surface temperature gradient (ΔT) and instantaneous latent heat flux (λET), which is computed as a residue of the energy budget.

4.7.1 Instantaneous net surface radiation flux (SEBAL)

Instantaneous net surface radiation flux (R_n) [W.m^{-2}] representing the radiative budget at land surface, is the sum of shortwave (R_S) and long-wave radiation components R_L. R_n can be estimated from remote sensing data and some climatic variables, as incoming minus outgoing radiation fluxes:

$$R_n = (1 - \alpha) R_{S\downarrow} + R_{L\downarrow} - R_{L\uparrow} - (1 - \varepsilon o) R_{L\downarrow} \tag{4.16}$$

where $R_{S\downarrow}$ (W m^{-2}) is incoming short-wave radiation, a is surface albedo, $R_{L\downarrow}$ (Wm^{-2}) is the incoming long-wave radiation, $R_{L\uparrow}$ (W m^{-2}) is the outgoing long-wave radiation. The term (1-ε_o)$R_{L\downarrow}$ represents the fraction

of incoming long-wave radiation reflected from the surface. Figure 4.1 schematizes the flowchart used to evaluate R_n.

4.7.1.1 Incoming extraterrestrial shortwave radiation

Incoming shortwave radiation ($R_{S\downarrow}$) (W m^{-2}), similarly to the direct and diffuse clear-sky solar radiation flux that reaches the earth's surface, was obtained as:

$$R_{s\downarrow} = K_{TOA} \times cos\,\theta \times d_r \times \tau_{sw} \quad (4.17)$$

where τ_{sw} is the broadband short-wave atmospheric transmissivity, K_{TOA} is the solar constant (1367 W m^{-2}) (Allen et al., 1998), θ is the solar beam incidence, and d_r is the inverse of the squared relative earth-sun distance in astronomical units.

The atmospheric transmissivity (τ_{sw}) varies with altitude and is calculated for cloud-free conditions, by using the methodology proposed by Allen et al. (1998). The proposed procedure assumes that τ_{sw} reaches its maximum value of 0.75 at sea level and then linearly decreases with elevation z [m a.s.l.]:

$$\tau_{sw} = 0.75 + 2 \times 10^{-5} \times z \quad (4.18)$$

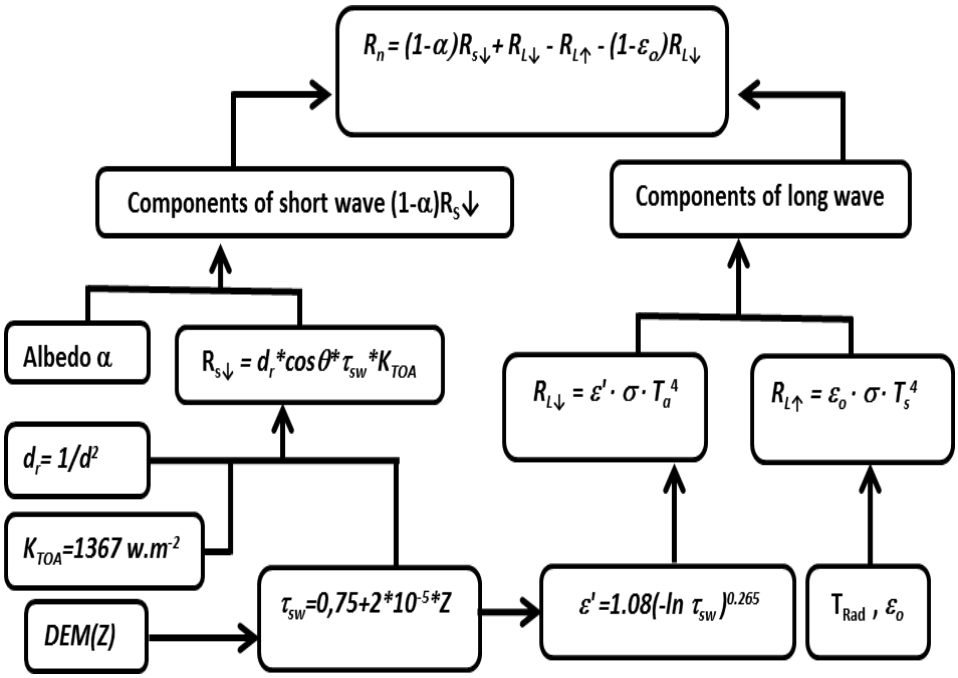

Figure 4.1: Net radiation calculation flow chart.

The solar beam incidence angle was computed by the following equation (Garner and Ohmura, 1968):

$$\cos(\theta s) = \sin(\delta)\sin(\varphi)\cos(s) - \sin(\delta)\cos(\varphi)\sin(s)\cos(\xi) + \cos(\delta)\cos(\varphi)\cos(s)\cos(\omega) + \cos(\delta)\sin(\varphi)\sin(s)\cos(\xi)\cos(\omega) + \cos(\delta)\sin(\xi)\sin(s)\sin(\omega) \quad (4.19)$$

where, δ [rad] is the solar declination, φ [rad] is the latitude, s [rad] is the surface slope, and ξ [rad] is the surface aspect angle.

4.7.1.2 Longwave radiation

Longwave radiation (R_L) originating from the incident solar electromagnetic radiation that is absorbed by the atmosphere or land surface is a critical component of R_n energy budget. R_L is formed by two components, the incoming and the outgoing longwave radiations.

Incoming longwave radiation ($R_{L\downarrow}$) represents the atmospheric downward originated thermal radiation (Wm^{-2}). According to Stefan-Boltzmann

law, $R_{L\downarrow}$ is in function of the near-surface air temperature and the atmospheric emissivity and is computed as:

$$R_{L\downarrow} = \varepsilon_a \times \sigma \times T_a^4 \quad (4.20)$$

where, ε_a (dimensionless) is the atmospheric emissivity in the thermal infrared, σ is the Stefan-Boltzmann constant equal to 5.67 × 10-8 W m^{-2} K^{-4}, and T_a (°K) is the near-surface air temperature.

The atmospheric emissivity in the thermal infrared can be obtained by following the empirical equation given by Bastiaanssen (1995):

$$\varepsilon_a = 0.85 \times (-ln\,\tau_{SW})^{0.09} \quad (4.21)$$

The outgoing longwave radiation ($R_{L\uparrow}$) (W m^{-2}) represents the upwelling thermal radiation emitted to the atmosphere from the land surface. It was obtained by using the surface radiometric temperature (T_{rad}), as shown in equation 4.22:

$$R_{L\uparrow} = \varepsilon_o T_{rad}^4 \quad (4.22)$$

4.7.2 Soil Heat Flux (SEBAL)

Soil heat flux at ground level (G_0) (W m^{-2}) is the rate of heat storage into the soil due to conduction. Here since soil temperature at different depths is not known, G_0 is assumed as a fraction of the total net radiation. Liang (2004b) showed that G_0 can range between 5% of the total net radiation in case of full canopy cover and 50% of the total net radiation for dry bare soils. In SEBAL, in which there is no need to distinguish between soil and canopy radiation, near midday values of G_0 were estimated with sufficient reliability based on NDVI and surface albedo, by using the following empirical relationship developed by Bastiaanssen (2000):

$$G_0 = \frac{T_{rad}}{\alpha}(0.0038\alpha + 0.007\alpha^2)(1 - 0.98NDVI^4)R_n \quad (4.23)$$

4.7.3 Sensible heat flux (SEBAL)

In SEBAL model, based on the assumption that ΔT varies linearly with radiometric temperature (T_{rad}), the sensible heat flux is estimated as follows (Bastiaanssen et al., 1998 and 2005):

$$H = \frac{(\rho \times C_p \times \Delta T)}{r_{ah}} \quad (4.24)$$

where ρ is air density (kg m^{-3}), c_p (1004 $J\ kg^{-1}K^{-1}$) is the specific heat of air, ΔT (°K) is the temperature gradient ($T_{z1} - T_{z2}$) between two heights z_1 and z_2, and r_{ah} ($s\ m^{-1}$) is the aerodynamic resistance to heat transport.

The temperature gradient ΔT represents the difference in temperature between a reference and the roughness heights governing the transfer of heat. The reference heights z_1 and z_2 in meters are defined as the vertical heights, representing limits above the vegetation zero plane displacement (d_0); z_1 represents the mean height above the vegetation where the radiant energy is converted into sensible heat and z_2 is the height just below the boundary layer. The values of z_1 and z_2 are assumed respectively equal to 0.01 and 2.0 m above the ground level.

To compute H, two unknown variables need to be retrieved, ΔT and the aerodynamic resistance to heat transport, r_{ah} that, for neutral stability, can be computed as:

$$r_{ah} = \frac{ln\left(\frac{z_2}{z_1}\right)}{u^* \times K} \quad (4.25)$$

where u^* ($m\ s^{-1}$) is the friction velocity, and κ=0.41 is the von Karman's constant.

Friction velocity (u^*), which quantifies the turbulent velocity fluctuations in the air, is used to obtain the aerodynamic resistance to heat transport (r_{ah}). The calculation of u^* requires the knowledge of wind speed, u^*, that is computed for neutral atmospheric conditions at the weather station, where the height of the measurement (z_u) is known, and the wind speed (u_x) is measured (Brutsaert, 1985). The friction velocity (u^*) at the weather station is computed by using the logarithmic wind law for neutral atmospheric conditions:

$$u^* = \frac{Ku_x}{ln\left(\frac{z_u}{z_{om}}\right)} \tag{4.26}$$

where, z_{om} is the momentum roughness length parameter.

In SEBAL, under the assumption that the wind speed at blending height is aerially constant, u^* corresponding to each pixel is determined. This blending height is assumed at 200 m, and the wind speed at this height (u_{200}) is hypnotized that there is no effect from the surface roughness. Wind speed at the blending height above the weather station is calculated as follows:

$$u_{200} = u^* \frac{ln\left(\frac{200}{z_{om}}\right)}{K} \tag{4.27}$$

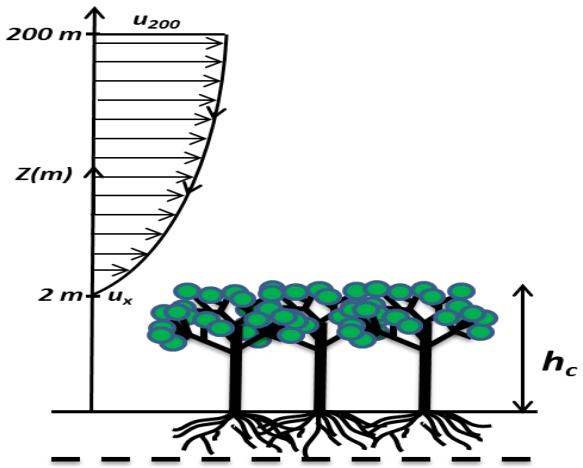

Figure 4.2: Determination of friction velocity (u*), and wind speed at the blending height (200 m).

The spatial distribution of friction velocity (u^*) is then calculated by using the following equation:

$$u^* = \frac{ku_{200}}{ln\frac{200}{z_{om}}} \tag{4.28}$$

Once known u^*, it is possible to evaluate (eq. 4.25) the aerodynamic resistance to heat transport (r_{ah}) for each pixel of the selected scene. After

the retrieval of the spatial distribution of r_{ah} and since the air temperature at each pixel is unknown, along with the explicit values for T_{z1} and T_{z2}, the near-surface temperature difference (ΔT) is used to compute the sensible heat flux (H). To facilitate the computation of the spatial distribution of ΔT, SEBAL uses firstly the two "anchor" pixels approach, where reliable values for H can be predicted and thus ΔT can be estimated.

The two anchor pixels represent two hydrological extremes located in the area of interest, the hot and cold pixels. The first extreme is the "cold" pixels representing a wet, irrigated full ground cover vegetation. The surface temperature at the cold pixel T_{cold} and near-surface air temperature T_a are assumed to be similar ($T_a \cong T_{cold}$) and the soil heat flux can be assumed negligible. At the "cold" pixel, the sensible heat flux is calculated as:

$$H_{cold} = R_{ncold} - \lambda ET_{cold} \quad (4.29)$$

By solving the energy balance equation in the cold pixel, it is possible to compute ΔT_{cold} by using equation 4.30:

$$\Delta T_{cold} = \frac{H_{cold} \times r_{ah}}{\rho \times c_p} \quad (4.30)$$

The "hot" pixel, as the second hydrological extreme, is selected as a dry surface layer (e.g., bare agricultural soil). In the hot pixel, the latent heat flux of the energy balance (λET_{hot}) is considered negligible. The energy balance is assigned as:

$$H_{hot} = R_{nhot} - G_{0hot} \quad (4.31)$$

By solving the energy balance equation in the hot pixel, it is possible to determinate ΔT_{hot} as follows:

$$\Delta T_{hot} = \frac{H_{hot} \times r_{ah}}{\rho \times c_p} \quad (4.32)$$

One of the main assumptions of SEBAL model is the linearity between ΔT and T_{rad}. The selection of the anchor pixels allowed solving the linear

equation and fix boundaries for ΔT variations with respect to T_{rad}. Under this assumption, SEBAL computes ΔT in each pixel as follows:

$$\Delta T = aT_{rad} + b \tag{4.33}$$

where a and b are the linear equation correlation coefficients.

After retrieving ΔT, SEBAL model gives a first estimation of the sensible heat flux (H) in all the scene pixels by using equation 4.24. The first estimation of H is computed under the hypothesis of neutral stability, where temperature and wind distributions follow almost adiabatic conditions. Atmospheric stability can have a significant effect on the retrieval of aerodynamic resistance (r_{ah}) and must be taken into account in the computation of sensible heat flux (H), especially under dry conditions. It is important to consider that actual conditions can be unstable and thus can modify the friction velocity and the aerodynamic resistance to heat transport.

Physical corrections of atmospheric stability are crucial to obtain reliable turbulent fluxes such as the latent and sensible heat fluxes. In order to account for the buoyancy effects generated by surface heating, SEBAL applies corrections based on the Monin-Obukhov similarity theory (Paulson 1970; Webb 1970).

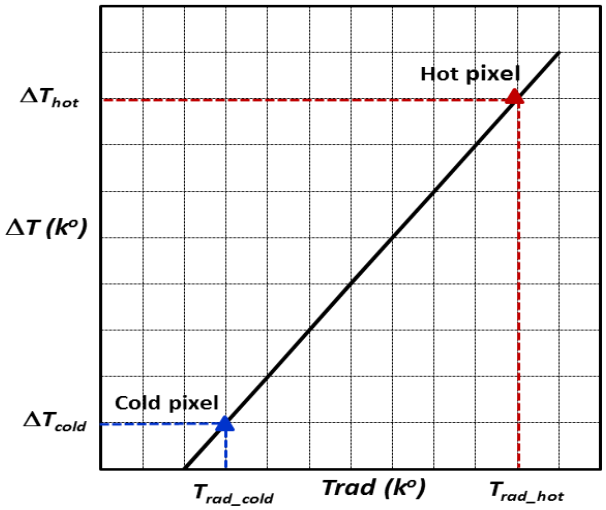

Figure 4.3: Linear variation of ΔT with radiometric temperature T_{rad} .

The Obukhov length (L) is used to define the atmospheric stability conditions, thus account for nonadiabatic conditions. The first value of H initially estimated is used in the following iteration to obtain the integrated stability correction based on the Monin–Obukhov similarity hypothesis, that allows improving u^* estimation. The new value of u^* is then used to estimate a new r_{ah} that introduces the heat transport stability correction. SEBAL repeats iteratively the computation of H until the values $\Delta T_{hot,}$ and r_{ah} at the "hot" pixel stabilize and as a result, H represents the pixel-to-pixel local buoyancy conditions.

The Obukhov length (L) is the height at which forces of buoyancy or stability and mechanical mixing are equal; it is a function of the heat and momentum fluxes and is computed as follows (Paulson 1970; Webb 1970):

$$L = \frac{\rho c_p u^{*3} T_{rad}}{KgH} \tag{4.34}$$

where g is the gravitational constant (9.81 m s^{-2}).

If L is negative ($L < 0$), the atmospheric conditions are considered unstable, and the temperature gradient is different from the adiabatic condition; if L is equal to zero, the atmosphere is considered neutral, whereas if L is positive ($L > 0$), the atmosphere is considered stable.

Depending on the atmospheric conditions (unstable, neutral or stable), the values of the stability corrections for momentum and heat transport (ψ_m and ψ_h) are computed by using the formulations provided by Paulson (1970) and Webb (1970).

In neutral conditions (L=0), ψ_m and ψ_h are equal to zero, and the primary estimation of H is accepted. In unstable conditions (L<0) the stability correction for momentum transport at the blending height (here assumed z_u=200 m) is given by:

$$\psi_m = 2\,ln\left(\frac{1+\mu_m}{2}\right) + ln\left(\frac{1+\mu_m^2}{2}\right) - 2arctan(\mu_m) + \frac{1}{2}\pi \tag{4.35}$$

The parameter μ_m is evaluated as:

$$\mu_m = \left[1 - 16\frac{(z_u - d_0)}{L}\right]^{1/4} \quad (4.36)$$

The stability corrections for heat transport at the two reference heights z_T (here assumed 0.1 and 2 m) are determined as:

$$\psi_{h(2m)} = 2\,ln\left(\frac{1+\mu_h^2}{2}\right) \quad (4.37)$$

The parameter $\mu_{h(2m)}$ is given as:

$$\mu_{h(2m)} = \left[1 - 16\frac{(z_T - d_0)}{L}\right]^{1/4} \quad (4.38)$$

and

$$\psi_{h(0.1m)} = 2\,ln\left(\frac{1+\mu_h^2}{2}\right) \quad (4.39)$$

The parameter $\mu_{h(0.1m)}$ is given as:

$$\mu_{h(0.1m)} = \left[1 - 16\frac{(z_T - d_0)}{L}\right]^{1/4} \quad (4.40)$$

Under stable conditions ($L > 0$) the stability correction for momentum transport at the blending height and for the heat transport at the two reference heights z_1 and z_2 are respectively given by:

$$\psi_{m200} = -5\left(\frac{2}{L}\right) \quad (4.41)$$

$$\psi_{h2} = -5\left(\frac{2}{L}\right) \quad (4.42)$$

$$\psi_{h0.1} = -5\left(\frac{0.1}{L}\right) \quad (4.43)$$

Depending on the atmospheric conditions, the values of the momentum stability corrections (ψ_m) and heat transport stability corrections (ψ_h) are

computed by using the formulations given by Paulson (1970) and Webb (1970). A corrected new value for the friction velocity (u^*) and the aerodynamic resistance to heat transport (r_{ah}) is computed in an iterative process based on the following equations:

$$u^* = \frac{u_{200} K}{ln\frac{200}{z_{om}} - \psi_{h200}} \tag{4.44}$$

$$r_{ah} = \frac{ln\left(\frac{z_2}{z_1}\right) - \psi_{h(z_2)} + \psi_{h(z_1)}}{u^* \times K} \tag{4.45}$$

New ΔT values for the "cold" and "hot" pixel are recalculated by equations 4.30 and 4.32, based on the corrected r_{ah}. A new solution for the linear relation between T_{rad} and ΔT defined in the equation 4.33 is found (new coefficient a, b) and a new value of ΔT is obtained. Finally, using equation 4.24, H is recalculated spatially, pixel by pixel for the entire scene. The previous steps are repeated for a revised value for ΔT, a new corrected value for H and a new stability correction. This iterative process is repeated until successive values of H stabilizes, and thus the final value for the sensible heat flux (H) is obtained. Figure 4.4 schematizes, with a flow chart, the SEBAL iterative methodology in retrieving the sensible heat flux (H).

4.7.4 Instantaneous latent heat flux (SEBAL)

The fluxes Rn and G_0 and the corrected final value of the sensible heat flux (H) represent instantaneous retrievals of the surface energy fluxes (image acquisition time). The energy allocated for the evapotranspiration process at the instant of the satellite, known as the instantaneous latent heat flux (λET), is then estimated as a residual of the surface energy balance:

$$\lambda ET = R_n - G_0 - H \tag{4.46}$$

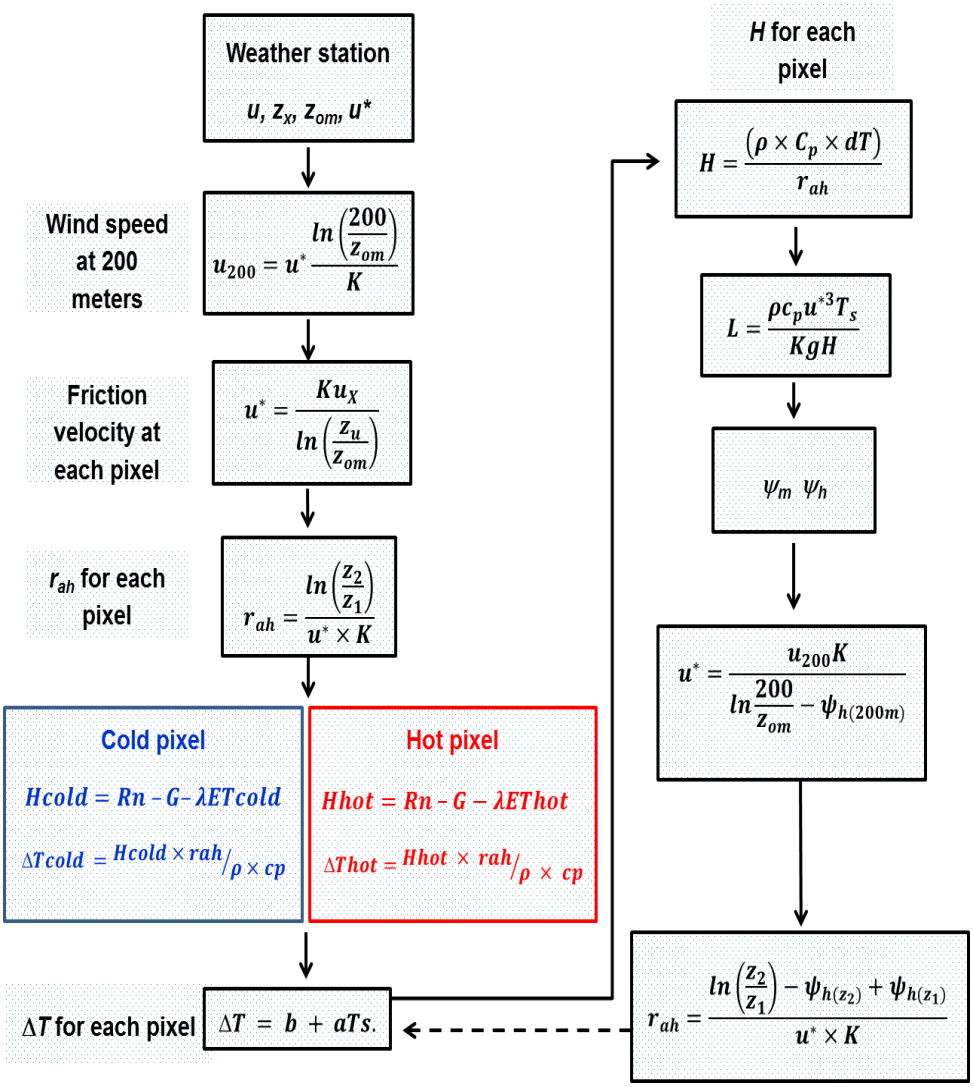

Figure 4.4: Schematic representation of SEBAL sensible heat flux (*H*) retrieval.

4.8 The Two-Source Energy Balance (TSEB) model

4.8.1 Air temperature thermal correction (TSEB internal calibration)

The TSEB internal calibration approach, as proposed by Norman *et al.* (2006), is used to derive estimations of air temperature in the image scene. Similarly to SEBAL, the internal-scene calibrated TSEB assumes the presence of a cold pixel (a non-stressed, irrigated and full covered vegetation) in the studied scene. Air temperature in the cold pixel is assumed to be equal to the remotely sensed radiometric temperature, and the soil heat flux at the cold pixel is considered negligible due to the absence of soil layer. The calibrated air temperature (T_a) can be estimated using the following relationship:

$$T_a = T_{rad\_cold} - \frac{r_{ah}}{\rho c_p}[R_n - \lambda ET_{PT}] \quad (4.47)$$

where, T_{rad_cold} is the radiometric temperature at the cold pixel, r_{ah} is the aerodynamic resistance, R_n is the net radiation, and λET_{PT} is the Priestley-Taylor latent heat flux over the cold pixel.

The Priestley-Taylor latent heat flux can be obtained as (Priestley and Taylor, 1972):

$$\lambda ET_{PT} = \left(a_{PT}.\frac{\Delta}{\Delta+\gamma}\right).R_n \quad (4.48)$$

where a_{PT} is the Priestley-Taylor coefficient, equal to 1.26 for potential conditions, Δ is the slope of the saturation vapor pressure versus temperature curve and γ is the air psychrometric constant(0.066kPa.°C^{-1}).

The Obukhov length (L) is used to define the stability conditions of the atmosphere with an iterative process and give an improved estimation of the friction velocity (u*) used to estimate the new value of the aerodynamic resistance (r_{ah}), which introduces the heat transport stability correction. In this thesis, ten iterations were carried out to improve r_{ah} and u*, whereas four iterations were done to compute calibrated air temperature.

The schematic representation of the TSEB internal calibration for air temperature is presented in figure 4.5.

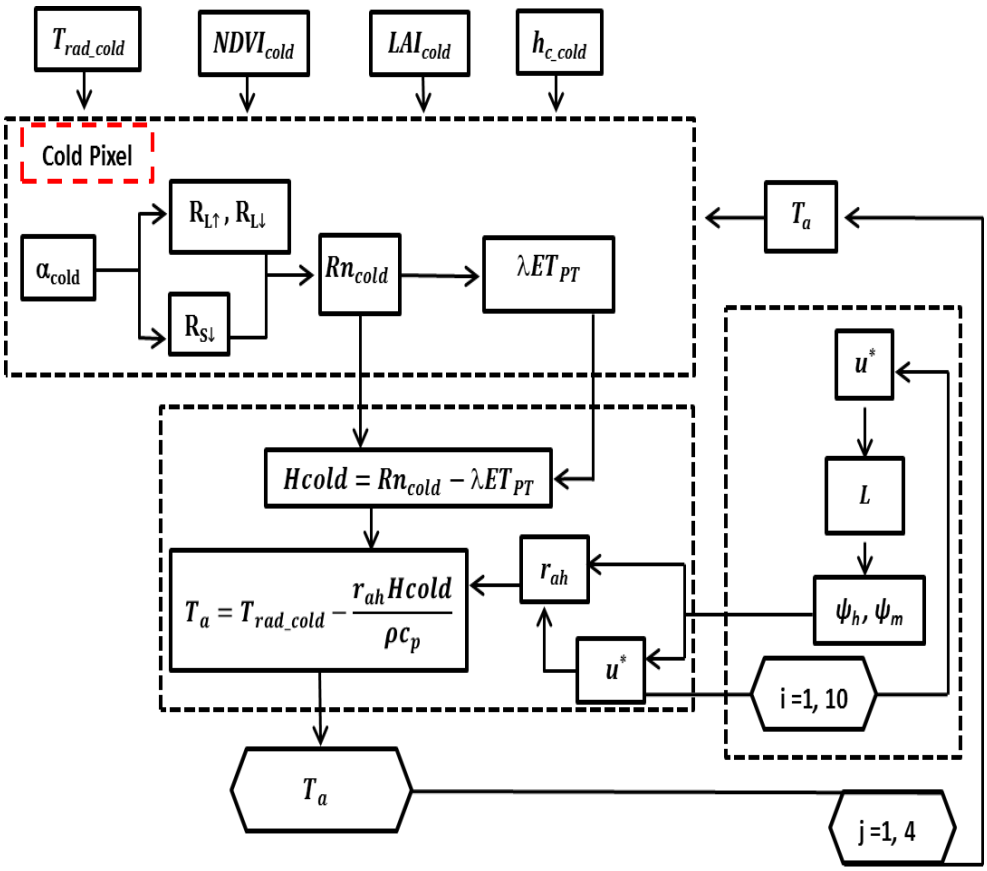

Figure 4.5: Schematic representation of TSEB air temperature internal calibration.

4.8.2 TSEB Soil-canopy radiation partitioning

By following a similar approach used on SEBAL, net radiation (R_n) was estimated by the two source model TSEB from remote sensing data and some ancillary meteorological data; R_n, as the balance between the incoming and the outgoing radiation fluxes, is computed by Eq. 4.16.

In TSEB, R_n is partitioned between canopy and soil. This partitioning is crucial to differentiate soil evaporation and canopy transpiration. Net radiation is assessed for canopy and soil as following indicated (Anderson et al., 1997):

$$R_{ns} = R_n exp(-\kappa LAI) \quad (4.49)$$

$$R_{nc} = R_n[1 - exp(-\kappa LAI)] \quad (4.50)$$

where, κ is the extinction coefficient used to calculate the surface net radiation of soil (R_{ns}), that was assumed equal to 0.45 (Norman *et al.*, 1995; Ross, 2012).

4.8.3 Soil Heat Flux (TSEB)

In the original TSEB formulation, where the distinction between canopy and soil is essential, G_0 can be approximated from the soil net radiation (Norman et al., 1995):

$$G_0 = c_g R_{ns} \quad (4.51)$$

where, c_g (0.2) *is a* coefficient ranging between 0.2 and 0.5 (Choudhury et al., 1987).

4.8.4 The Partitioned Sensible and Latent Heat Fluxes (TSEB)

In the two source model (TSEB), the land surface is treated differently, where the radiative exchanges (net radiation), the thermal heat conduction and convection between the surface and low atmosphere are parameterized and partitioned between vegetation and soil.

The key element of the two source energy balance model is the partitioning of fluxes between soil and canopy. Partitioning of net radiation represents the first step in estimating the various components of

temperature included in TSEB calculations. The knowledge of soil and canopy temperatures allows distributing available energy (R_n-G_0) to the remaining components of surface energy balance. The TSEB key boundary condition is the radiometric land surface temperature (Kustas and Anderson, 2009). The contributions of canopy and soil to land surface radiometric temperature is different. Indeed, the model assumes that a single pixel emissivity can represent the pixel components (soil and vegetation) and the radiometric temperature is partitioned on the basis of the fractional cover as follows:

$$T_{rad} = [f_c T_c^4 - (1 - f_c) T_s^4]^{1/4} \quad (4.52)$$

where T_s is the soil surface temperature (°K), T_c is the canopy temperature (K), and f_c is the fractional vegetation cover.

The primary hypothesis in TSEB is the assumption of a potential evapotranspiration rate. TSEB estimates the Priestley-Taylor canopy latent heat flux (λETc_{PT}) according to eq. 4.48:

$$\lambda ET_{C_{PT}} = \left(a_{PT}.f_g.\frac{\Delta}{\Delta+\gamma}\right).R_{nc} \quad (4.53)$$

where a_{PT} is the Priestley-Taylor coefficient (1.26 for potential conditions), f_g is the green fraction of LAI (assumed equal to 1), R_{nc} is the net radiation flux at canopy surface obtained by Eq.4.5, Δ is the slope of the saturation vapor pressure versus temperature curve and γ is the psychrometric constant (0.066 kPaC^{-1}).

The retrieval of λETc_{PT} allows solving the surface energy balance equation since the soil heat flux under the canopy is considered negligible, and the sensible heat flux in canopy layer (H_c) is obtained by subtracting the latent heat fluxes from the net radiation in the canopy layer as:

$$H_c = R_{nc} - \lambda ET_{C_{PT}} \quad (4.54)$$

Once calculated the sensible heat flux in the canopy layer, it is possible to obtain a reasonable estimation of canopy layer temperature (Tc) and thus retrieve the various components of the temperature, but first, the

components of the resistance network have to be computed. The aerodynamic resistance r_a (s m^{-1}), corresponding to r_{ah} computed in SEBAL, is evaluated as:

$$r_a = \frac{ln\left(\frac{z_T - d_0}{z_{0h}}\right)}{u^* \times \kappa} \quad (4.55)$$

where z_T represents the height of air temperature measurement, d_0 is the zero plane displacement length z_{0h} is the heat transport roughness length, u^* is the friction velocity (m s^{-1}) and κ=0.41is von Karman's constant.

The friction velocity (u^*), is obtained by equation 4.56 using the horizontal wind speed measurement at a known elevation (z_u) and u_{200} is obtained by the same procedure indicated in the previous section (Eq. 4.27).

$$u^* = \frac{u_{200}\kappa}{ln\left(\frac{z_u - d_0}{z_{0m}}\right)} \quad (4.56)$$

where z_{om} is momentum roughness length.

The resistance to the sensible heat in the boundary layer just above the soil surface (the soil-canopy air space layer) is defined as r_s (s m^{-1}) and is computed by using the simplified semi-empirical equation given by Sauer et al. (1995):

$$r_s = \frac{1}{a' + b' u_s} \quad (4.57)$$

where, *a'* and *b'* are soil resistance parameters equal to 0.004 and 0.012 respectively (Sauer et al., 1995), u_s is the wind speed (m s^{-1}) just above the soil surface, computed as proposed by Goudriaan (1977), from wind speed at the top of the canopy layer (u_c):

$$u_s = u_c exp\left[-a\left(1 - \frac{0.2}{h_c}\right)\right] \quad (4.58)$$

The factor *a* is the extinction factor for the exponential wind profile, computed as a function of canopy parameters as the canopy height (h_c), the leaf size (*s*) and LAI:

$$a = 0.28LAI^{2/3}{h_c}^{1/3}s^{-1/3} \tag{4.59}$$

The wind speed at the canopy surface u_c) can be obtained as:

$$u_c = u_x\left[\frac{ln\left(\frac{h_c-d_0}{z_{0m}}\right)}{ln\left(\frac{z_u-d_0}{z_{0m}}\right)}\right] \tag{4.60}$$

where, u_x, as defined before, is the wind speed above the canopy at measurement height z_u.

The 3rd resistance parameter is the resistance of the boundary layer of canopy leaves (r_c) ($s\ m^{-1}$), that can be approximated as follows:

$$r_c = \frac{C'}{LAI}\left(\frac{\omega_l}{u_{d_0+z_{0m}}}\right)^{1/2} \tag{4.61}$$

where, the coefficient C' is set equal to 90 m s^{-1} (Grace, 1981) and u_{d0+z0m} is the wind speed at the height (d_0+z_{0m}), indicating the boundary layer of canopy:

$$u_{d_0+z_{0m}} = \mathrm{u}_c\exp\left[-a\left(1-\frac{d_0+z_{0m}}{h_c}\right)\right] \tag{4.62}$$

The numerical solution aimed to assess T_c and T_s can be applied based on the linearization of Eq. 4.52. After obtaining the resistances r_a, r_s and r_c, under the initial hypothesis of potential evapotranspiration, the canopy temperature (T_c), the soil temperature (T_s) and air temperature in the vegetation-air layer (T_{ac}) are calculated. The canopy temperature (°K) is initially approximated based on H_c estimates by the following equation:

$$T_{c,lin} = \frac{\frac{T_a}{r_a}+\frac{T_{rad}}{r_s(1-f_c)}+\frac{Hcr_x}{\rho cp}\left(\frac{1}{r_a}+\frac{1}{r_s}+\frac{1}{r_x}\right)}{\frac{1}{r_a}+\frac{1}{r_s}+\frac{f_c}{r_s(1-f_c)}} \tag{4.63}$$

By assuming:

$$\left(T_{c,lin}+\Delta T_c\right)^4 = T_{c,lin}^4 + 4T_{c,lin}^3\Delta T_c \tag{4.64}$$

that is realistic when $T_{c,lin}$ >>ΔT, with ΔT (°*K*) defined as follows:

$$\Delta T_c = \frac{T_{rad}^4 - f_c T_{c,lin}^4 - (1-f_c) T_d^4}{4(1-f_c) T_D^3 \left(1+\frac{r_s}{r_a}\right) + 4 f_c T_{c,lin}^3} \quad (4.65)$$

$$T_D = T_{c,lin}\left(1+\frac{r_s}{r_a}\right) - \frac{Hc_1 r_x}{\rho c_p}\left(1+\frac{r_s}{r_x}+\frac{r_s}{r_a}\right) - T_a \frac{r_s}{r_a} \quad (4.66)$$

where T_a is the measured air temperature; the final computation of the canopy temperature is then given by:

$$T_c = T_{c,lin} + \Delta T_c \quad (4.67)$$

The first estimation of soil surface temperature (T_s) is obtained in a nonlinear relationship between T_{rad} and T_c by solving equation 4.52:

$$T_s = \left(\frac{T_{rad}^4 - f_c T_c^4}{1-f_c}\right)^{1/4} \quad (4.68)$$

Air temperature in the canopy (T_{ac}) is related to the resistance and the soil and canopy temperatures, and can be obtained by the following equation:

$$T_{ac} = \frac{\frac{T_a}{r_a}+\frac{T_s}{r_s}+\frac{T_c}{r_x}}{\frac{1}{r_a}+\frac{1}{r_s}+\frac{1}{r_x}} \quad (4.69)$$

After obtaining and separating the different temperature components, the sensible heat fluxes arising from soil surface is primarily estimated as:

$$H_s = \rho c_p \frac{T_s - T_{ac}}{r_s} \quad (4.70)$$

The sensible heat flux (*H*) on land surface is computed by summing H_c and H_s:

$$H = H_c + H_s \quad (4.71)$$

As a result, TSEB gives the first estimation of the sensible heat flux (*H*) under the initial assumption of neutral stability. Similarly to SEBAL, an

iterative process that uses the Monin-Obukov approach is applied to define stability conditions. This iterative flux-profile process is crucial in the retrieval of sensible heat flux. The Obukhov length (L) is used to define the atmospheric stability. For $L \geq 0$, the atmosphere is considered neutral to stable, and the initial estimation of H is accepted. If $L>0$, the atmosphere is considered unstable. The friction velocity (u^*), the aerodynamic resistance (r_a) and the wind speed at the top of the canopy (u_c) are corrected for atmospheric stability by applying the parameters of momentum (ψ_m) and heat transport stability (ψ_h) to the following equations:

$$r_{ah} = \frac{ln\left(\frac{z_T - d_0}{z_{0h}}\right) - \psi_h}{u^* \times \kappa} \tag{4.72}$$

$$u^* = \frac{u_{200}\kappa}{ln\left(\frac{z_u - d_0}{z_{0m}}\right) - \psi_m} \tag{4.73}$$

$$u_c = u_x \left[\frac{ln\left(\frac{h_c - d_0}{z_{0m}}\right)}{ln\left(\frac{z_u - d_0}{z_{0m}}\right) - \psi_m}\right] \tag{4.74}$$

The resistances, wind speed, and temperature parameters are recalculated based on the new corrected values of u^*, r_a and u_c. The new values of wind speed above the soil surface u_s, resistance to the sensible heat just above the soil surface (r_s), resistance of the boundary layer of canopy leaves (r_c), canopy temperature (T_c), soil temperature (T_s) and air temperature in the vegetation-air layer (T_{ac}) are used to calculate a new value of soil sensible heat flux (H_s) in an iterative process until the value of H_s stabilizes. Atmosphere stability functions are computed as a function of sensible heat flux. After closing this iterative cycle and given the first estimation of H_s, under an initial hypothesis of potential evapotranspiration, the first estimation of the evaporation rate for the soil (λEs) can be estimated by solving the soil surface energy balance equation as follows:

$$\lambda E_s = R_{ns} - G_0 - H_s \tag{4.75}$$

where the net radiation flux at the soil surface (R_{ns}) and the soil heat conduction flux (G_0) are estimated with Eq. 4.49 and 4.51 respectively.

A schematic description of the first iterative cycle of TSEB model representing potential conditions and evidencing the connections, the primary inputs and the procedure of *H* retrieval is shown in Figure 4.6.

The first estimation is soil evaporation λE_s, computed by Eq. 4.75. If λE_s is positive, the initial hypothesis is confirmed, and the current solution for soil and canopy energy fluxes partitioning is accepted.

If λE_s is negative, it can indicate dry soil conditions, and thus the initial estimation is not accepted. λE_s is set to zero and a new solution of *H* under the hypothesis "no soil evaporation" is proposed.

The new value of soil sensible heat flux (H_s) is obtained by the following Eq. 4.76, and a new value of soil surface temperature (T_s) is estimated by using Eq. 4.77 as:

$$H_{s2} = R_{ns} - G_0 \tag{4.76}$$

$$T_s = \frac{Hs_2 r_s}{\rho c_p} + T_{ac} \tag{4.77}$$

The canopy temperature (T_c) is recomputed by solving Eq. 4.52 as follows:

$$T_c = \left[\frac{T_{rad}^4 - (1-f_c)T_s^4}{f_c}\right]^{1/4} \tag{4.78}$$

A new estimation of air temperature in the canopy (T_{ac}) is obtained by using Eq. 4.69. Moreover, a new value of the sensible heat flux in canopy layer (H_c) is calculated as:

$$H_c = \frac{[\rho c_p (T_c - T_{ac})]}{r_x} \tag{4.79}$$

The sensible heat flux (*H*) on land surface is recomputed by using Eq 4.71 and, as done previously, the Monin-Obukhov iterative process is applied until the value of H_c stabilizes. After closing this new iterative cycle, the new H_c value overwrites the first one, so that the new value of λET_c is lower than the previously estimated $\lambda ETc_{P\text{-}T}$, referred to potential evapotranspiration The new canopy evapotranspiration is computed as:

$$\lambda ET_c = R_{nc} - H_c \quad (4.80)$$

A schematic description of the second iterative cycle of TSEB model representing ‘‘no evaporation from soil’’ is shown in Figure 4.7.

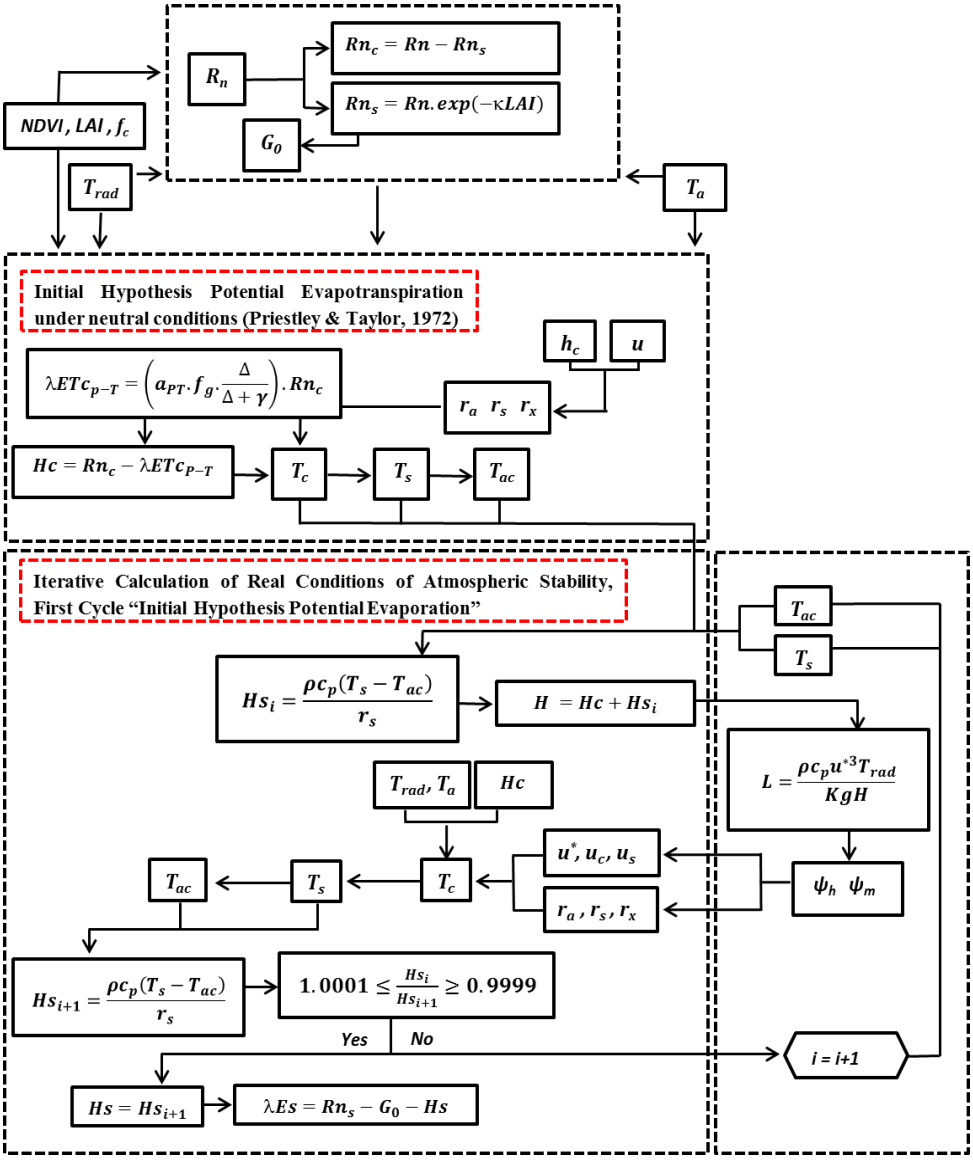

Figure 4.6: Schematic representation of TSEB first iterative cycle and soil sensible heat flux (H_s) retrieval under the hypothesis of potential conditions (absence of crop stress).

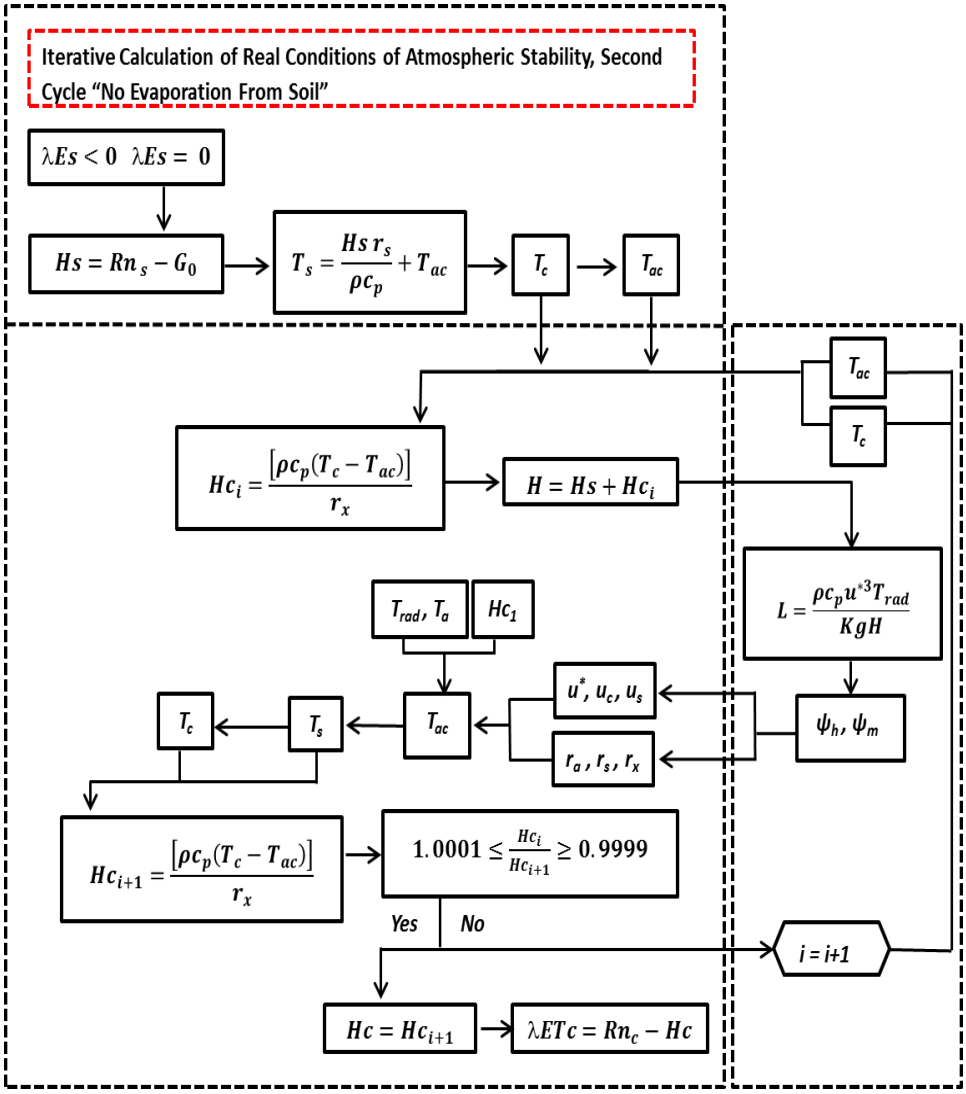

Figure 4.7: Schematic presentation of the TSEB second iterative cycle and soil sensible heat flux (H_c) retrieval under the hypothesis of no soil evaporation.

After the second iteration, if λET_c is negative, it means that the sensible heat flux at the canopy is higher than the net radiation at the canopy surface ($H_c > R_{nc}$), which is impossible. In this case, the crop transpiration (λET_c) is set to zero so that the radiation on the canopy surface is transferred entirely into sensible heat, and the energy balance

closure is addressed (R_{nc}=H_c). In this condition areas with zero evapotranspiration are identified, Under this new condition the canopy temperature (T_c) was reobtained from Eq.4.78. The soil surface temperature (T_s) is computed by using Eq. 4.68 which yields the sensible heat flux at the soil surface (H_s) (Eq. 4.70); moreover, since λET is set to zero the soil heat flux G_0 is computed as:

$$G_0 = R_{ns} - H_s \tag{4.81}$$

Finally, new values of T_s, T_c and T_{ac} that satisfy the soil-surface and the canopy energy balances are obtained from the sensible heat fluxes.

$$T_{ac} = T_a + \frac{H.r_{ah}}{\rho c_p} \tag{4.82}$$

$$T_s = T_{ac} + \frac{Hs.r_s}{\rho c_p} \tag{4.83}$$

$$T_c = T_{ac} + \frac{Hc.r_x}{\rho c_p} \tag{4.84}$$

In TSEB, the instantaneous latent heat flux (λET) is given as the sum of the previously partitioned soil evaporation (λE_s) and canopy transpiration (λET_c) and then as:

$$\lambda ET = \lambda ET_c + \lambda E_s \tag{4.85}$$

4.9 Eddy covariance measurements, Energy balance closure and Bowen ratio

Data acquired by the flux tower (distributed over 24 h) referred to the days of satellite image acquisition, were averaged over half-hourly time-step. Net radiation (R_n, W m^{-2}) was obtained by balancing short-wave radiation and long-wave radiation both measured by four components radiometer. Soil heat flux (G_0) (W m^{-2}) was measured by using soil heat plate*;* the flux plate sensors measure accounting for the actual soil thermal conductivity by means of a Huckseflux self-calibrating heat flux sensor (Huckseflux, 2013).

The eddy covariance (EC) measurements data were processed by following the standard EUROFLUX rules (Aubinet et al., 2000). Sensible heat flux (H, W m^{-2}) was evaluated by considering the covariance between the vertical velocity fluctuation of horizontal wind and air temperature (EC technique, Kaimal and Finnigan, 1994) as follows :

$$H = \rho c_{p\,\sigma_{wT}} \tag{4.86}$$

where, ρ (g m^{-3}) is the air density, c_p (J g^{-1} $^{\circ}K^{-1}$) is the air specific heat capacity at constant pressure, and σ_{wT} (m s^{-1} K) is the covariance between the vertical wind speed and air temperature.

Similarly, latent heat flux (λET, W m^{-2}) was derived by considering the covariance between the vertical velocity fluctuation of horizontal wind and the water vapor density (Kaimal and Finnigan, 1994), expressed as:

$$\lambda ET = \lambda c_{\sigma_{wq}} \tag{4.87}$$

where λ is the latent heat of vaporization (J kg^{-1}) and $c_{\sigma_{wq}}$ (m s^{-1} $^{\circ}$K) is the covariance between the vertical wind speed and water vapor concentration.

The H component is then adjusted by applying linear de-trending (Moncrieff *et al.*, 2004), coordinate rotation (Finnigan et al., 2003) and spectral loss correction (Liu and Peters, 2001; Schotanus et al., 1983), whereas λET is adjusted by applying the same corrections used for H and also the Webb, Penmann, and Leuning corrections (Webb et al., 1980).

In order to verify the reliability of the data measurements, it was necessary to carry out a data check of how well the turbulent fluxes H and λET account for the available energy (R_n–G_0). The surface energy balance closure ratio, C_R, as suggested by Prueger et al. (2005), was evaluated only when R_n resulted greater than 100Wm^{-2}:

$$C_R = \frac{H+\lambda ET}{Rn-G_0} \tag{4.88}$$

To compare remotely sensed based model outputs and measured fluxes, the energy closure was forced, targeting to preserve the Bowen ratio. An error of ±15% in remote sensing surface energy balance estimations is

considered acceptable (Allen et al., 2011), thus the balance closure was considered satisfactory when C_R > 0.85 (Prueger et al., 2005; Wilson et al., 2002).

When C_R value is not satisfactory, the turbulent fluxes are adjusted by using the Bowen ratio closure method, in which the Bowen ratio, β, is expressed as (Prueger et al., 2005):

$$\beta = \frac{H}{\lambda ET} \tag{4.89}$$

R_n and G_0 measurements are more accurate than the turbulent fluxes H and λET. The Bowen ratio method assumes that errors in the measured available energy is negligible and therefore forces the closure of surface energy by attributing available energy between to H and λET, by using the coefficient β This approach rearranges the SEB equation as follows:

$$R_n - G_0 = (H + \Delta H) + (\lambda ET + \Delta \lambda ET) \tag{4.90}$$

where, ΔH and $\Delta \lambda ET$ represent the closure errors for H and λET, respectively.

The first term used in the correction of λET is obtained as:

$$\Delta \lambda \mathrm{ET} = \frac{(\mathrm{R_n}\text{-}\mathrm{G_0})\text{-}(1+\beta)\lambda \mathrm{ET}}{(1+\beta)} \tag{4.91}$$

The corrected values of the latent heat flux, expressed as $\lambda ET_{clos.,}$ was computed as follows:

$$\lambda ET_{clos.} = \lambda ET + \Delta \lambda ET \tag{4.92}$$

The second correction terms was computed as:

$$\Delta H = \beta(\lambda ET + \Delta \lambda ET) - H \tag{4.93}$$

moreover, the corrected values of the sensible heat flux ($H_{clos.}$) is equal to:

$$H_{clos} = H + \Delta H \tag{4.94}$$

4.10 Temporal Upscaling

Instantaneous actual evapotranspiration (ET_a, mm hr^{-1}) at the hour of satellite image acquisition is calculated as follows:

$$ET_a = 3600 \frac{\lambda ET}{\lambda} \quad (4.95)$$

where λ (J kg^{-1}) is the latent heat of vaporization and 3600 converts from seconds to hours.

Up-scaling instantaneous values of evapotranspiration into a more useful monthly and seasonal values implies firstly to upscale ET_a to daily values and extrapolate those daily values to monthly and seasonal values. To upscale ET_a from instantaneous satellite overpass time into the actual daily evapotranspiration values ($ET_{a,D}$) two reliable methods are used. The first is the instantaneous evaporative fraction (Λ) computed from the instantaneous surface energy balance components, while the second method uses the incoming shortwave radiation as an integration factor.

Extrapolation of up-scaled $ET_{a,D}$ to longer periods values can be done by using daily reference evapotranspiration obtained from meteorological data.

4.10.1 Upscaling Instantaneous to daily evapotranspiration.

The instantaneous evaporative fraction (Λ) computed from the instantaneous surface energy balance components is used to upscale instantaneous ET to daily values under the hypothesis of day-time self-preservation. The daily evapotranspiration $ET_{a,D}$ is obtained as follows:

$$ET_{a,D} \approx \Lambda \frac{R_{n24}}{\lambda \rho_w} \quad (4.96)$$

where R_{n24} (MJ m^{-2} d^{-1}) is the net daily radiation, λ (MJ m^{-3}) is the latent heat of vaporization and ρ_w (kg.m^{-3}) is the water density.

The evaporative fraction (Λ) can be computed as the ratio of λET to available energy as follows:

$$\Lambda = \frac{\lambda ET}{R_n - G_0} \quad (4.97)$$

R_{n24} is estimated using 24-h integrated meteorological variables adopting the procedure outlined in the FAO Irrigation and Drainage Paper No. 56 (Allen et al., 1998).

4.10.2 Daily to seasonal evapotranspiration

Monthly and seasonal evapotranspiration "maps" are often desired for quantifying total water consumption from agriculture. Each Landsat TM image is set to represent a period of time; the images are set to cover irrigation seasons of investigated years (May-September). Reference evapotranspiration (ET_0) obtained at the meteorological stations is used to extrapolate $ET_{a,D}$ over days between images. It was assumed that actual daily evapotranspiration computed at the image acquisition time changes similarly to reference evapotranspiration at the meteorological station for the entire period represented by each image. ET_0 is therefore used as an index of the relative change in weather. According to this assumption, the corresponding daily actual evapotranspiration (ET_D) is calculated as:

$$ET_D = \frac{ET_{0,ID}}{ET_{0,D}} \times ET_{a,ID} \quad (4.98)$$

where, $ET_{0,ID}$ is the daily reference evapotranspiration corresponding to the acquisition day, $ET_{0,D}$ is the corresponding daily reference evapotranspiration and $ET_{a,ID}$ is the actual evapotranspiration calculated at the day of image acquisition.

Monthly ET ($ET_{monthly}$), that can be obtained by using a single or more than one image covering the month (from day m to day n), is calculated as:

$$ET_{monthly} = \sum_{i=m}^{n} ET_D \quad (4.99)$$

The seasonal evapotranspiration is calculated as a sum $ET_{monthly}$ as follows:

$$ET_{season} = \sum ET_{monthly} \quad (4.100)$$

4.11 Irrigation application efficiency

Irrigation system performance was assessed for both investigated cases at hydrant level, on monthly and seasonal bases; the estimated upscaled remotely sensed $ET_{monthly}$ are compared to measured water consumption downstream hydrants, accounting for the on-field irrigation application efficiency

Irrigation system performance was indexed based on the ratio between the volumes of evapotranspiration estimated by remote sensing (accounting for irrigation system efficiency), and the corresponding volumes actually distributed by hydrants in the district.

A general expression of irrigation performance at hydrant level, on a monthly basis, is given by:

$$IP_{H,monthly} = \frac{ET_{monthly}}{IE * V_{monthly}} \quad (4.101)$$

where *IE is the total* irrigation system application efficiencies, and $V_{monthly}$ is the volumes delivered downstream hydrants.

The main purpose of this indicator is to quantify the efficiency of water application on hydrant and irrigation district level. The remote sensing retrieved actual evapotranspiration is used as a reference to quantify the application efficiency of delivered water resources.

Chapter 5: Results

Results are presented within two main sections; the first illustrates the outcomes of the surface energy balance application in SAT Llano Verde district, which is characterized by uniform and homogeneous crops (no fragmentation) and thus, a single source SEB was applied. The second assesses the potential of SEB applications when monitoring irrigation over sparse vegetation, such as those characterizing the district 1/A of the Consorzio di Bonifica di Agrigento 3. Within this latter, SEB models were compared to measurements of an eddy covariance tower installed within olive groves. In this section, particular attention is given to the temporal upscaling methodologies. Finally, the potential of SEB models applications in the case study is discussed.

5.1 Application of SEBAL model in SAT Llano Verde district, Spain

The first part of this section reports the results of the application of SEBAL model in SAT Llano Verde agricultural district for irrigation seasons (from May to September) 2006, 2007 and 2008. SEBAL model was run by using the Landsat 5 Thematic Mapper (TM) images and some ancillary meteorological data obtained at the hour and day of image acquisition. Twenty-six TM images were used to cover the three irrigation seasons. Subset images were made for the area of interest, georeferenced and processed to produce a layered spectral bands image, required to apply the surface energy balance model.

In particular, the spatial distribution of the different terms appearing in the surface energy balance equation is presented. The same methodology was applied to all available images. However, to simplify the results presentation and since the application is the same, only the image retrieved on May 7, 2007 (DOY 127) is used as an example for which obtained maps are shown in the following sections.

5.1.1 Surface albedo

Broadband shortwave surface albedo (α) is strongly influenced by land cover, soil, vegetation and surface water content. Allen et al. (1987) stated that a hypothetical grass reference crop has an albedo value of 0.23. The surface albedo varies between 0 and 1 and a value of 0.23 means that 23% of the incoming solar radiation is reflected. In the examined study case, albedo values ranged from a minimum of 0 to a maximum value of approximately 0.4. The mean value of the subset image resulted equal to 0.19. Figure 5.1 shows the spatial distribution map of surface albedo, as well as the distribution histogram and main statistics (minimum, maximum, mean and standard deviation).

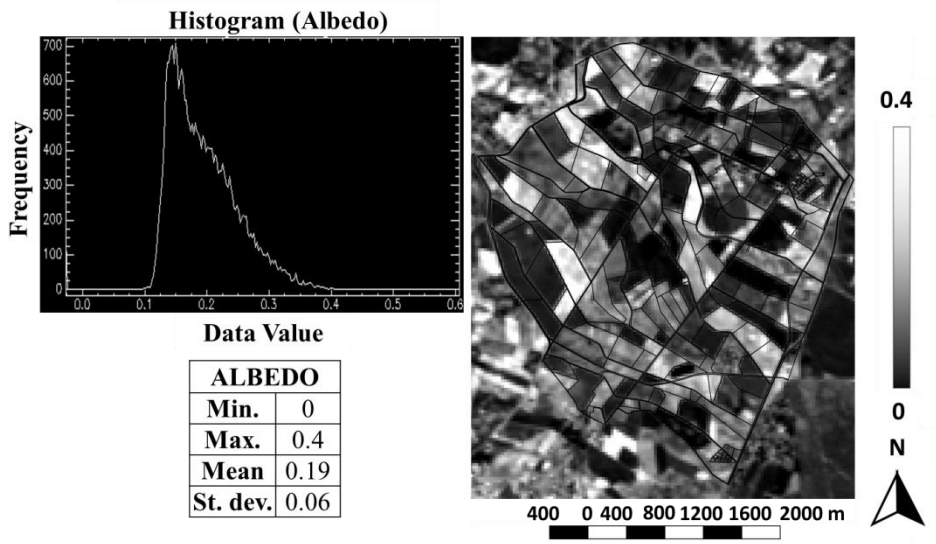

ALBEDO	
Min.	0
Max.	0.4
Mean	0.19
St. dev.	0.06

Figure 5.1: Spatial distribution of surface albedo, histogram and statistic parameters related to the image acquired on DOY 127 in 2007.

5.1.2 Normalized Difference Vegetation Index

SEBAL model also requires the knowledge of the Normalized Difference Vegetation Index (NDVI), whose values usually range between -1 and +1. Negative values could indicate the presence of water bodies, whereas high NDVI values close to +1 are indicative of dense vegetation. NDVI values close to zero indicate no vegetation and possible urbanized area.

In the proposed application, vegetated regions were then identified based on NDVI, whose values ranged from a minimum of -0.26 and a maximum of approximately 0.87, as illustrated in figure 5.2. As can be observed, vegetated areas were characterized by NDVI values higher than 0.7, whereas bare soil had values lower than 0.2. Figure 5.2 also shows NDVI histogram and main statistics.

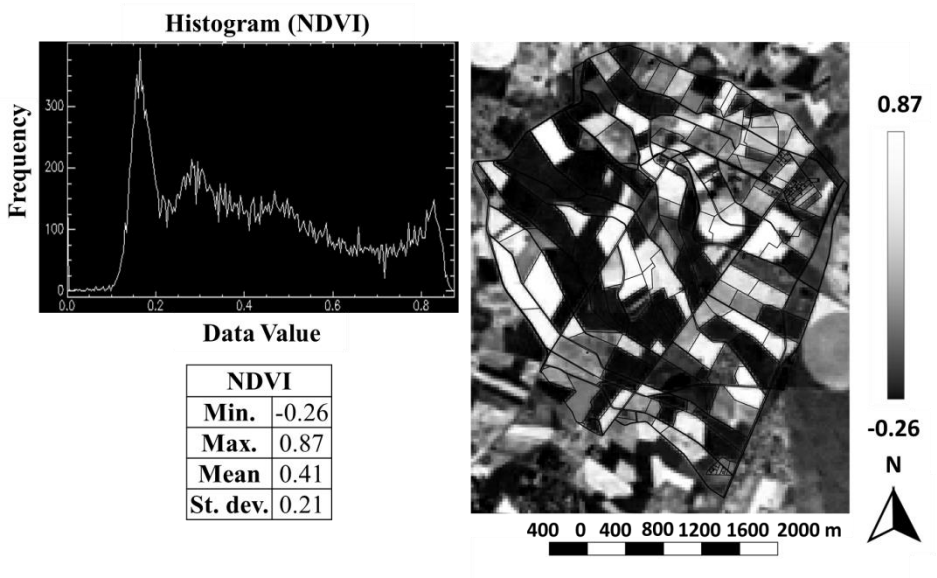

NDVI	
Min.	-0.26
Max.	0.87
Mean	0.41
St. dev.	0.21

Figure 5.2: Spatial distribution of NDVI, histogram, and statistics (image acquired on DOY 127 in 2007).

5.1.3 Net radiation

Total net radiation (R_n) is based on the balance between shortwave and longwave radiations. Generally R_n ranges from -50 Wm^{-2} on a clear night to more than 500 Wm^{-2} on a summer day (Beven, 2001).

In the SAT Llano Verde case study, the total R_n ranged between a minimum value of ≈ 212 and a maximum of ≈707 Wm^{-2}. Figure 5.3 shows the spatial distribution of net radiation, as well as corresponding histogram and statistics.

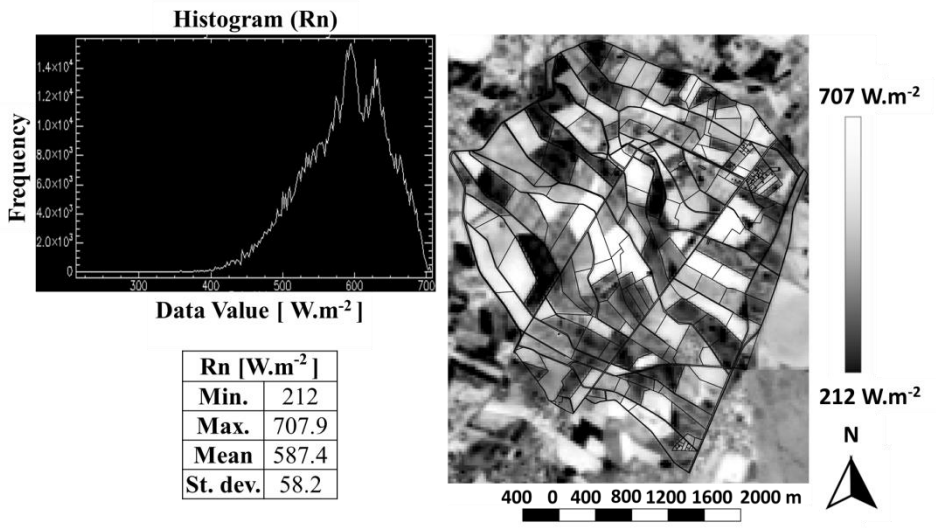

Figure 5.3: Spatial distribution of R_n, histogram, and statistics (image acquired on DOY 127 in 2007).

5.1.4 Soil heat flux

In SEBAL, ground heat flux (G_0) is estimated as a fraction of R_n, based on surface temperature, α and NDVI. Areas characterized by low albedo (e.g., bare dry soils) strongly absorb incoming solar radiation; the presence of vegetative cover reduces soil surface temperature, thus producing relatively low G_0 values. In these areas, low percentage of R_n is transferred to the ground. On the contrary, areas not covered by vegetation are characterized by relatively high G_0 values.

During daytime, heat flux into the ground is positive, the flux is downward from a warmer layer heat is transferred to a cooler underlying ground layer. G_0 value retrieved by SEBAL model ranged between a minimum value of 25.2 and a maximum of approximately 100 Wm^{-2}. According to the heat exchanges between the soil surface and air, G_0 showed to be higher in bare soils than in cultivated areas, where energy is used for evapotranspiration process.

Figure 5.4 shows G_0 map retrieved by SEBAL, as well as the image histogram and related statistics. The mode of G_0 fell in the range 65-98 Wm^{-2}.

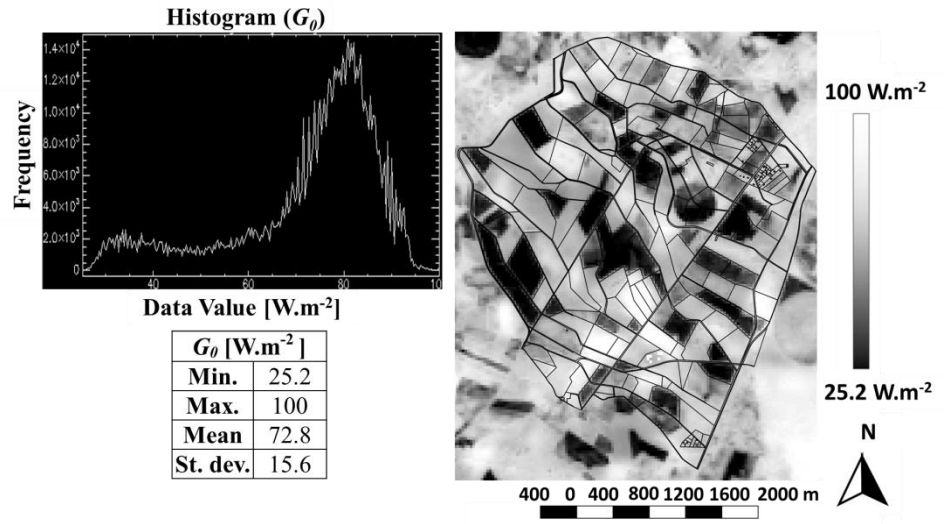

G_0 [W.m^{-2}]	
Min.	25.2
Max.	100
Mean	72.8
St. dev.	15.6

Figure 5.4: Spatial distribution of soil heat flux, histogram and main statistics (image acquired on DOY 127 in 2007).

5.1.5 Sensible heat flux

Sensible heat flux (*H*) is the heat energy transferred between the surface and air when there is a difference in temperature between them. During day-time, when the air is colder than the underneath surface, the heat is transferred upwards to the air (positive sensible heat), thus increasing air temperature and cooling the surface. Heat is initially transferred by conduction between the surface and the air, then by convection due to the air warming up.

Stability corrections for friction velocity and resistance to heat transport are applied using the Monin-Obukhov length, *L* (m), based on an iterative process. Sensible heat flux usually converges rapidly after a few iterations. As expected, retrieved *H* values were always positive and variable between 0 and about 675 W m^{-2}. Bare soils showed higher sensible heat flux than vegetated areas in which energy is mainly used for evapotranspiration processes. Figure 5.5 shows the retrieved spatial distribution of sensible heat flux, its distribution histogram, and the main statistics.

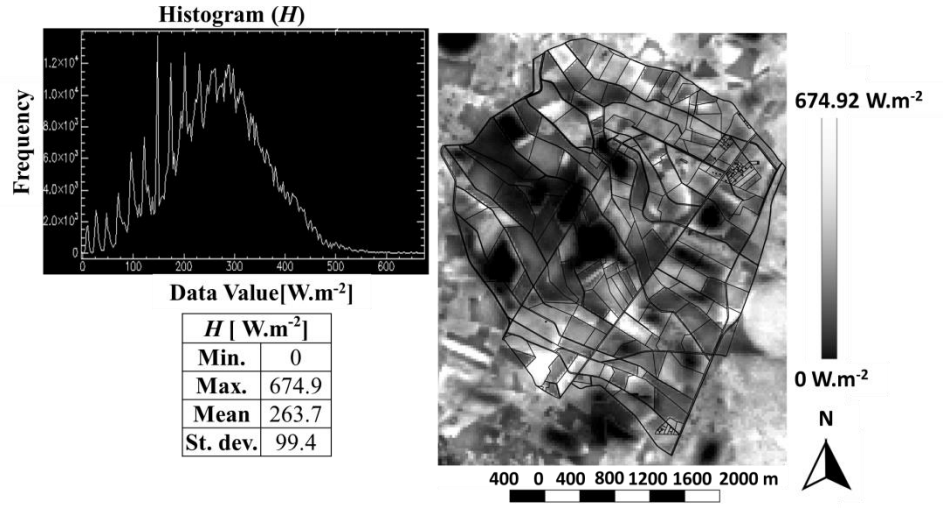

H [W.m^{-2}]	
Min.	0
Max.	674.9
Mean	263.7
St. dev.	99.4

Figure 5.5: Spatial distribution of sensible heat flux, histogram and main statistics (image acquired on DOY 127 in 2007).

5.1.6 Instantaneous latent heat flux

Actual latent heat flux at the instant of image acquisition, λET, is retrieved by SEBAL as residual of surface energy balance, once known R_n, $G_{0,}$ and H.

Instantaneous latent heat flux ranged between 0 and 670 Wm^{-2}, being the lowest values associated to bare soils and the highest to cultivated areas. Figure 5.6 shows the spatial distribution of λET retrieved by SEBAL model, the related histogram and the main statistics.

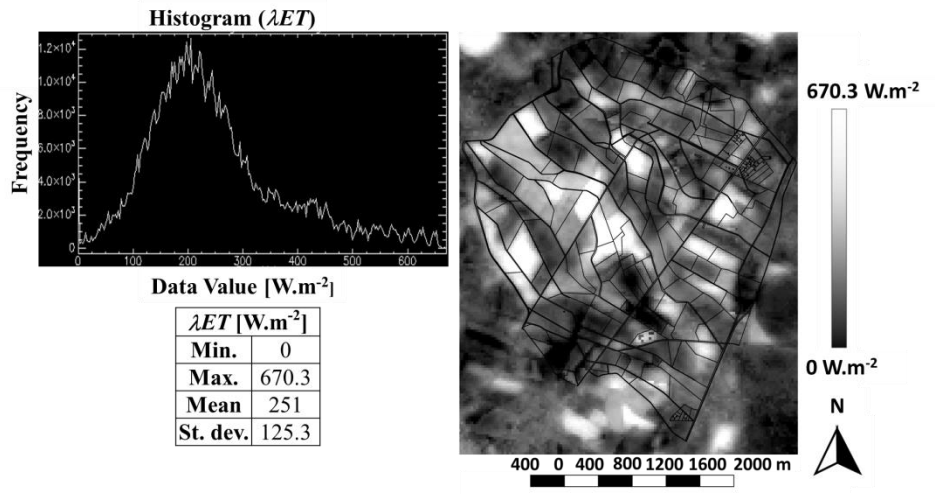

λET [W.m^{-2}]	
Min.	0
Max.	670.3
Mean	251
St. dev.	125.3

Figure 5.6: Spatial distribution of instantaneous latent heat flux, histogram and main statistics (image acquired on DOY 127 in 2007).

5.1.7 Evaporative fraction

Evaporative fraction (Λ), corresponding to the ratio between actual latent heat flux and available energy, mathematically ranges between 0 and 1; the lower limit is associated to the circumstance that all the energy is used as sensible heat flux, whereas the upper limit is associated to the case in which all the energy is used as latent heat flux. In pixels where Λ is lower than 1 evapotranspiration is not at its maximum. The evaporative provides an indication of partitioning energy over the land surface and is used to upscale instantaneous latent heat flux into daily *ET* values by using the self-preservation hypothesis.

Figure 5.7 shows the spatial distribution map of Λ values, the related histogram and main statistics. It is possible to observe that bare soils are characterized by low evaporative fractions and, on the contrary, vegetated areas are characterized by high values of Λ, which indicates that most of the energy is used as latent heat flux.

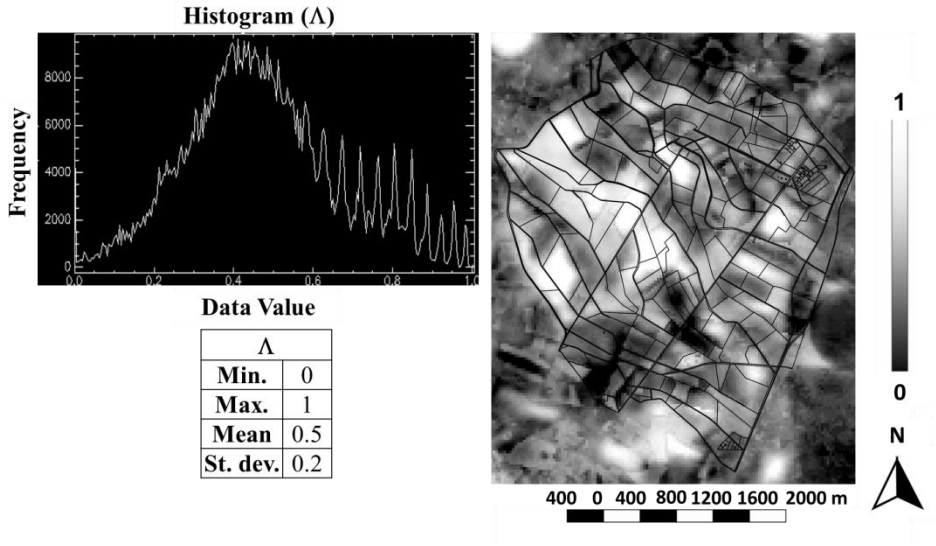

Figure 5.7: Spatial distribution of evaporative fraction, histogram and main statistics (image acquired on DOY 127 in 2007).

5.1.8 Daily net radiation, R_{n24}

The retrieval of day net radiation, R_{n24}, is mandatory to upscale instantaneous fluxes to daily values. By applying the FAO-56 (Allen et al., 1998) formulation, R_{n24} reached a minimum value of 69.9 and a maximum of about 255.8 Wm^{-2} (corresponding to 6.04 and 22.1 $MJm^{-2}d^{-1}$, using a conversion factor of 1 $MJm^{-2}d^{-1}$ = 0.0864 * Wm^{-2}.

Figure 5.8 shows the spatial distribution map of R_{n24} retrieved by SEBAL model, the corresponding histogram and main statistics. Bare soils showed, of course, the lowest R_{n24}.

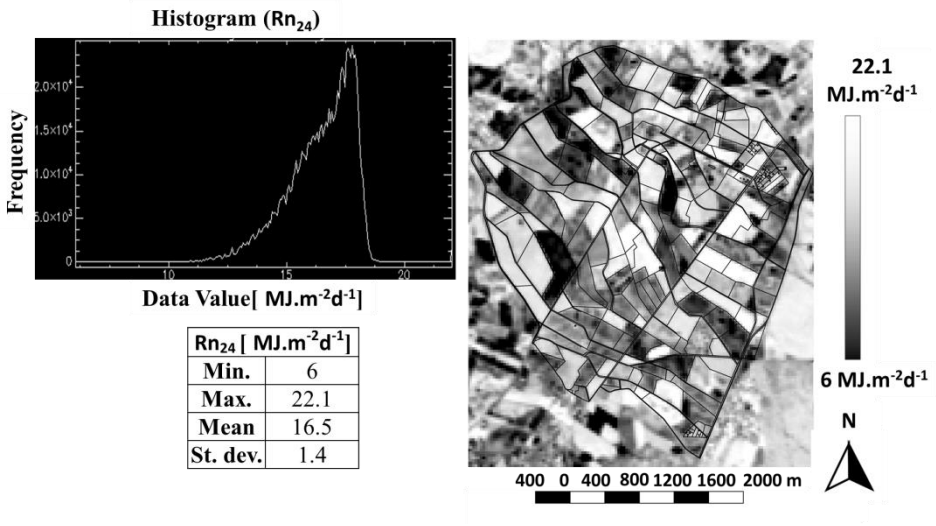

Rn_{24} [MJ.m^{-2}d^{-1}]	
Min.	6
Max.	22.1
Mean	16.5
St. dev.	1.4

Figure 5.8: Spatial distribution of R_{n24}, histogram and main statistics (image acquired on DOY 127 in 2007).

5.1.9 Daily Evapotranspiration

The hypothesis of self-preservation of the evaporative fraction was used to upscale the instantaneous latent heat flux to actual daily evapotranspiration $ET_{a,ID}$ (mm).

Cultivated areas exhibited high $ET_{a,ID}$ values, with a maximum value of approximately 7 mm·d^{-1}, where bare soils were characterized by the lowest values. Figure 5.9 shows the spatial distribution map of daily evapotranspiration retrieved by SEBAL, the pixel distribution histogram and the related statistic parameters.

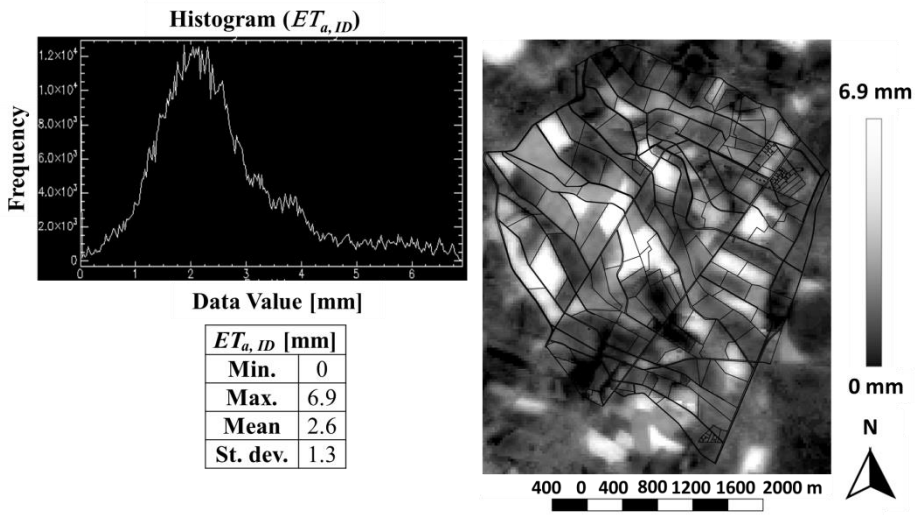

$ET_{a, ID}$ [mm]	
Min.	0
Max.	6.9
Mean	2.6
St. dev.	1.3

Figure 5.9: Spatial distribution of $ET_{a,ID}$, histogram and main statistics (image acquired on DOY 127 in 2007).

It was therefore assumed that the dynamic of daily evapotranspiration obtained by upscaling instantaneous *ET* values, $ET_{a,ID,}$ at the image acquisition day for the entire area of interest, changes in proportion to reference evapotranspiration (ET_0) evaluated at the meteorological stations. This assumption was validated in a set of experiments by Allen et al., (2007a), it was used to deduce daily evapotranspiration for days between processed images, ET_D. The methodology used to obtain ET_D is conceptually similar to the seasonal crop coefficient (K_c) curve. However, it has the advantage that it requires no data related to the crop and its development stage.

An example of temporal extrapolation of $ET_{a,ID}$ acquired by SEBAL on the 7th of May 2007 and over two different fields (Alfalfa and Barley) is shown in figure 5.10. Figure 5.10 shows the extrapolation approach applied to fill the data gaps between cloud-free satellite acquisitions. The extrapolated values ET_D shows similar trend of variability when compared to the SIAR meteorological station measured $ET_{0.D}$

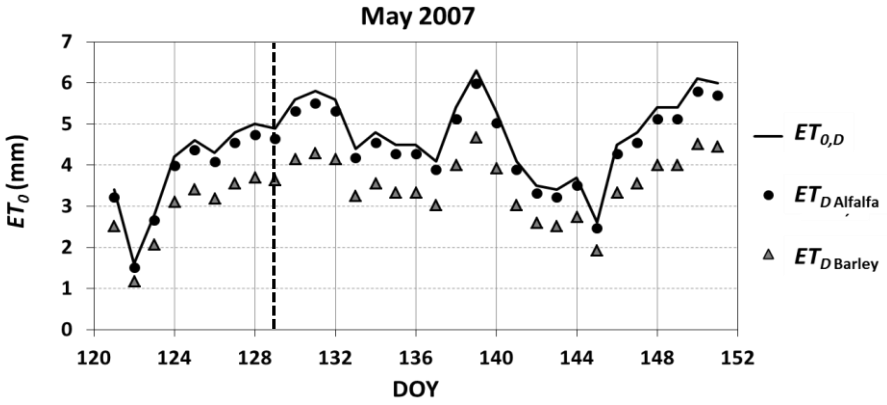

Figure 5.10: Temporal upscaling related to May 2007, over 2 different fields (alfalfa and barley). The dashed line represents the image acquisition day.

5.1.10 Monthly and seasonal evapotranspiration

Once ET_D was deduced between acquisition dates, the cumulative actual evapotranspiration of the entire period represented by each image was obtained, as well as monthly and seasonal evapotranspiration computed for the areas downstream each hydrant, representing one or more farms. Each Landsat TM image was set to represent a certain period of time in order to cover the whole investigated irrigation seasons (May-September). Tables 5.1, 5.2 and 5.3 summarize the period to which each image was referred. Because of the lack of cloud-free scenes of TM images, in some cases, a single image was set to cover an entire month, while in other cases represented a period of less than 10 days. However, Allen et al., (2007a), showed that only one or two satellite image snapshots per month can be sufficient to estimate seasonal evapotranspiration.

Table 5.5: Date of Landsat TM image acquisition and related periods during irrigation season 2006.

Date (dd/mm)	DOY	Initial day (dd/mm)	Final day (dd/mm)
27/04	117	01/05	31/05
05/06	156	01/06	16/06
21/06	172	17/06	30/06

30/06	181	01/07	10/07
16/07	197	11/07	31/07
08/08	220	01/08	15/08
24/08	236	16/08	31/08
18/09	261	01/09	30/09

Table 5.6: Date of Landsat TM image acquisition and related periods during irrigation season 2007.

Date (dd/mm)	DOY	Initial day (dd/mm)	Final day (dd/mm)
07/05	127	01/05	31/05
24/06	175	01/06	30/06
03/07	184	01/07	10/07
19/07	200	11/07	20/07
26/07	207	21/07	31/07
04/08	216	01/08	15/08
27/08	239	16/08	31/08
05/09	248	01/09	19/09
28/09	271	20/09	30/09

Table 5.7: Date of Landsat TM image acquisition and related periods during irrigation season 2008.

Date (dd/mm)	DOY	Initial day (dd/mm)	Final day (dd/mm)
02/05	122	01/05	31/05
19/06	170	01/06	20/06
26/06	176	21/06	30/06
05/07	186	01/07	15/07
21/07	202	16/07	31/07
13/08	225	01/08	15/08
22/08	234	16/08	31/08
14/09	257	01/09	20/09
30/09	273	21/09	30/09

5.2 ET estimates by SEBAL model and water volumes delivered to hydrants

Quantifying ET_D at field level allowed the estimation of water demand at hydrants that should have been used to irrigate the considered fields. Field water demand calculated by SEBAL was slightly augmented to account for irrigation efficiency that, was assumed equal to 85% as indicated by the irrigation association managers. The considered irrigation efficiency is allocated to water losses due to deep percolation and irrigation system losses. This section reports the comparison between irrigation water requirement estimated by application of SEBAL model and the corresponding actual water consumption supplied by hydrants. Due to the difficulty to know the exact irrigation timing downstream each hydrant, the comparison was done at monthly and seasonal scales. As mentioned in the theoretical background, since the SEBAL model was extensively validated by eddy covariance towers in Castilla la Mancha region (Bastiaanssen et al., 1998), and as it was proven that the model estimations are more accurate than those obtained with the FAO-56 Penman-Monteith (Allen et al., 1998), actual *ET* values were therefore assumed as reference to assess the potential water saving in the examined irrigation district. Is important to highlight that irrigation is applied intensively without producing any water stress on cultivated crops (validated from the irrigation system managers). Thus, allowing to consider SEBAL estimated latent heat fluxes as a reference to asses irrigation application efficiency at both hydrant and district levels.

Before discussing this comparison, it is useful to remember that some hydrants were used for purposes different than irrigation, such as animal productions or others. This circumstance can explain the large differences sometimes observed, between measured water volumes delivered to hydrants and SEBAL estimates. On the contrary, for some hydrants, estimates from SEBAL model resulted quite higher than the volumes delivered to the hydrants, due to improper irrigation practices; however, it was confirmed by irrigation managers that the only source of water for farmers was represented by the irrigation distribution system.

Figure 5.11 shows that measured water distributed by hydrants was approximately 12% lower than model estimates for irrigation season

2006, while it was greater for seasons 2007 and 2008 23 and 35% respectively. This can be explained by considering that irrigation demand in May generally accounted for monthly precipitation which was relatively significant during this month. During May was recorded 52.8, 22.4 and 107.6 mm of precipitation for the years 2006,2007and 2008 respectively. The temporal aggregation at monthly basis could explain the observed dispersion of data, consequent to the lack of information on the irrigation timing. Rainfall reduced the irrigation demand significantly; of course, if on a hand a fraction of effective precipitation is accounted in SEBAL, on the other hand, it is not included in the water volumes distributed by hydrants. By observing figure 5.12, it is evident that even though precipitation in May 2006 was significant, it was quite lower than evaporative demand represented by the reference ET_0 estimated at the meteorological station (grey bars). According to figure 5.11, hydrants can be categorized into two main groups, the first of which includes those delivering water volumes almost equals to model estimated *ET* and the second group for which the delivered volumes exceeded the model estimates. The generally low volumes delivered to hydrants in May 2008 were consequent to the abundant precipitation (107.6 mm) of the period that resulted only slightly lower than reference ET_0 (120 mm)(fig. 5.12). If considering the linear relationships existing between the two variables, characterized by a coefficient of determination (R^2) of 0.67, 0.51 and 0.41, respectively for May 2006, 2007 and 2008, it is confirmed that generally irrigation scheduling practiced by farmers accounted for the rainfall occurring in May period.

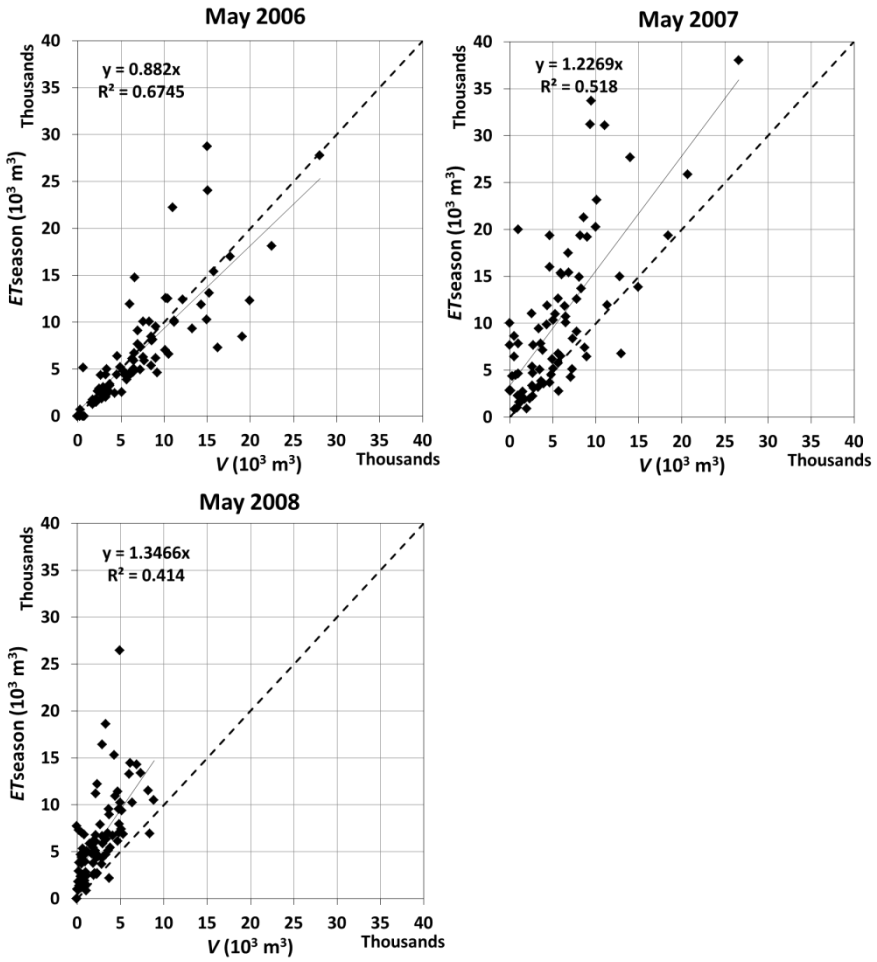

Figure 5.11: Monthly evapotranspiration volumes estimated by SEBAL model vs. water volumes, *V*, delivered to hydrants in May 2006, 2007 and 2008.

As shown in figure 5.13, evapotranspiration volumes estimated in June by SEBAL were generally lower than or equal to the corresponding water volumes delivered to hydrants.

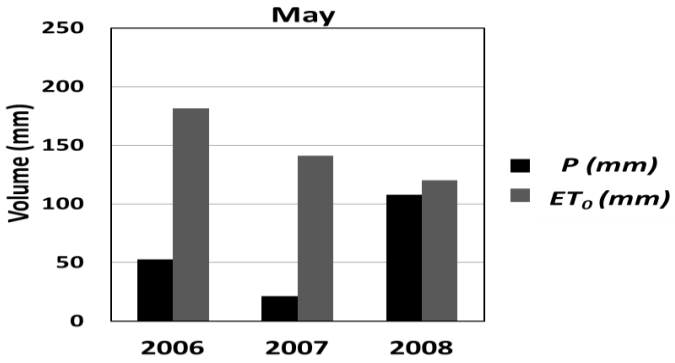

Figure 5.12: Precipitation (*P*) and reference evapotranspiration (ET_0) in May 2006, 2007 and 2008.

Differences between model estimates *ET* values and corresponding measured volumes in the three years were, to some extent, variable. The lowest differences were observed in June 2008 due to the higher precipitation and the contextually lower evaporative demand, as shown in figure 5.14. June 2008 differs from May 2008 even though the evaporative demand and the precipitation data seem similar. This was due to the effectiveness of precipitation occurring in June 2008, the most of which (about 90%) raised in only two consecutive days (8 and 9 June) which decreased significantly the effectiveness of precipitation water. Similarly to May, even in June, a few hydrants were out of scale because of water uses different than irrigation. However, even in June strong linear relationships were observed, with a coefficient of determination of about 0.69, 0.75 and 0.81 for 2006, 2007 and 2008 respectively.

As shown in figure 5.15, during July, in the three years the trend was quite similar: *ET* volumes estimated by SEBAL model generally resulted lower than the corresponding volumes delivered to hydrants. Figure 5.16 shows the relatively high evaporative demand and the practically absent precipitations, except in 2008, when only 3 mm of rainfall were recorded. As shown in figure 5.15, even in July good correlations between data were observed, with R^2 values of about 0.86, 0.87 and 0.77 for 2006, 2007 and 2008 respectively.

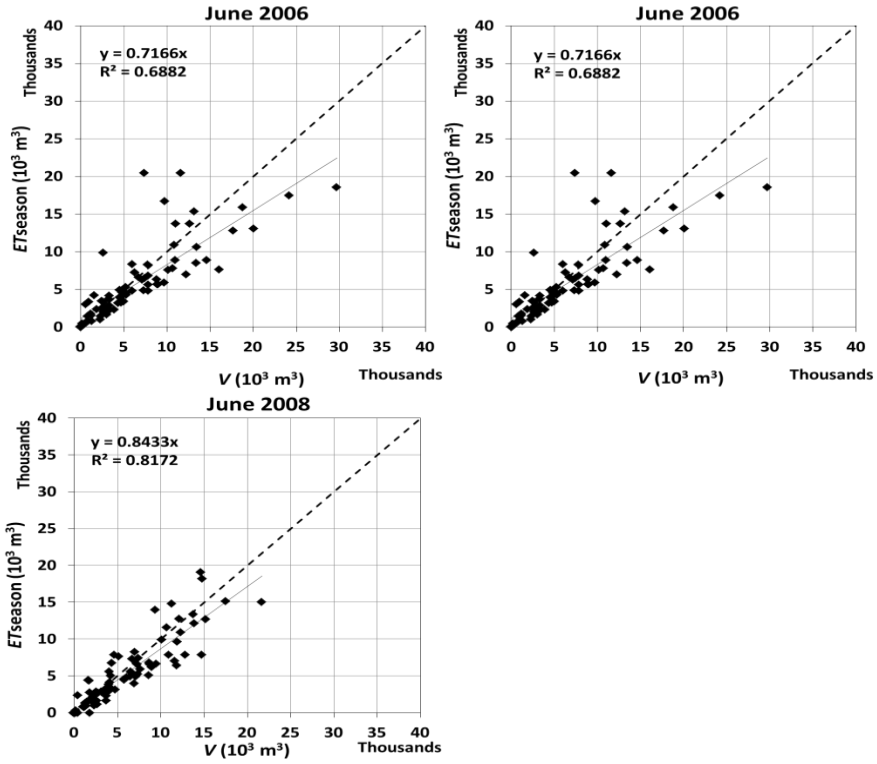

Figure 5.13: Monthly evapotranspiration volumes estimated by SEBAL model vs. water volumes delivered to hydrants in June 2006, 2007 and 2008.

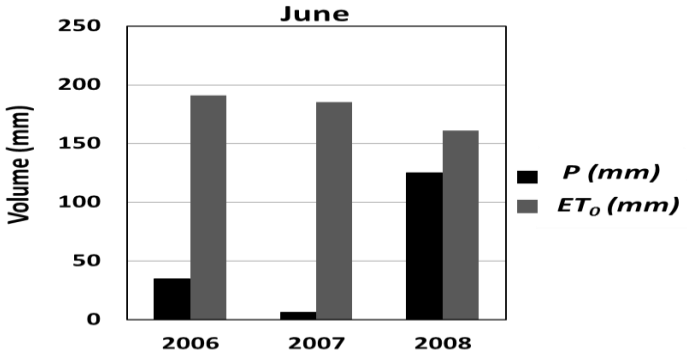

Figure 5.14: Precipitation (P) and reference evapotranspiration (ET_0) in June 2006, 2007 and 2008.

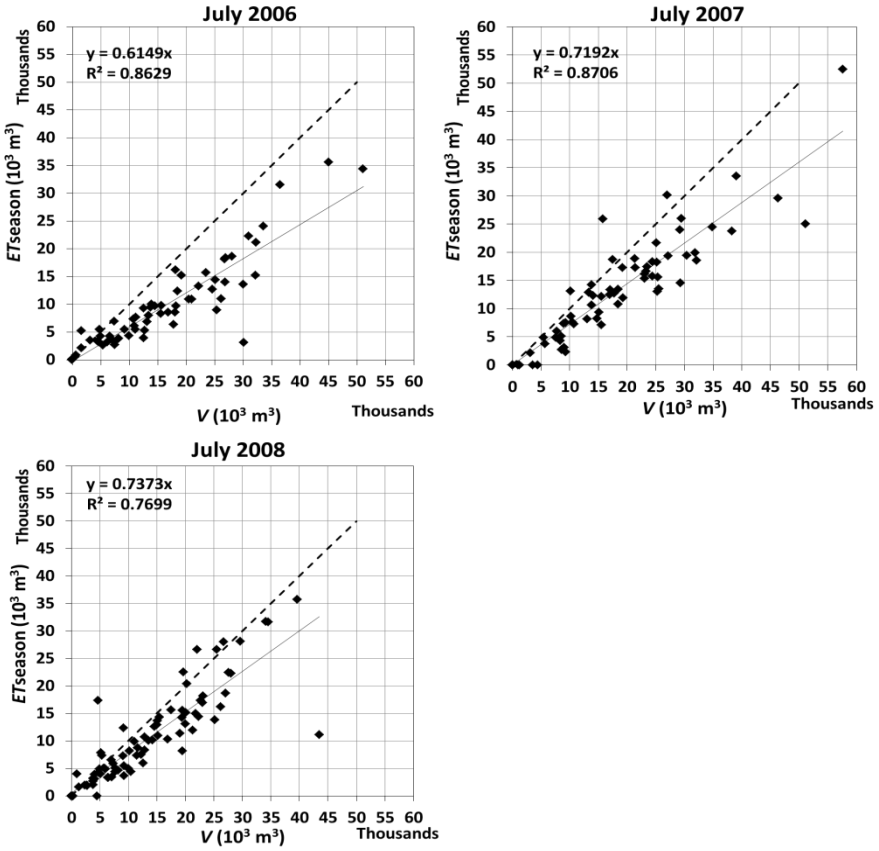

Figure 5.15: Monthly evapotranspiration volumes estimated by SEBAL model vs. water volumes delivered to hydrants in July 2006, 2007 and 2008.

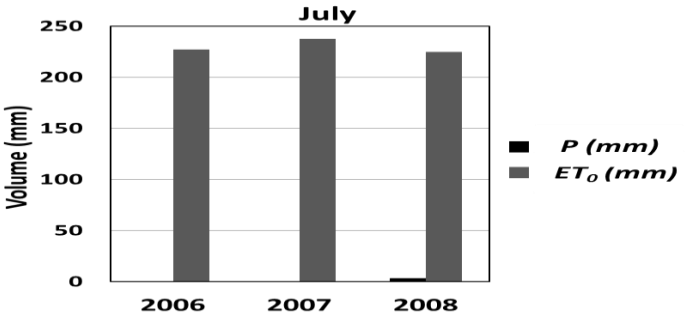

Figure 5.16: Precipitation (P) and reference evapotranspiration (ET_0) in July 2006, 2007 and 2008.

Similarly to July, August was characterized by very high evaporative demand and irrelevant rainfall (Figure 5.18). Even in this case, *ET* volumes estimated by SEBAL were, in general, lower than the corresponding delivered to hydrants, and good correlations between data were obtained with R^2 values of approximately 0.85, 0.82 and 0.75 for August 2006, 2007 and 2008 respectively.

Similar trends were observed during the three years even in September (fig. 5.19), in which *ET* volumes estimated by SEBAL resulted lower than the corresponding delivered by hydrants. Good correlations between data were obtained, as shown in figure 5.19, with R^2 values of approximately 0.75, 0.85 and 0.75 for the three years. Figure 5.20 shows the Precipitation (*P*) and reference evapotranspiration (ET_0) in September 2006, 2007 and 2008.

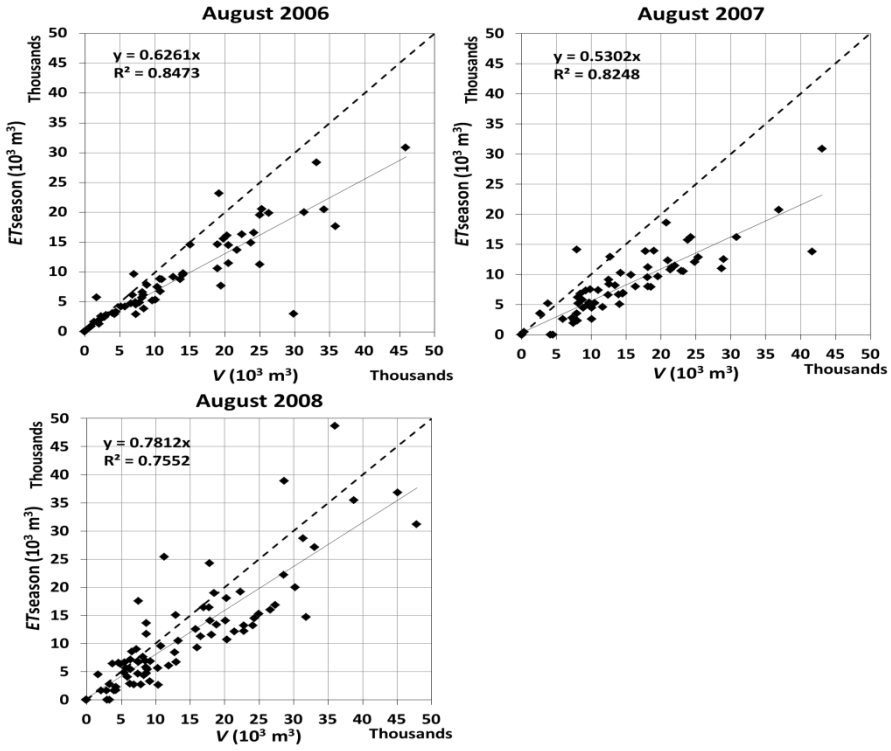

Figure 5.17: Monthly evapotranspiration volumes estimated by SEBAL model vs. water volumes delivered to hydrants in August 2006, 2007 and 2008.

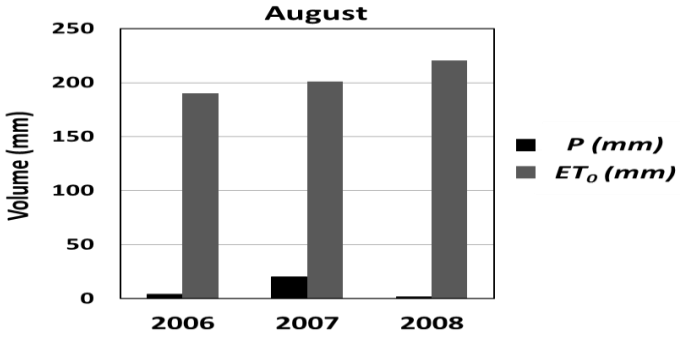

Figure 5.18: Precipitation (P) and reference evapotranspiration (ET_0) in August 2006, 2007 and 2008.

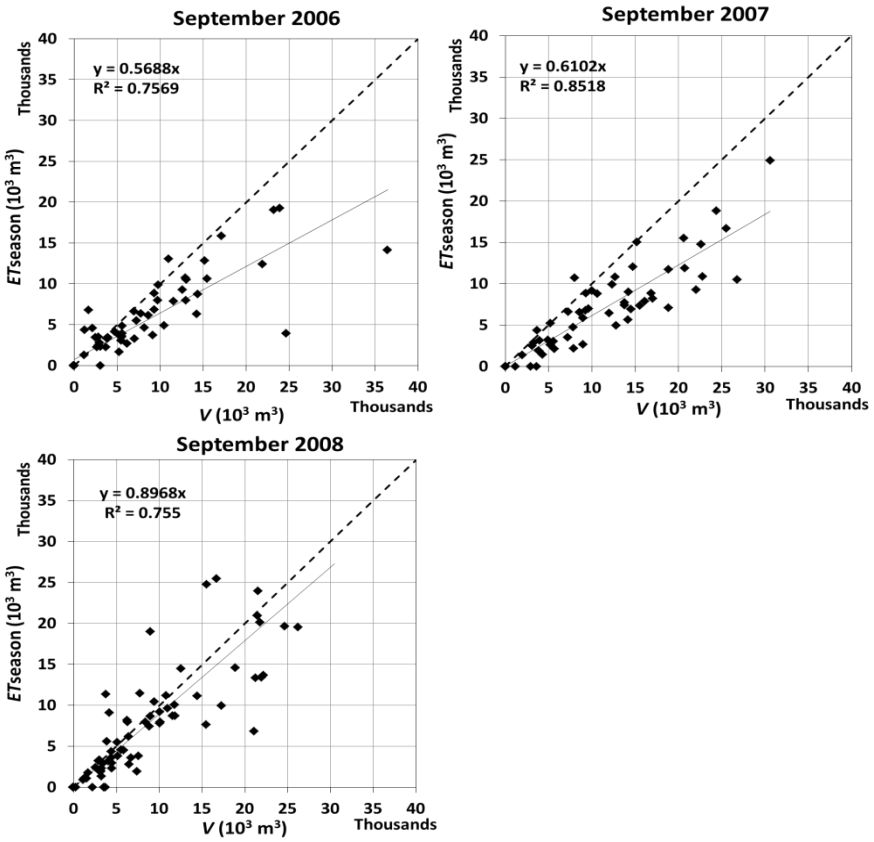

Figure 5.19: Monthly evapotranspiration volumes estimated by SEBAL model vs. water volumes delivered to hydrants in September 2006, 2007 and 2008.

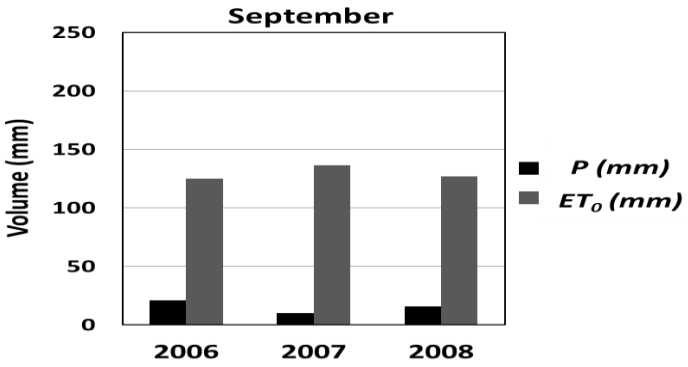

Figure 5.20: Precipitation (P) and reference evapotranspiration (ET_0) in September 2006, 2007 and 2008.

When analyzing the data at monthly time-scale, it is evident that in general farmers, due to the absence of rainfall and the high evapotranspiration demand of atmosphere, tended to supply irrigation volumes higher than the actual crop requirement.

This circumstance is even more manifest after aggregating the data of the three years at seasonal temporal scale and hydrant level (figures 5.21, 5.22 and 5.23). As can be observed, during irrigation seasons 2006 and 2007 the results were quite similar. In both years, two main groups of hydrants can be noticed. The first group (inside the red dashed lines) is represented by hydrants that delivered seasonal water volumes similar to the corresponding seasonal *ET* estimated by SEBAL. On the other hand, the second group, containing most of the data, is characterized by those hydrants that delivered water volumes higher than the corresponding *ET*. This can be due to farmers' irrigation practices and can be considered an indicator to categorize on-farm irrigation efficiency. In both irrigation seasons (2006 and 2007) few hydrants used water from hydrants for applications different than irrigation, which explain the most significant differences between seasonal *ET* estimated by SEBAL and water volume delivered to those hydrants. Both the irrigation seasons showed a quite high coefficient of determination, approximately of 0.87 and 0.83, which indicates a strong linear relationship between the considered variables.

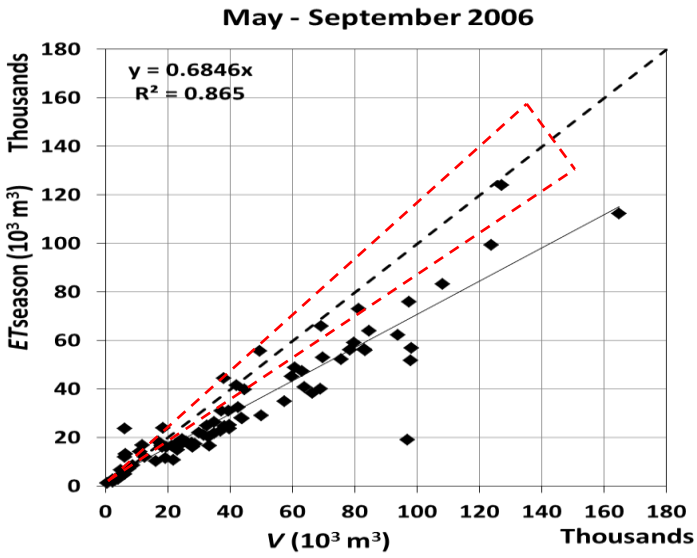

Figure5.21: Seasonal *ET* estimated by SEBAL vs. water volumes delivered to hydrants during irrigation season 2006.

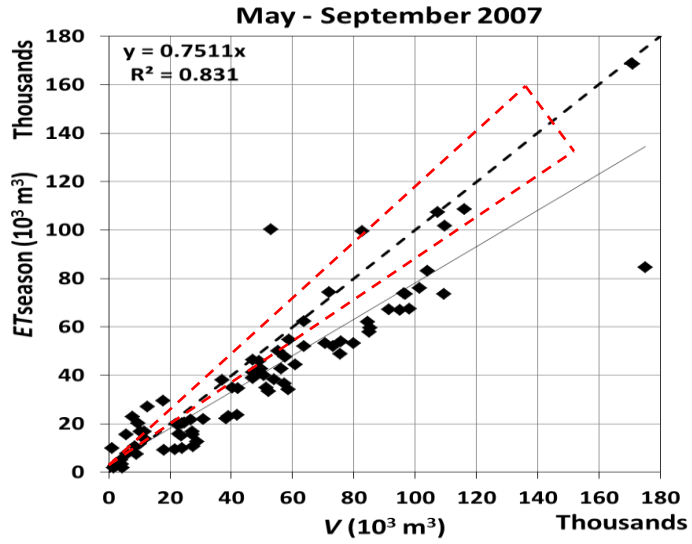

Figure 5.22: Seasonal *ET* estimated by SEBAL vs. water volumes delivered to hydrants during irrigation season 2007.

On the other hand, in 2008, cumulated seasonal ET estimated by SEBAL model resulted on average slightly lower than the total season volumes delivered to hydrants. However, when compared to irrigation seasons 2006 and 2007, the differences between the estimated volumes and the corresponding delivered to hydrants were lower, due to the copious amount of precipitation characterizing all irrigation season, which corresponded approximately to 250 mm.

According to the rainfall occurred in irrigation season 2008, farmers tended therefore to reduce irrigation water supply. The fact that a fraction of precipitation has been used by the plant in the evapotranspiration process reduced the differences between the model estimates and the measured volumes. For irrigation season 2008 the data were characterized by a linear relationship with a coefficient of determination R^2 of about 0.83 (figure 5.23).

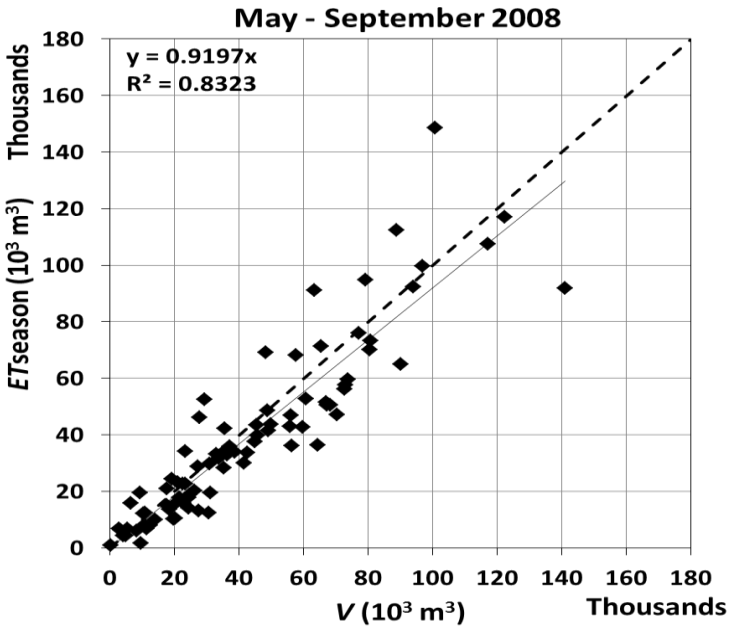

Figure 5.23: Seasonal *ET* estimated by SEBAL vs. water volumes delivered to hydrants during irrigation season 2008.

5.3 Water and Energy tradeoff and savings

At hydrant level, SEBAL *ET* estimates were aggregated to obtain the monthly evapotranspiration volumes ($ET_{monthly}$) in the whole irrigation district that were compared to measured monthly water consumption($V_{monthly}$). Figures 5.24, 5.25 and 5.26 show, for the three years and for the whole district, the comparison between monthly *ET* volumes estimated by SEBAL and actual water volumes distributed by hydrants.

As shown in figure 5.24 for irrigation season 2006, it was verified that a significant amount of water could have been saved by following SEBAL estimations, especially in the driest months, when precipitations were absent or negligible. In May, June and September it was observed that the amount of water that could have been saved was quite limited, because of rainfall events occurred in those periods. It is important to highlight that SEBAL model accounts for a fraction of precipitation used by vegetation to increase actual transpiration fluxes. However, this volume is not taken into account in water consumption measurements downstream hydrants. This can lead to decrease the difference between the model estimates and the measured water consumption, especially in months with significant rainfall and low evaporative demand.

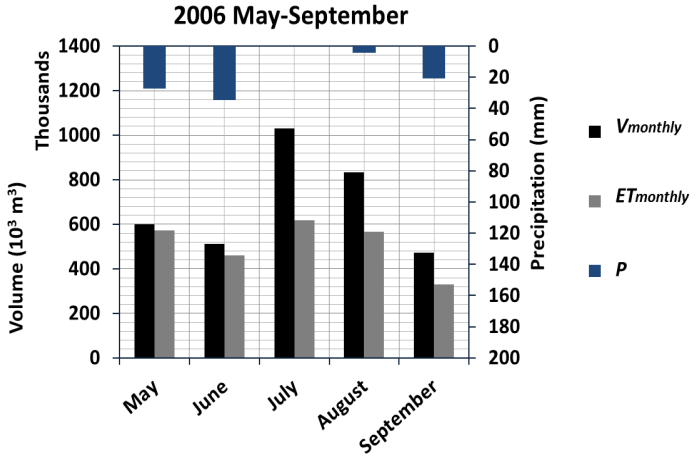

Figure 5.24: Monthly distribution of *ET* volumes estimated by SEBAL and water consumption in the district during irrigation season 2006. Monthly Precipitation is also indicated in the secondary axis.

Similar results were obtained in 2007 when, with the exception of May, significant volumes of water could have been saved if irrigation managers had accounted for model estimates of actual *ET*. Regarding the month of May, the low evaporative demand, the significant amount of precipitation and the consequential presence of water stored in the soil, determined reduced water consume. Figure 5.25 shows that the highest water saving could have been achieved during the periods of peak water demand (July and August).

A considerable amount of water could have been saved in July and August even in 2008 (figure 5.26). It was observed that in May, water consumption was lower than the model estimated, due to the copious precipitations and the relatively low evaporative demand (figure 5.12). In June, despite the occurrence of abundant rainfall, the highest amount compared to the other months of the season, water distributed by hydrants resulted lower than actual *ET* estimated by SEBAL; this was due to the circumstance that precipitations was recorded in only two consecutive events (8 and 9 June) characterized by relatively high intensity, during which only a restricted fraction was infiltrated into the soil, thus limiting crop water uptake.

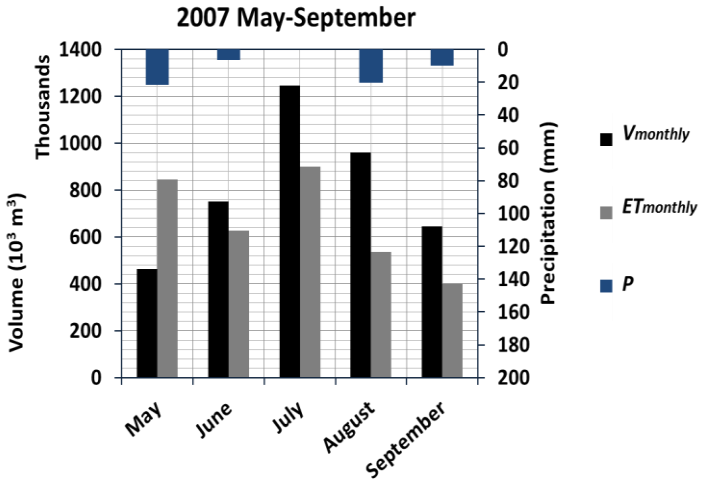

Figure 5.25: Monthly distribution of *ET* volumes estimated by SEBAL and water consumption in the district during irrigation season 2007. Monthly Precipitation is also indicated in the secondary axis.

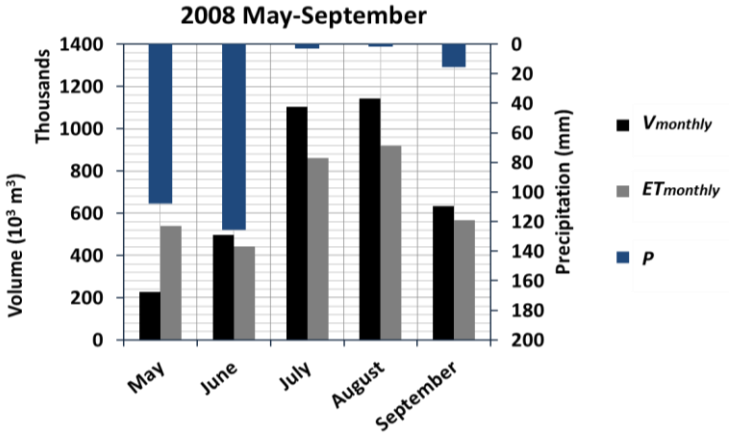

Figure 5.26: Monthly distribution of *ET* volumes estimated by SEBAL and water consumption in the district during irrigation season 2008. Monthly Precipitation is also indicated in the secondary axis.

Assuming SEBAL estimations as a reference, it is evident that farmers apply excessive amounts of water. The comparative analysis at district level showed that seasonal volumes estimated by SEBAL model are lower than those distributed by hydrants, which opened a great potential for water saving. The numerical values of monthly measured water consumption and the corresponding estimated by SEBAL, for the three years, is shown in table 5.4.

As can be observed, substantial water saving could have been achieved in the district that, on a seasonal basis and for the three years, corresponds to 26.2, 28.0 and 16. 4% of total water consumption.

Table 5.8: Volumes of water distributed by hydrants and corresponding estimated by SEBAL model.

	Water distributed by hydrants (m^3)			**SEBAL estimated ET (m^3)**		
	2006	**2007**	**2008**	**2006**	**2007**	**2008**
May	600311	462044	226405	571895	844733	540624
June	513383	750507	497491	460530	628179	443077
July	1031859	1247093	1104688	617128	900099	860621
August	833917	959868	1142649	567831	536378	917586
September	472001	645392	633981	330851	398945	565343

For each month of the examined seasons, table 5.5 summarizes the electrical energy consumed in the whole district, as provided from irrigation managers.

Table 5.9: Total electrical energy consumed in the irrigation district (kWh).

Energy Invoice (kWh)			
	2006	**2007**	**2008**
May	190507	148063	69653
June	157673	235345	153907
July	314025	373121	361867
August	251995	289338	380517
September	143867	186374	175850

Based on SEBAL recommendations and considering the potential water saving that could have been achieved a considerable amount of energy could also have been saved in the pumping station. Following SEBAL estimations, therefore, the district could have a great potential even for energy saving, with percentage theoretically similar to those corresponding to irrigation volumes. Table 5.6 shows the potential amount of water and energy saving per hectare of irrigated surface.

Table 5.10: Potential of water and energy saving per hectare of irrigated area

	Water saving (m^3 ha^{-1})			**Energy saving (kWh ha^{-1})**		
	2006	**2007**	**2008**	**2006**	**2007**	**2008**
May	46.6	0.0	0.0	13.9	0.0	0.0
June	86.8	189.4	86.1	25.3	57.2	26.3
July	680.7	537.2	386.2	196.0	156.7	124.2
August	436.7	655.6	356.1	123.9	191.2	115.9
September	231.7	381.5	108.6	66.1	106.5	29.0
Seasonal	1482.5	1763.7	937.0	425.2	511.6	295.4

5.4 Application of SEBAL model in the District 1/A, Castelvetrano, Italy

In this section, results of the application of SEBAL model in the district 1/A of ‘‘Consorzio di Bonifica di Agrigento 3’’ is reported. Firstly, Landsat 5 TM images were pre-processed to produce maps describing the spatial distribution of surface albedo, NDVI, canopy height and land surface radiometric temperature. Outputs obtained from initial pre-processing, joint with some ancillary data retrieved from the meteorological weather station, were then implemented in the model for the examined case study. This application provided a direct estimation of instantaneous energy fluxes at the moment of satellite image acquisition. Then, the model used the evaporative fraction and the self-preservation hypothesis to upscale the instantaneous latent heat flux into daily evapotranspiration.

The model output was represented by maps describing the spatial distribution of actual evapotranspiration at the acquisition day. Finally, reference evapotranspiration estimated based on the measured weather variables was used as integration factor to estimate actual evapotranspiration over longer time intervals.

The model was applied to the agricultural district 1/A for irrigation seasons (from May to September) 2009 and 2010.

The cloud coverage of satellite images was a drawback in the model application in this case study; in fact, only 7 Landsat TM images were used to cover both investigated irrigation seasons. Subset images over the district 1/A were prepared and processed in order to produce a layered spectral band image, required to apply the surface energy balance model. In the following paragraphs, the maps of input data are shown, as well as the instantaneous fluxes and the daily surface evapotranspiration retrieved after SEBAL model application. Even if the model was applied to all available images, acquisitions on 25th July 2009 (DOY 206) and on 12th July 2010 (DOY 193) are used as examples to present model application and achieved results.

5.4.1 Surface albedo

The broadband shortwave surface albedo ranged between a minimum of 0 and a maximum of approximately 0.42, obtained on 25th July 2009. On the other image, on 12th July 2010 values of α ranged between a minimum of 0.07 and a maximum of 0.47. For the two examined days, figures 5.27 and 5.28 show the spatial distributions of surface albedo, as well as the corresponding histograms and the main statistic parameters.

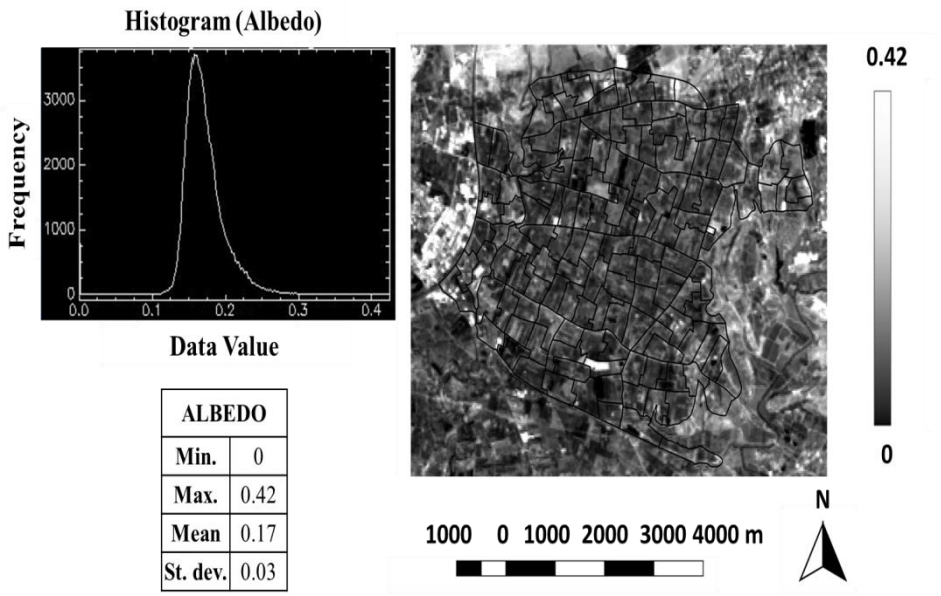

ALBEDO	
Min.	0
Max.	0.42
Mean	0.17
St. dev.	0.03

Figure 5.27: Spatial distribution of surface albedo, histogram and statistics (image acquired on DOY 206 in 2009).

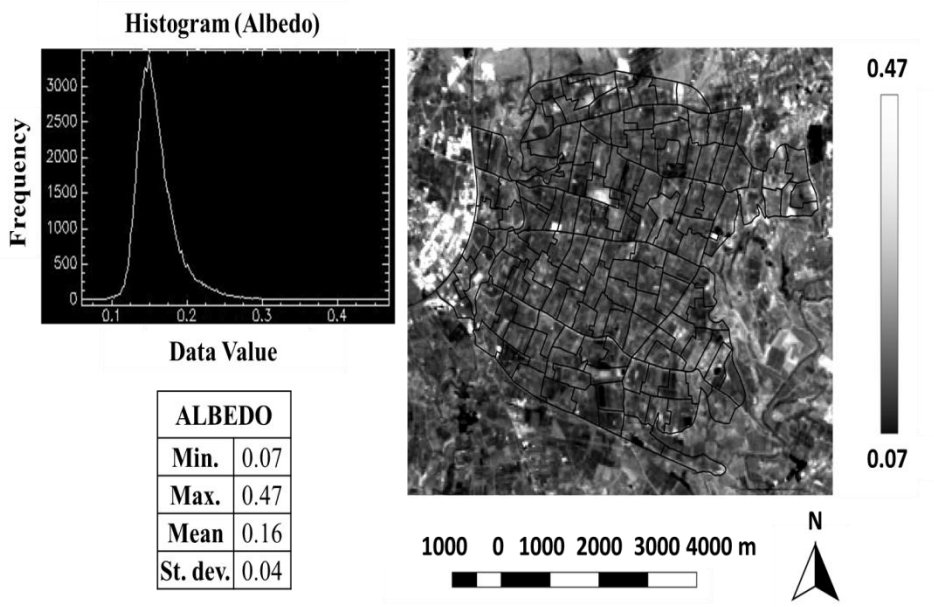

Figure 5.28 Spatial distribution of surface albedo, histogram, and statistics (image acquired on DOY 193 in 2010).

5.4.2 Normalized Difference Vegetation Index

On DOY 206 (2009), NDVI values ranged between a minimum of 0 and a maximum of approximately 0.82. Similarly, on DOY 193 (2010), NDVI values ranged between a minimum of 0 and a maximum of 0.81.

Relatively high NDVI (> 0.7) allowed detecting regions with dense vegetation. On the contrary, low NDVI values are indicative of bare soil pixels. Figures 5.29 and 5.30 show the NDVI spatial distribution, as well as the corresponding histograms and main statistics obtained respectively on DOY 206 in 2009 and on DOY 193 in 2010.

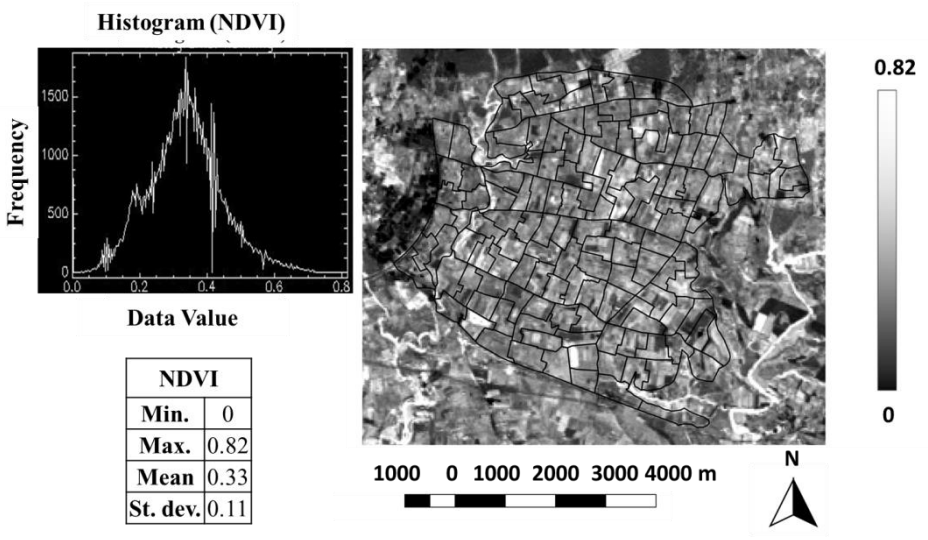

NDVI	
Min.	0
Max.	0.82
Mean	0.33
St. dev.	0.11

Figure 5.29: Spatial distribution of NDVI, histogram and statistics (image acquired on DOY 206 in 2009).

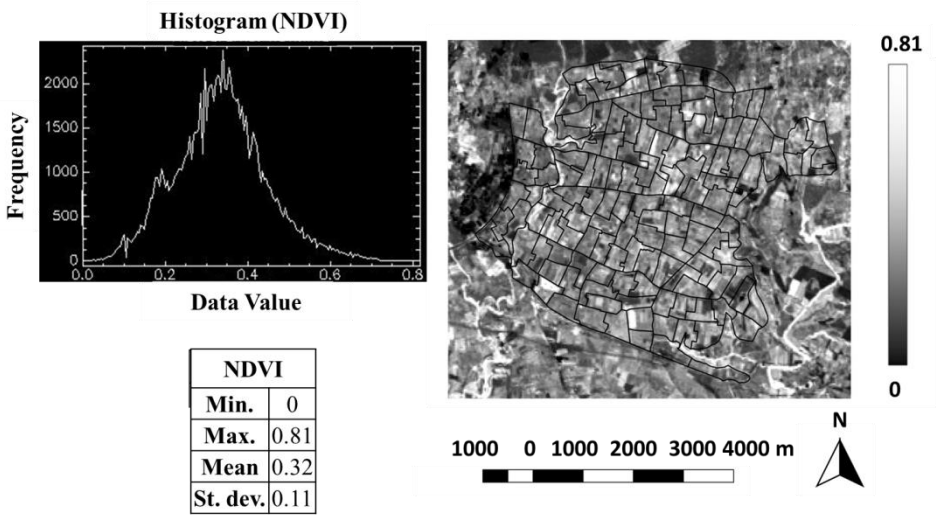

NDVI	
Min.	0
Max.	0.81
Mean	0.32
St. dev.	0.11

Figure 5.30: Spatial distribution of NDVI, histogram and statistics (image acquired on DOY 193 in 2010).

5.4.3 Net radiation

In the district 1A, in 2009 net radiation ranged between a minimum value of about 130.2 Wm^{-2} and a maximum of about 768 Wm^{-2} (DOY 206), whereas in 2010 minimum and maximum values resulted approximately equal to 133 and 788 Wm^{-2} (DOY 193).

For both the examined scenes, figures 5.31 and 5.32 show the spatial distributions of net radiation, as well as the corresponding histograms and the statistic parameters.

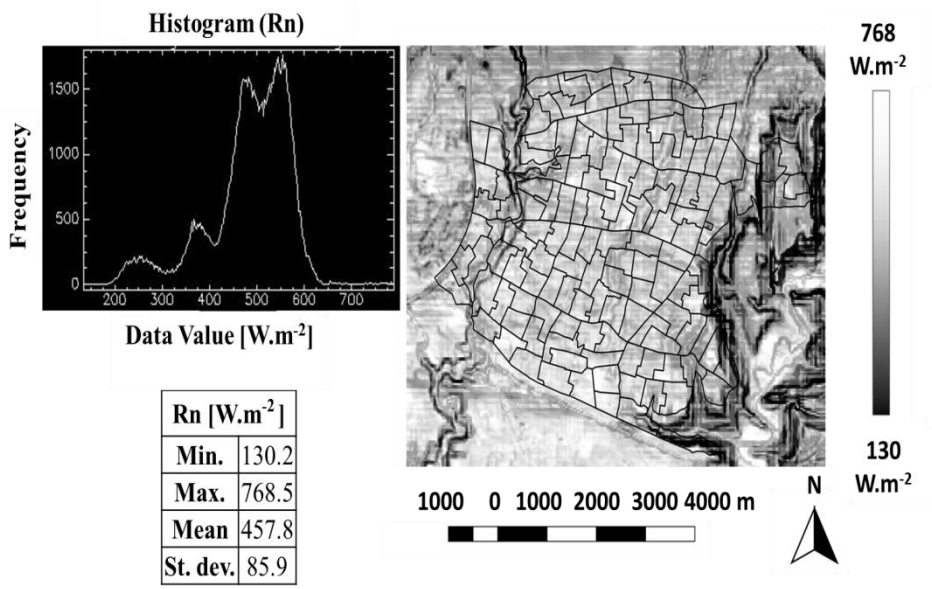

Rn [W.m^{-2}]	
Min.	130.2
Max.	768.5
Mean	457.8
St. dev.	85.9

Figure 5.31: Spatial distribution of R_n, histogram and statistics (image acquired on DOY 206 in 2009).

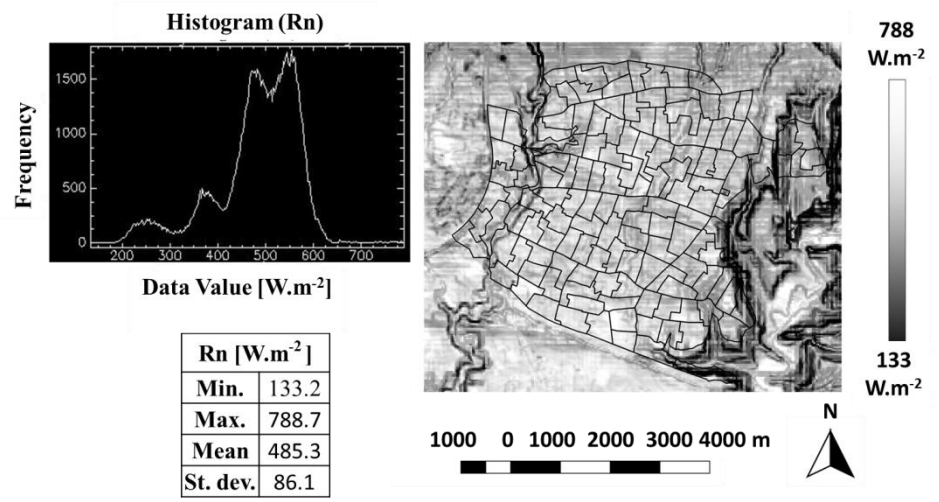

Rn [W.m^{-2}]	
Min.	133.2
Max.	788.7
Mean	485.3
St. dev.	86.1

Figure 5.32: Spatial distribution of R_n, histogram and statistics (image acquired on DOY 193 in 2010).

5.4.4 Soil heat flux

The near mid-day heat flux in the ground was estimated as a fraction of the total net radiation based on the values of NDVI, surface radiometric temperature and surface albedo. As mentioned in the theoretical background it was shown by Liang, (2004b) that G_0 values can range between 5% of total net radiation under full canopy cov**er and about 50% of total net radiation for dry bare soils. Areas characterized** by low albedo and low NDVI (e.g., bare dry soils) absorb more energy from incoming solar radiation, which yields higher G_0 values.

G_0 ranged between a minimum value of about 37.0 Wm^{-2} and a maximum of about 140.0 Wm^{-2} on DOY 206 (2009) and also from a minimum of about 26.5 Wm^{-2} and a maximum of about 120.0 Wm^{-2} on DOY 193 (2010).

As expected, G_0 showed to be greater in bare soils than in cultivated areas. The spatial distributions of G_0, as well as the corresponding histograms and the related statistic parameters on both the examined scenes, are shown respectively in figures 5.33 and 5.34.

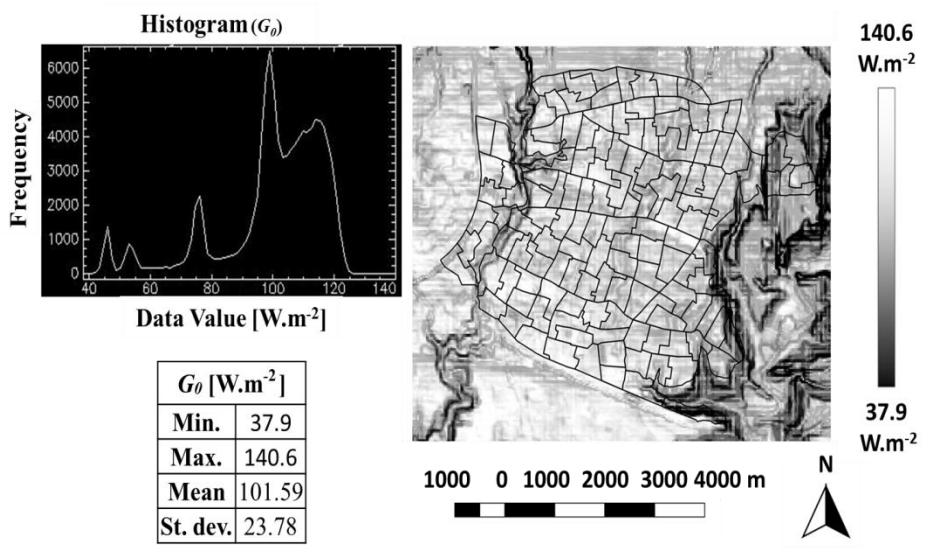

G_0 [W.m^{-2}]	
Min.	37.9
Max.	140.6
Mean	101.59
St. dev.	23.78

Figure 5.33: Spatial distribution of G_0, histogram, and statistics obtained for an image acquired on DOY 206 in 2009.

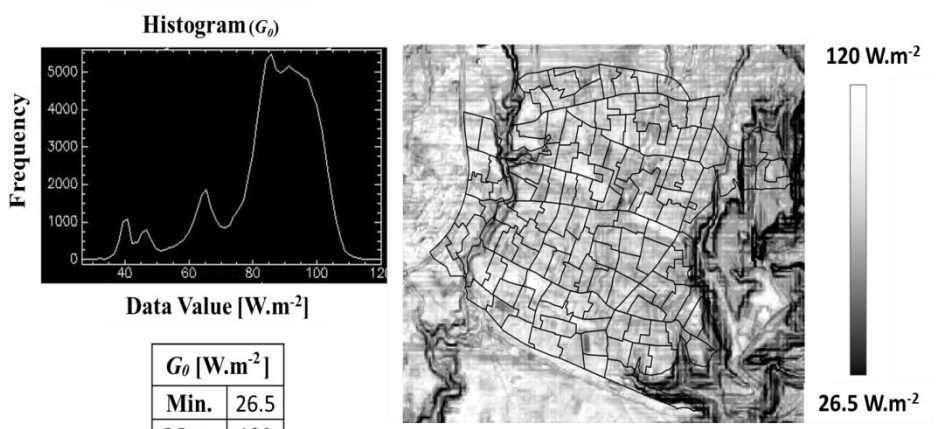

G_0 [W.m^{-2}]	
Min.	26.5
Max.	120
Mean	86.58
St. dev.	23.4

Figure 5.34: Spatial distribution of G_0, histogram, and statistics obtained for the image acquired on DOY 193 in 2010.

5.4.5 Sensible heat flux

Under a certain gradient of temperature (ΔT), sensible heat flux (H) is transferred from soil surface to the overlying atmosphere. SEBAL uses this gradient of temperature to estimate H in the whole image scene, by assuming a linear correlation between ΔT and the surface radiometric temperature (T_{rad}). Firstly, the sensible heat flux was estimated by SEBAL under atmospheric stable condition and then the correct estimations of sensible heat flux were retrieved by applying the corrections for atmospheric stability, for both stable and unstable conditions, by using the Monin-Obukhov length (L).

Values of sensible heat flux ranged between a minimum close to 0.0 Wm^{-2} and a maximum of about 598 Wm^{-2} on DOY 206 (2009); on DOY 193 in 2010, minimum and maximum values resulted respectively of 0.0 and about 736.3 Wm^{-2}. Vegetated areas showed relatively low values of sensible heat flux, especially under intensively irrigated vegetation, where energy is mainly used for evapotranspiration processes. On the contrary, bare soils showed high H values. The spatial distributions of H, as well as the corresponding histograms and the statistic parameters on both investigated scenes, are shown in figures 5.35 and 5.36.

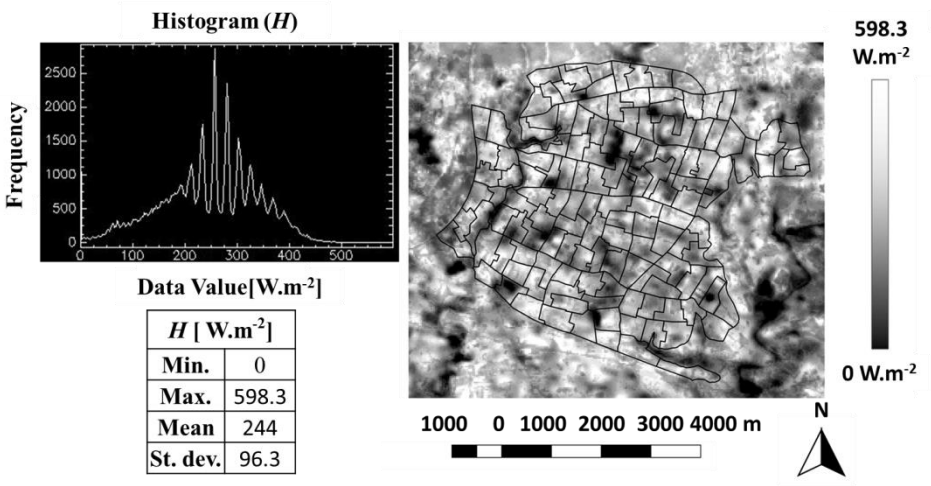

H [$W.m^{-2}$]	
Min.	0
Max.	598.3
Mean	244
St. dev.	96.3

Figure 5.35:Spatial distribution of *H*, histogram, and statistics obtained for the image acquired on DOY 206 in 2009.

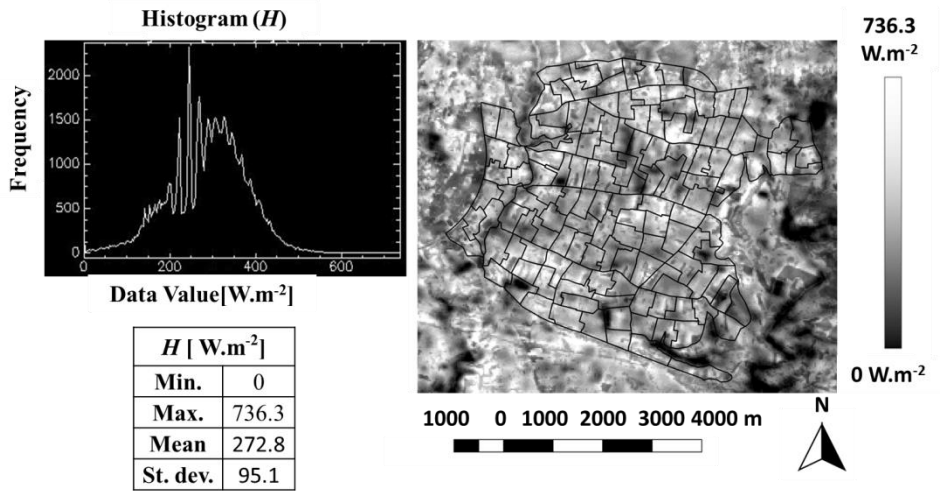

H [W.m^{-2}]	
Min.	0
Max.	736.3
Mean	272.8
St. dev.	95.1

Figure 5.36: Spatial distribution of *H*, histogram and statistics obtained for the image acquired on DOY 193 in 2010.

5.4.6 Instantaneous latent heat flux

Remote sensing cannot give a direct measurement of the energy allocated for evapotranspiration since it requires knowing the surface humidity and the soil moisture content. However, the latent heat flux can be retrieved by remote sensing techniques as a residue from the energy budget. The retrieved instantaneous net radiation, soil heat flux and sensible heat flux allowed then to obtain the spatial distribution of instantaneous λET over the image scene. In this perspective, the latent heat flux obtained by RS techniques describes real conditions at image acquisition time.

Application of SEBAL evaluated instantaneous latent heat flux values ranging between a minimum of 0.0 Wm^{-2} and a maximum of 700 Wm^{-2} on DOY 206 in 2009 and between 0.0 Wm^{-2} and 585 Wm^{-2} on DOY 193 in 2010. Low λET values were associated to bare soils, being high values associated to cultivated areas.

Figure 5.37 and 5.38 show the spatial distributions of λET retrieved by SEBAL model, the corresponding histograms and the main statistics obtained for both the examined acquisition dates.

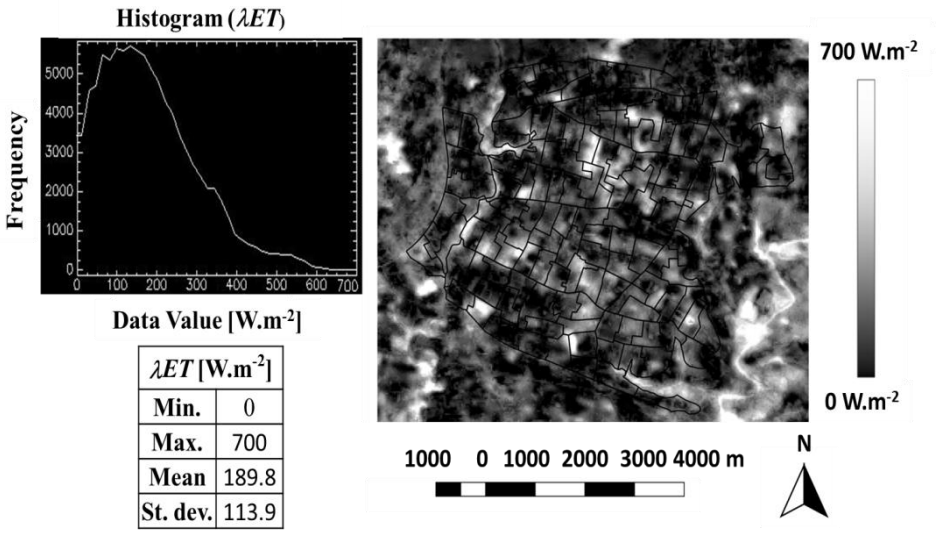

λET [W.m^{-2}]	
Min.	0
Max.	700
Mean	189.8
St. dev.	113.9

Figure 5.37: Spatial distribution of *λET*, histogram and statistics obtained for the image acquired on DOY 206 in 2009.

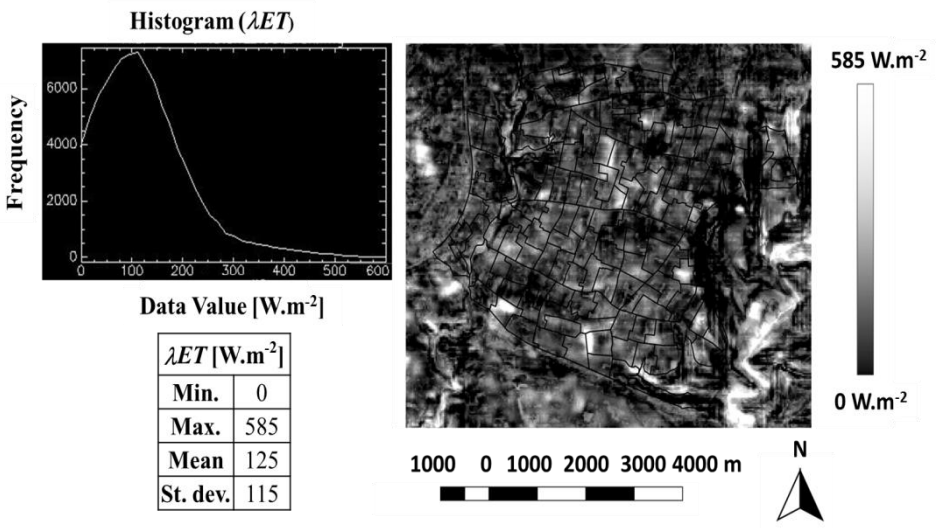

λET [W.m^{-2}]	
Min.	0
Max.	585
Mean	125
St. dev.	115

Figure 5.38: Spatial distribution of *λET*, histogram and statistic parameters obtained for the image acquired on DOY 193 in 2010.

5.4.7 Evaporative fraction

SEBAL model evaluates the evaporative fraction (Λ) as the ratio between actual latent heat flux and available energy, corresponding to R_n-G_0. The evaporative fraction has a range of variability between a minimum of zero and a maximum of 1.0. The latter value indicates zones in which evapotranspiration is absent and all the energy is converted into sensible heat. On the contrary, the maximum value indicates zones of maximum evapotranspiration, in which all the energy is converted into latent heat. This means that for each pixel, Λ represents an indicator of energy partitioning. A pixel with Λ significantly lower than one indicates that *ET* does not occur at maximum rate due to the contribution of the non-vegetated area, to water stress or the simultaneous occurrence of both factors.

The spatial distribution maps of an evaporative fraction, the related histograms and statistics for both the considered scenes are shown in figures 5.39 and 5.40. By observing these figures it is possible to distinguish pixels with vegetated areas, characterized by high values of *Λ* from pixels representing bare soils, with low values of the evaporative fraction.

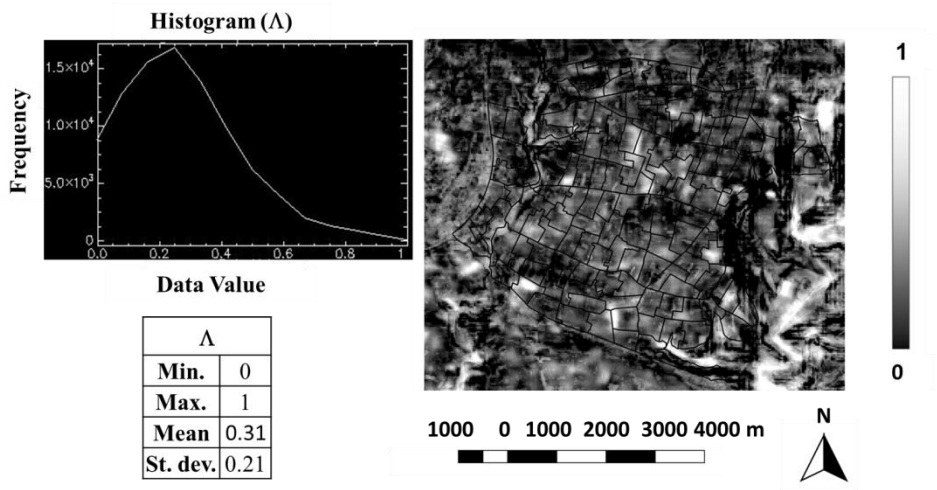

Λ	
Min.	0
Max.	1
Mean	0.31
St. dev.	0.21

Figure 5.39: Spatial distribution of the evaporative fraction, histogram and statistics obtained for the image acquired on DOY 206 in 2009.

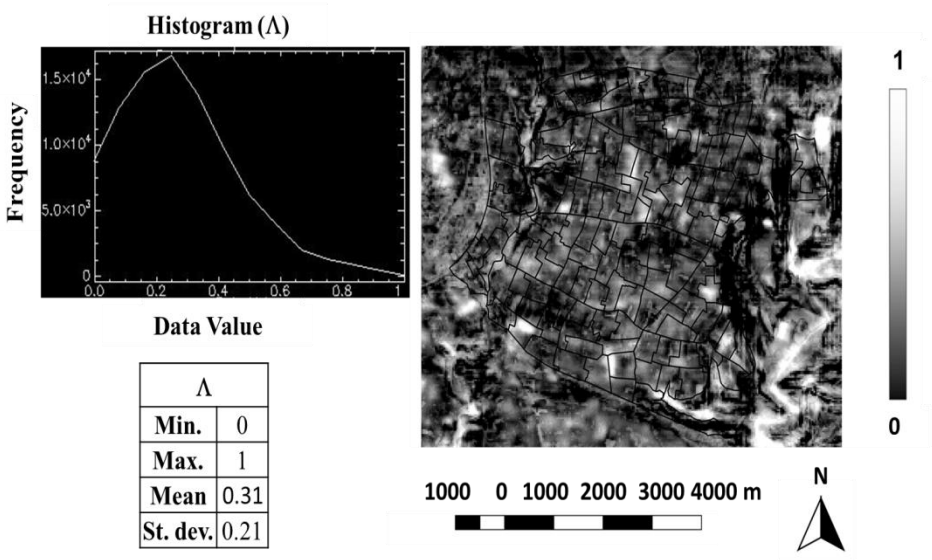

Figure 5.40: Spatial distribution of the evaporative fraction, histogram and statistics obtained for the image acquired on DOY 193 in 2010.

5.4.8 Daily net radiation, R_{n24}

SEBAL uses the FAO-56 (Allen et al., 1998) procedure to estimate daily net radiation, R_{n24}. This estimation is mandatory since Rn_{24} is used in upscaling instantaneous latent heat flux into daily values.

On DOY 206 in 2009, R_{n24} achieved a maximum value of about 22.9 $MJm^{-2}d^{-1}$ and a minimum of 10.17 $MJm^{-2}d^{-1}$, with average of 17 $MJm^{-2}d^{-1}$. On DOY 193 in 2010, instead, R_{n24} retrieved a maximum of about 11.8 $MJm^{-2}d^{-1}$ and a minimum of 25.76 $MJm^{-2}d^{-}1$, with average of 20.76 $MJm^{-2}d^{-1}$.

The spatial distribution maps of R_{n24}, the corresponding histograms and the main statistic parameters for both the considered scenes are presented in figures 5.41 and 5.42.

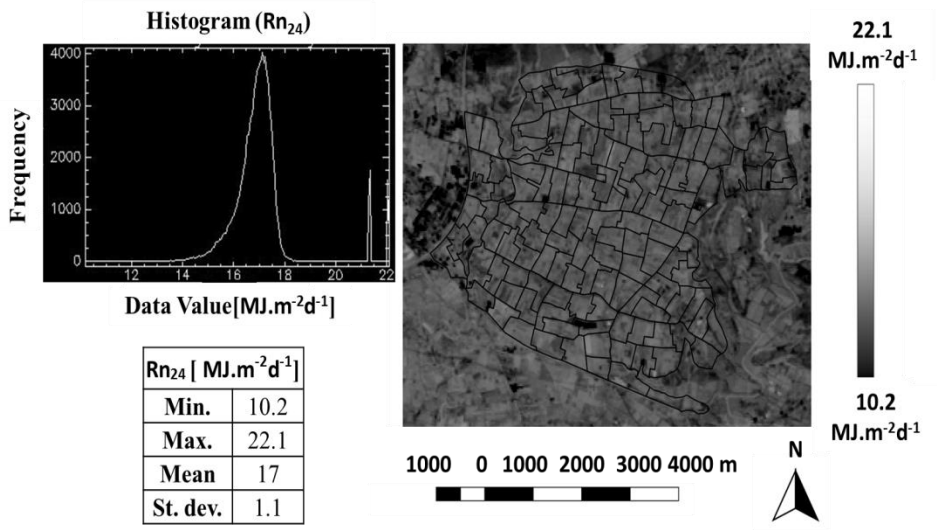

Rn_{24} [MJ.m^{-2}d^{-1}]	
Min.	10.2
Max.	22.1
Mean	17
St. dev.	1.1

Figure 5.41: Spatial distribution of R_{n24}, histogram and statistics obtained for the image acquired on DOY 206 in 2009.

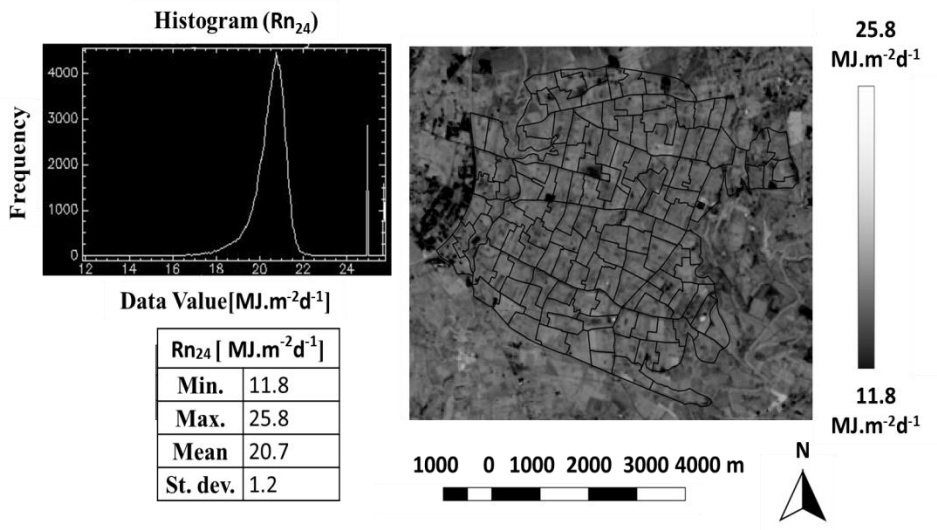

Rn_{24} [MJ.m^{-2}d^{-1}]	
Min.	11.8
Max.	25.8
Mean	20.7
St. dev.	1.2

Figure 5.42: Spatial distribution of R_{n24}, histogram and statistics obtained for the image acquired on DOY 193 in 2010.

5.4.9 Daily Evapotranspiration

Under the self-preservation hypothesis, SEBAL uses the evaporative fraction to upscale instantaneous latent heat flux into daily *ET* values. The retrieved R_{n24} and Λ were used to obtain the actual evapotranspiration $ET_{a,ID}$ (mm) at the image acquisition days. The energy fluxes were then converted into evaporated water mass.

Application of the model allowed evaluating $ET_{a,ID}$ values ranging between a minimum of 0.0 and a maximum of 8.0 mm for both the scenes representing DOY 206 and 193. However, the average value of $ET_{a,ID}$ was different, assuming a mean value of 2.48 mm on DOY 206 (2009) and of 1.57 mm on DOY 193 (2010).

Low $ET_{a,ID}$ values were associated to bare soils, being high values associated to cultivated areas. Figure 5.43 and 5.44 shows the spatial distributions of $ET_{a,ID}$ retrieved by SEBAL model, the related histograms and the main statistic parameters evaluated on both the represented acquisition dates.

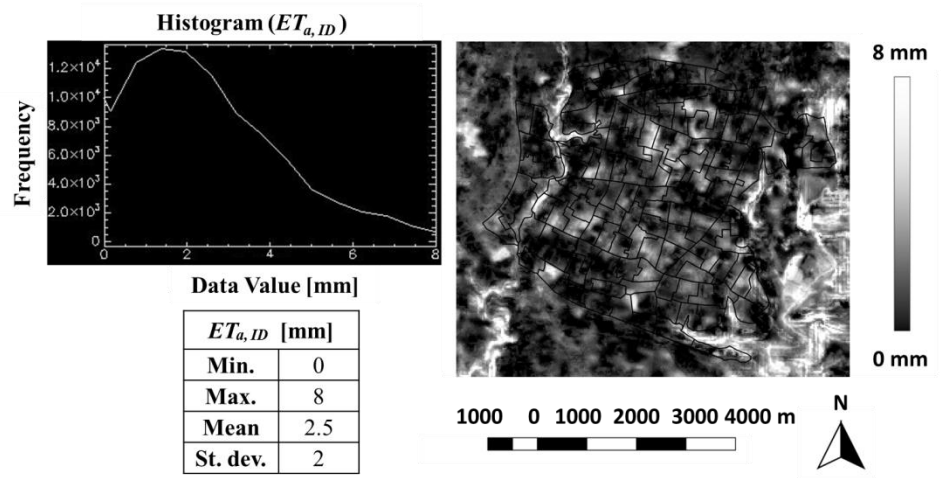

$ET_{a,ID}$ [mm]	
Min.	0
Max.	8
Mean	2.5
St. dev.	2

Figure 5.43: Spatial distribution of $ET_{a,ID}$, histogram and statistics obtained for the image acquired on DOY 206 in 2009.

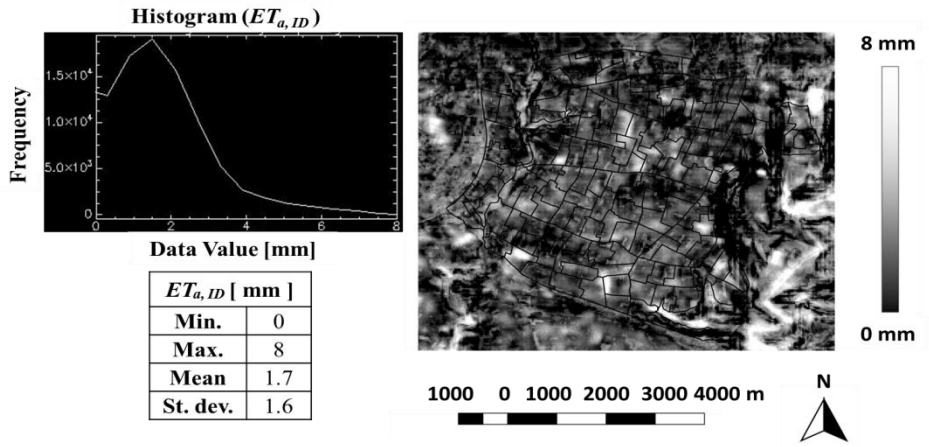

$ET_{a, ID}$ [mm]	
Min.	0
Max.	8
Mean	1.7
St. dev.	1.6

Figure 5.44: Spatial distribution of $ET_{a,ID}$, histogram and statistics obtained for the image acquired on DOY 193 in 2010.

5.5 Application of TSEB model in the District 1/A

Despite a two-source surface energy balance model, TSEB, was applied on the district 1/A case study, detailed application results will be not presented due low accuracy under-estimations of sensible heat flux, with consequent overestimation of latent heat flux.

The TSEB model has theoretically the advantage of dealing with vegetation and soil as different energy transfer components. This implicates that in areas characterized by sparse vegetation, as the case of district 1/A the TSEB model is preferred. It was initially assumed that application of TSEB should have allowed obtaining better estimates of daily evapotranspiration if compared to SEBAL model. However, due to uncertainties associated with surface radiometric temperatures or due to input parameters defining vegetation geometry, canopy parameters and viewing geometry, it was not possible to improve the estimations of actual evapotranspiration obtained by the two source model.

Figure 5.45 and 5.46 show the comparison between the flux tower cumulated daily evapotranspiration ($ET_{D,EC}$) *vs* TSEB seasonally upscaled daily evapotranspiration ($ET_{D,TSEB}$), as well as with the reference daily evapotranspiration (ET_0). The bar charts in reference to the secondary axis, represents the precipitation events during the considered seasons. The dash lines in the figure indicated the acquisition

day of the used satellite images. It was shown in figure 5.45 and 5.46 that the TSEB retrieved daily evapotranspiration was always overestimated with values very similar to that of the (ET_0). The dashed line in the figures below can show that on acquisition days results were not acceptable, which means that this overestimation was not related to the temporal upscaling approach.

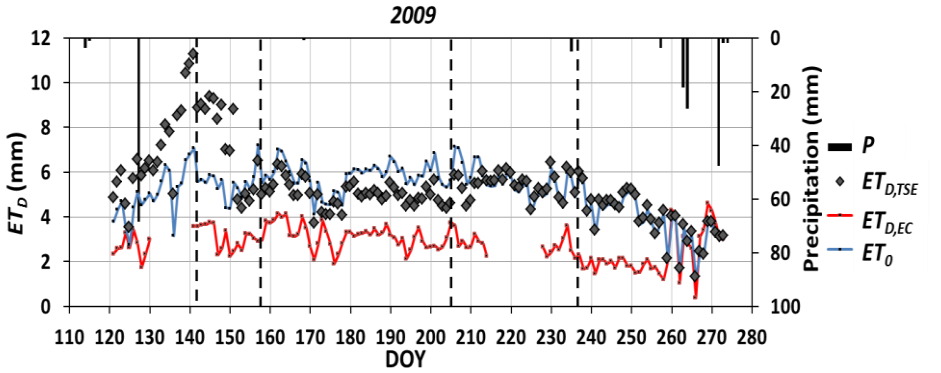

Figure 5.45: The 2009 season temporal distribution of daily *EC* measured evapotranspiration ($ET_{D,EC}$), temporally upscaled $ET_{D,TSEB}$, Precipitation (*P*) and SIAS measured reference evapotranspiration (ET_0) (dashed lines represent image acquisition dates).

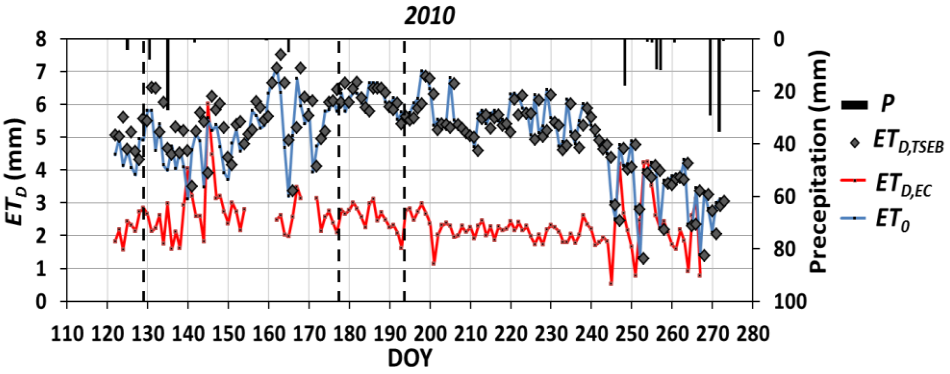

Figure 5.46: The 2010 season temporal distribution of daily *EC* measured evapotranspiration ($ET_{D,EC}$), temporally upscaled $ET_{D,TSEB}$, Precipitation (*P*) and SIAS measured reference evapotranspiration (ET_0) (dashed lines represent image acquisition dates).

One of the main difference between SEBAL and TSEB is the procedure how the models process the surface radiometric temperatures (T_{rad}) retrieved by remotely sensed images, to estimate sensible heat flux. The SEBAL approach assumes that differences between surface and air temperature (ΔT) vary linearly with radiometric temperature (T_{rad}) whose extremes, corresponding to "hot" and cold pixels," can be considered as an "internal" calibration. In SEBAL model, the selection of hot and cold calibration pixels represents the main factor influencing the estimations of sensible heat flux. On the other hands, TSEB model considers T_{rad} as direct input. Choi *et al.* (2009) showed that the TSEB approach is more sensitive to uncertainties in T_{rad}, especially when is used jointly to in-situ air temperature measurements. Norman et al. (2000) showed that in many cases the magnitude of the uncertainties in T_{rad} retrievals can often be comparable with the aerodynamic difference ($T_0 - T_a$) values. In another research, results of the two source model applications showed that uncertainties on the retrieval surface temperature are the main source of errors and have great impact on H estimates (Timmermans et al., 2007). Troufleau et al., (1997), also showed that replacing of the land surface temperature with T_{rad} is generally accepted for dense canopies but this drives to high errors for sparse canopies.

To gain greater insight over the problem, further analysis of TSEB sensitivity to surface temperature obtained from satellite data is recommended and additional efforts have to be done to evaluate the source of errors associated to TSEB applications over the case study.

5.6 Eddy covariance fluxes and diurnal changes of evaporative fraction

The flux tower installed in the case study of the district 1/A allowed the analysis of the surface energy balance components in the days of image acquisition. The energy balance closure was forced, targeting to preserve the Bowen ratio. Figure 5.47 shows the 30 minutes diurnal variation of net radiation R_n, sensible heat flux H, soil heat flux G_0 and latent heat flux. Figure 5.47 shows that both the values of G_0 and R_n are relatively stable and have similar trend during different acquisition days. On the contrary, sensible and latent heat fluxes are turbulent and presented the highest variability.

Variations of evaporative fraction are of great importance when upscaling instantaneous latent heat flux into daily values. Figure 5.48 shows the diurnal patterns of evaporative fraction during the image acquisitions days. The dynamic of Λ was obtained by using the values of the 30 minutes intervals of energy fluxes retrieved by the flux tower (FT). The diurnal variations of Λ allowed to corroborate the self-preservation hypothesis. The diurnal trend of Λ responds to several factors, including the relative magnitude of turbulent heat fluxes (H and λET). Figure 5.48 shows a concave-up shape usually exhibited by Λ.

As shown in the figure, Λ values are almost constant during midday, when they show a low variability. In most of the examined dates, the diurnal pattern of Λ showed a minimum around solar noon and exhibited two peaks, close to sunrise and sunset.

Gentine *et al.* (2011), found that the Λ was almost independent of the major forcing factors, namely incoming solar radiation and wind speed. The daytime self-preservation and shape of Λ is directly linked to the amplitude and the phase differences between the latent and sensible heat fluxes, it is noticed from figures 4.47 and 4.48 that (according to Gentine *et al.*, 2011) when there was no phase differences between LET and H (mainly between 8:00 and 16:00 UTC the evaporative fraction was relatively invariable during the whole daytime. However, a phase difference between both fluxes leads to strong departure from daytime EF self-preservation

The 30 minutes diachronic analysis of ET as $\Lambda(R_{n24}\text{-}G_{024})$ was obtained by the flux tower 30 minutes scaled evaporative fraction (demonstrated in figure 5.48) and the total daily available energy ($R_{n24}–G_{024}$) measured by the flux tower. These daily values obtained by the same approach that SEBAL represents the 30 mines time step diachronic variation in ET_D retrievals based on the self-preservation hypothesis.

Figure 5.49 shows the changes of ET_D (white dots) at time-step of 30 minutes, obtained by upscaling Λ for all the image acquisition days. The evapotranspiration measured by the eddy covariance method on the image acquisition days ($ET_{ID,EC}$) and the corresponding range of variability (±15%) usually accepted. Allen et al. (2011), demonstrated in

fact, that an error of ±15% in remote sensing surface energy balance estimations can be considered acceptable.

As shown in figure 5.49, the dynamic of ET_D obtained as $\Lambda(R_{n24}\text{-}G_{024})$ in the selected days is similar to that measured by the eddy covariance method on the considered day. An exception was the 26^{th} June when a certain variability was observed. Results showed a time window when the self preservation hypothesis can be applied. This window starts at 8.00-10.00 and finished at 14.00-16.00. This analysis showed that Λ upscaling approach overestimated *ETD* before 8:00 UTC and underestimated ET_D *after 16:00* UTC. However, for acquisition times between 9:30 and 10:00, and by considering the acceptable range of variability, the Λ upscaling approach is valid and accepted.

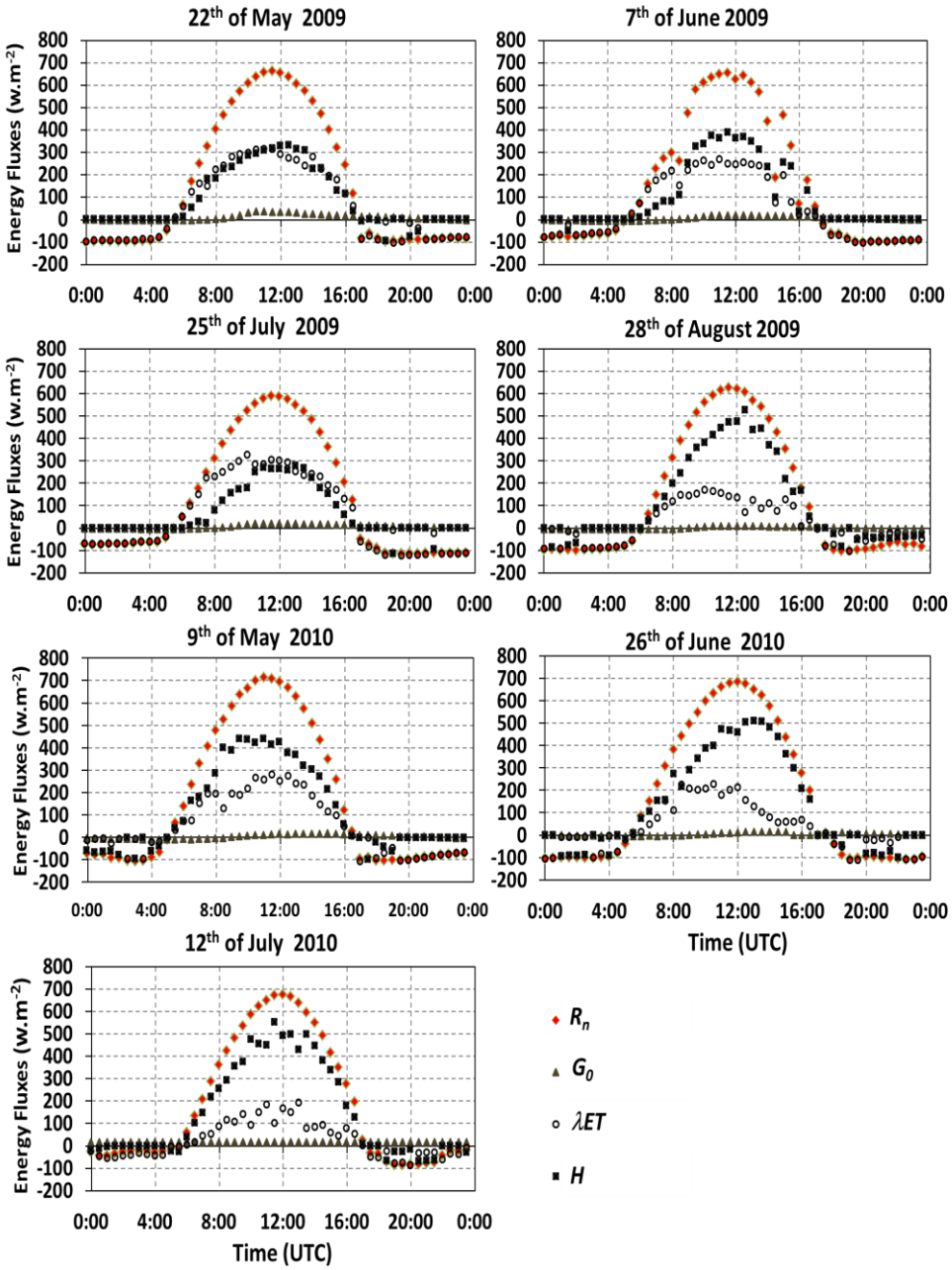

Figure 5.47: Diurnal variation of surface energy balance components during the satellite images acquisition days, in 2009 and 2010.

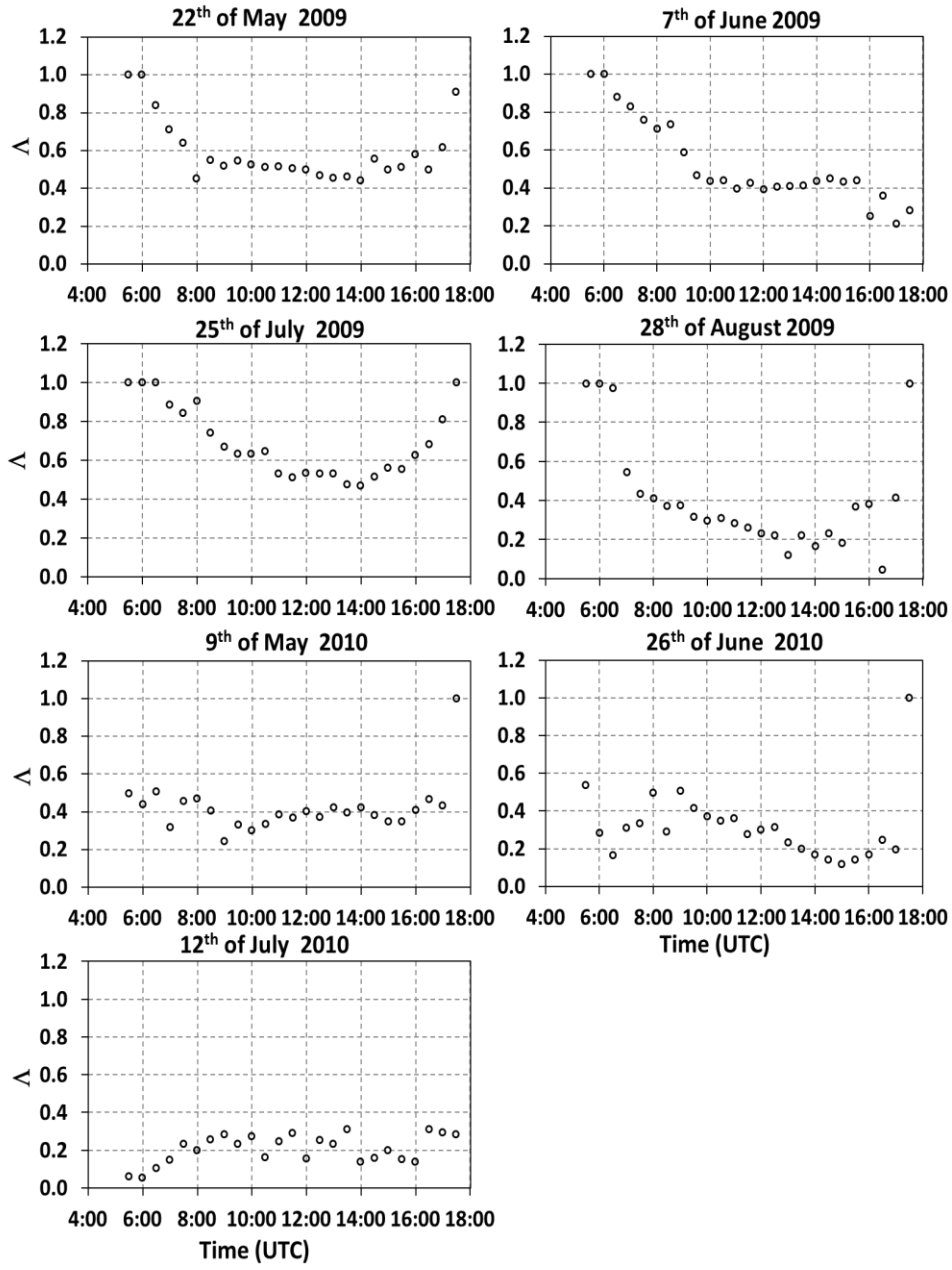

Figure 5.48: Patterns of diurnal Λ during satellite images acquisition days, in 2009 and 2010.

5.6.1 Monthly and seasonal evapotranspiration

In the case study of the consortium of Agrigento (district 1A) as observed from gathered data, irrigation was applied mainly on the 2 peak demand months (July and August). The 2 main cultivated crops in this region (olives and grapevines) are irrigated randomly and under stress conditions. The proposed methodology applied on the Spanish case study is not applicable here. However, the SEBAL retrievals can be valuable in evaluating the state of stress at field level providing indications on farmers practices.

Similar to the previous approach applied on the Spanish case study, the monthly and seasonal evapotranspiration maps were obtained by retrieving ET_D using reference evapotranspiration (ET_0) obtained at SIAS meteorological stations. It was assumed that the actual evapotranspiration $ET_{a,ID}$ estimated by SEBAL model at the image acquisition date changes in reference to ET_0 obtained at the SIAS meteorological station.

Each Landsat TM image was set to represent a period of time in order to cover the peak water demand seasons (May-September) of the years 2009 and 2010, respectively. It was notable that in this area few images were usable due to the cloud coverage which did not allow us to use some images and this added some restrictions to the application.

The fact that the cloud cover reduces the number of usable observations can lead to errors in the estimation of *ET* on seasonal basis, since it was considered that at least 1 image per month is needed to upscale acquisition day actual evapotranspiration ($ET_{a,ID}$) to seasonal *ET* (Allen et al., 2007a).

Allen et al. (2007a) also demonstrated that the lack of satellite image causes an underestimation in *ET* assessment. In our case, no images were available for September 2009 and July and September 2010. However, we proceeded with the proposed temporal upscaling methodology using previous satellite dates and ET_0 obtained at the SIAS meteorological station. Tables 5.7 and 5.8 show the period to which each image was referred.

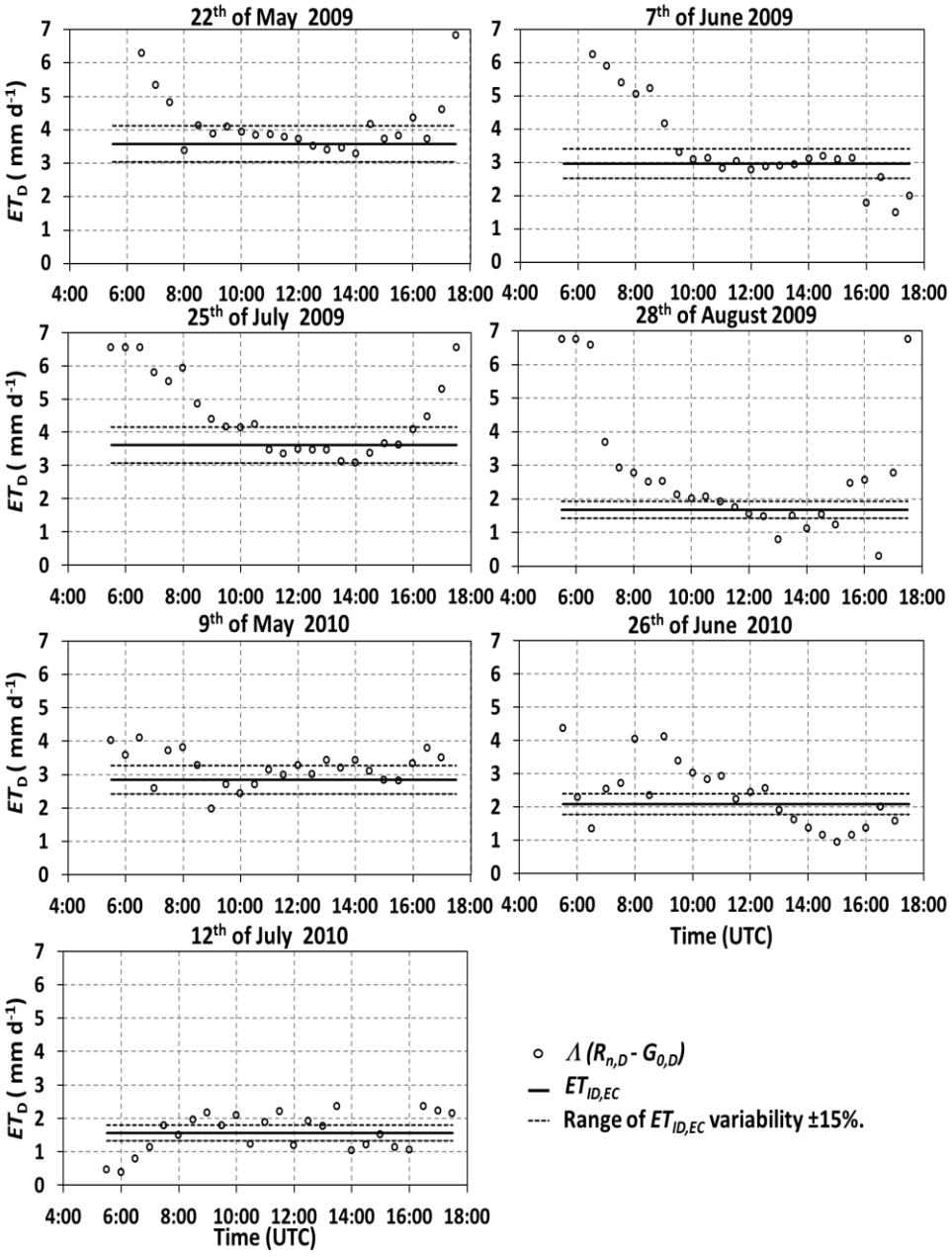

Figure 5.49: Acquisition days changes of Λ($R_{n,D}$-$G_{0,D}$) at time-step of 30 minutes, $ET_{ID,EC}$ measured by EC tower and accepted range of variability (±15%).

Table 5.7: Date of Landsat TM image acquisition and related periods during irrigation season 2009.

Date (dd/mm)	DOY	Initial day (dd/mm)	Final day (dd/mm)
22/05	142	15/05	31/05
07/06	158	01/06	30/06
25/07	206	01/07	31/07
26/08	238	01/08	30/09

Table 5.8: Date of Landsat TM image acquisition and related periods during irrigation season 2010.

Date (dd/mm)	DOY	Initial day (dd/mm)	Final day (dd/mm)
09/05	129	01/05	31/05
26/06	177	01/06	30/06
12/07	193	01/07	30/09

5.7 Validation of remote sensing SEBAL estimations with Eddy covariance data

The validation of SEBAL outputs was performed on the image acquisition days, using field measurement by the flux tower micrometeorological station. SEB turbulent fluxes of the pixel containing the flux tower were compared to eddy covariance turbulent fluxes.

Indeed, the turbulent fluxes measured by the FT are a function of the changes in the wind speed and direction. The wind affects also the position of the maximum fluxes contribution.

To be able to compare the results obtained from the application of the SEBAL model with those measured by Flux Tower, a simplification of this comparison is done using the distance determining the maximum contribution of fluxes, x_{max} (m). The x_{max} values was obtained from a previous doctorate thesis (Cammalleri C., 2011) following the approach proposed by Kormann and Meixner (2001) an explicit details on the

source area and footprint function detection can be found in section 3.1.3 of the thesis of Cammalleri C., (2011). The value of x_{max}, which is the distance in the upwind direction, shows values ranging between 3 and 23 m on daytime from 9:00 to 10:00 UTC for the considered years 2009 and 2010. This timing was taken into consideration since all the image were acquired within this time interval. The mean value of x_{max} was approximately 13.1 m with a standard deviation of ± 4.6 m, which means that the source area where originates maximum turbulent fluxes is always contained within the image pixel that contains the flux tower.

Figure 5.50 shows the comparison between the flux tower eddy covariance measured daily evapotranspiration ($ET_{ID,EC}$) and the daily SEBAL evapotranspiration ($ET_{a,ID}$) on the image acquisition days represented by the DOY. The dashes points the figure 5.48 represent the considered acceptable error of 15%.

As presented in figure 5.50, SEBAL model estimated ET accurately on the 22nd of May (DOY 142) and on the 7th of June (DOY 158) 2009 and on the 9th of May 2010 (DOY 129). While it overestimated the *ET* on the 26th of August 2009 (DOY 238) by 1.2 mm. It also overestimated the *ET* on the 26th of June (DOY 177) and 12th of July 2010 (DOY 193) by 0.89 and 0.83 mm, respectively. Finally, the SEBAL model underestimated *ET* by 1 mm on the 26th of July 2009 (DOY 206). The average error of SEBAL estimations was 0.7 mm for the year 2009 and 0.8 mm for the year 2010. Even though the error in *ET* estimation was higher than the acceptable range, it was not that much significant.

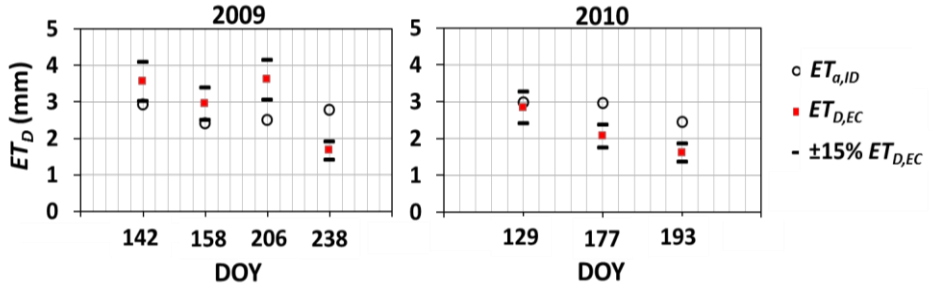

Figure 5.50: Eddy covariance measured evapotranspiration ($ET_{D,EC}$) and SEBAL estimated evapotranspiration ($ET_{D,SEBAL}$).

5.8 The validation of the ETD temporal upscaling into longer periods

The extrapolation of daily evapotranspiration ($ET_{a,ID}$) into longer periods is analyzed. $ET_{a,ID}$ was upscaled using the reference evapotranspiration (ET_0) obtained at the SIAS meteorological station. Theoretically changes in ET_0, thus in meteorological demand, are considered a proxy of the actual evapotranspiration changes with respect to the image acquisition time. Allen et al., 2007a proposed that at least 1 image per month should be available in this upscaling process. As shown previously in tables 5.7 and 5.8, only few images were appropriate for this application because of the presence of cloud cover hindering the SEBAL modeling. Due to this inconvenience, some images were set to cover a period longer than a month, thus, introducing inaccuracies in the estimation of ET over the period (according to Allen et al., 2007).

Figure 5.51 and 5.52 show the comparison between the flux tower cumulated daily evapotranspiration ($ET_{D,EC}$) *vs* SEBAL seasonally upscaled daily evapotranspiration (ET_D), as well as with the reference daily evapotranspiration (ET_0). The bar charts in reference to the secondary axis, represents the precipitation events during the considered seasons.

Figures below show that the extrapolation applied to fill the missing data between cloud-free satellite acquisitions is robust. A similar trend was detected between the extrapolated ET_D and the $ET_{D,EC.}$ However, the disposability of cloud-free images affects the applicability of the method, since a significant reduction in actual temporal resolution, increased the inaccuracies in extrapolating ET_D. In Figure 5.51, it was shown that in September 2009/2010, due to lack of scene cloud-free images, the extrapolation of ET_D resulted with considerable uncertainties. The acquisitions on DOY 238, 2009 and DOY 193, 2010 do not reflect the effects of the precipitations occurred during the month of September 2009 and 2010. However, this was not the case for August 2010 when starting from SEB applied on DOY 193 image, the trend of ET_D was estimated relatively accurately since no precipitation was recorded over the considered month. This result agrees with the approach proposed by Allen et al., (2007) and confirms a need of at least an image per month.

However, the approach fails in cases of significant rainfall or irrigation following the acquisition day (e.g., DOY 129 with a significant rainfall occurred the day after).

This effect is enhanced especially in water-stressed condition. However, over an area with intensive irrigation practice (similar to Spanish case study), the model hypothesis is valid since no stress is allowed and the crops are always at maximum evapotranspiration rate. These results coincide with Alfieri et al. (2017), for the need for more than one cloud-free image for accurate daily *ET* extrapolation. Alfieri et al. (2017) indicated that a return interval of no more than 5 days is necessary to accurately estimate $ET_{D.}$ Droogers et al. (2010) also indicated that water requirement can be accurately estimated, considering an interval of 15 days or shorter periods.

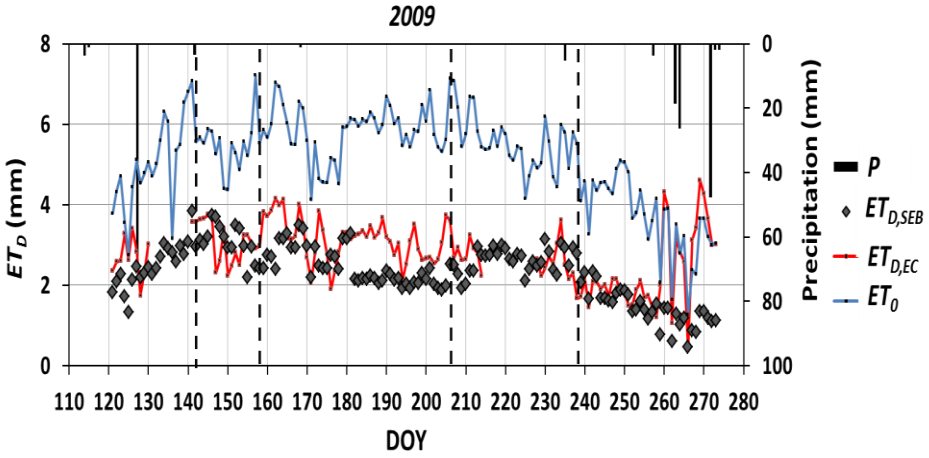

Figure 5.51: The 2009 season temporal distribution of *EC* measured evapotranspiration ($ET_{D,EC}$), temporally upscaled $ET_{D,SEBAL}$, Precipitation (*P*) and SIAS measured reference evapotranspiration (ET_0) (dashed lines represent image acquisition dates).

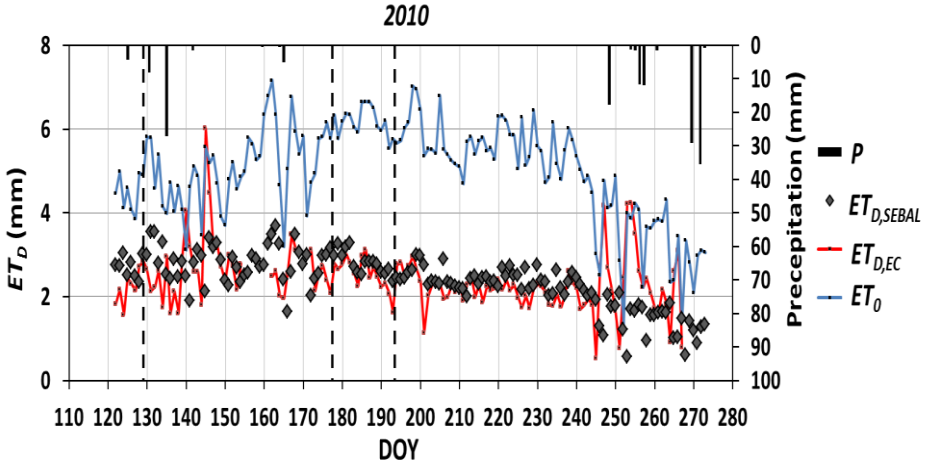

Figure 5.52: The 2010 season temporal distribution of *EC* measured evapotranspiration ($ET_{D,EC}$), temporally upscaled $ET_{D,SEBAL}$, Precipitation (*P*) and SIAS measured reference evapotranspiration (ET_0) (dashed lines represent image acquisition dates).

5.9 Evapotranspiration estimates by SEBAL model compared to the maximum evapotranspiration (ET_c)

The estimated SEBAL ET_D were upscaled to monthly values and compared to the maximum crop evapotranspiration (ET_c) obtained from the SIAS measured reference evapotranspiration (ET_0) and season dependent crop coefficients as addressed in the FAO Irrigation and Drainage Paper (Allen et al., 1998). The non-stressed, well-managed crops coefficients are demonstrated in table 5.9 where $K_{c,-in}$ represents the initial stages crop coefficient K_{c-mid} is the mid-season crop coefficient and K_{c-end} is the end season crop coefficient.

Table 5.9: FAO 56 single crop coefficients (Allen et al., 1998).

Crop	$K_{c\text{-ini}}$	K_{c-mid}	K_{c-end}
Grapevine	0.3	0.7	0.45
Olives	0.6	0.7	0.7

Knowing that the area is mainly cultivated by olives and grapevine, and managed under stress conditions, it was clear that the application performed in the Spanish case study could not be applied on the district 1A. However, comparing the model assessments, irrigation applied volumes and ET_c it is possible to give indication on the state of stress over the considered crops. The mean value of SEBAL instantaneous retrievals over identified grape vine and olive fields in the case study was taken into consideration. These values were upscaled using the self-preservation hypothesis and then compared on the image acquisition day to ET_c. Figures 5.53, 5.54, 5.55 and 5.56 report fields value of $ET_{a,ID}$ and ET_c representing managed evapotranspiration of a non-stressed well-managed crop. ET_c was retrieved from ET_0 using the season specific crop coefficients. Observing the following figures it was possible to indicate the level of stress in each field which gives an indication for farmers' irrigation practices. However, it was clear in the whole area, except for few fields, that the olive trees and grapevine grooves are cultivated under high levels of stress. An exception was the months of May 2009 and 2010, where the ET_c and $ET_{a,ID}$ were relatively similar.

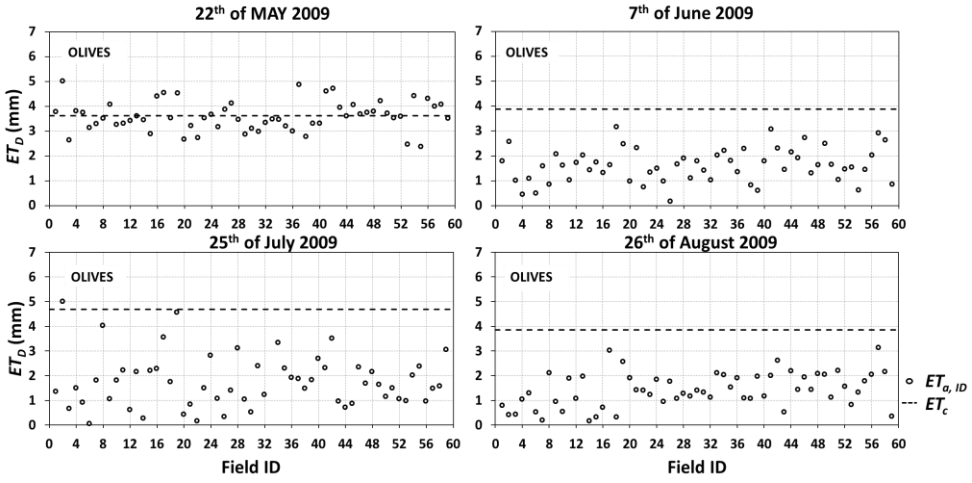

Figure 5.53: The SEBAL day of acquisition Retrieved ET_D vs the ET_c defined by the dashed line, Olives of season 2009.

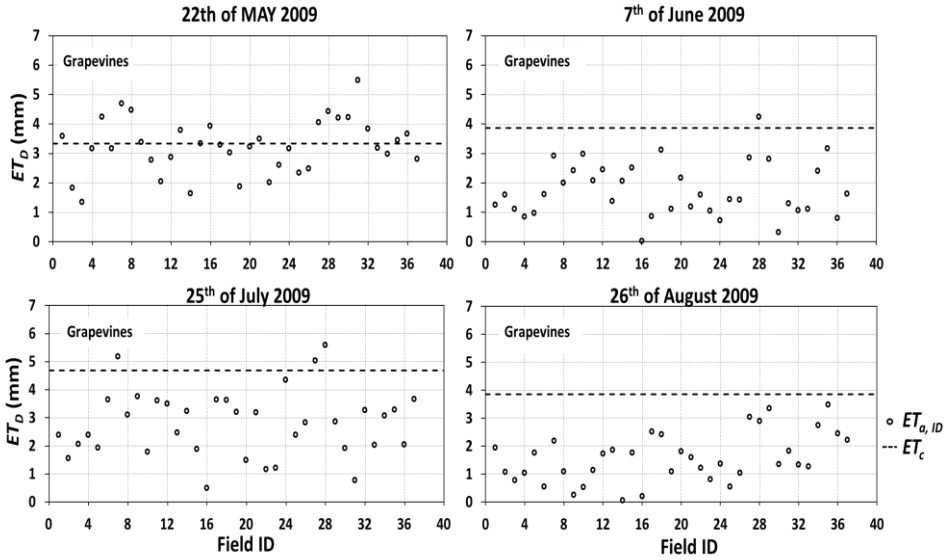

Figure 5.54: The SEBAL day of acquisition Retrieved ET_D vs the ET_c defined by the dashed line. Grape vines of season 2010.

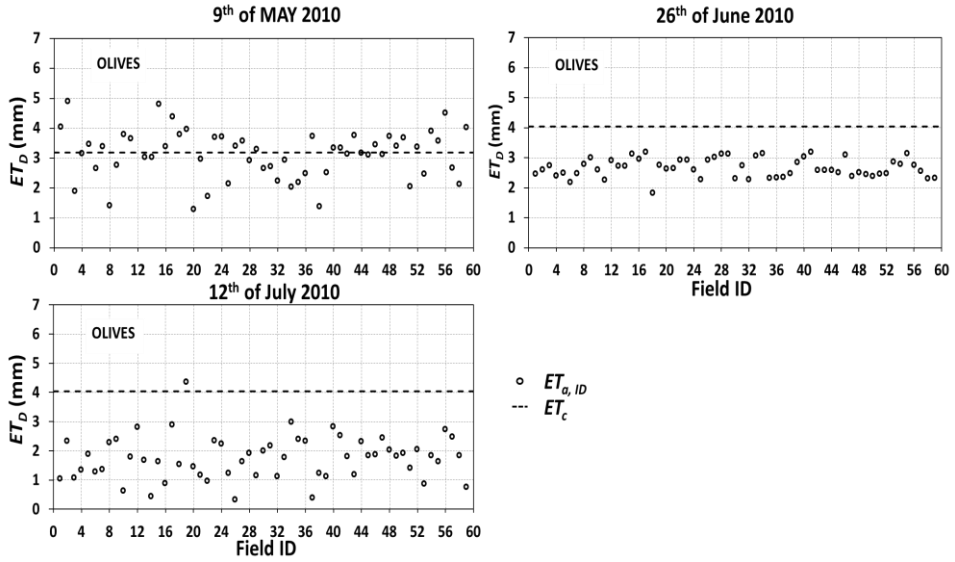

Figure 5.55: The SEBAL day of acquisition Retrieved ET_D vs the ET_c defined by the dashed line. Olives of season 2009.

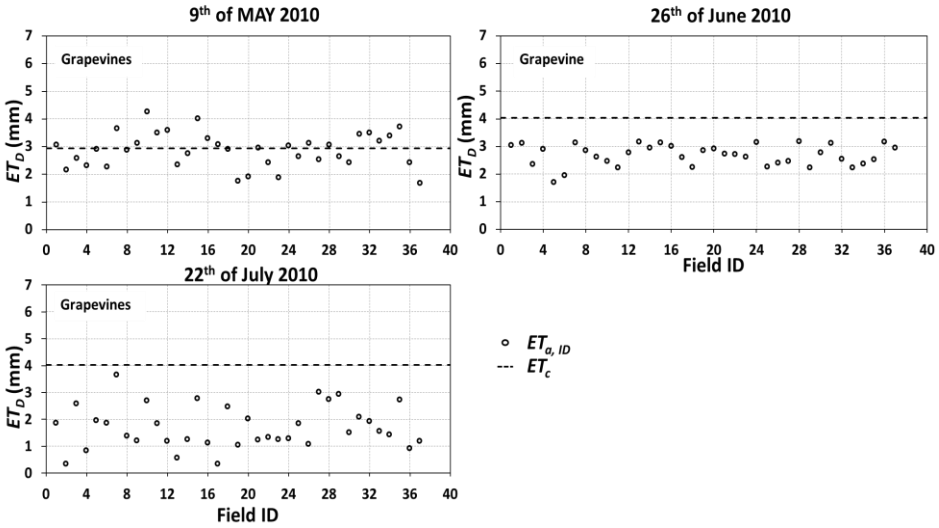

Figure 5.56: The SEBAL day of acquisition Retrieved ET_D vs the *ETc* defined by the dashed line. Grape vines of season 2010.

The estimated daily evapotranspiration was extrapolated to longer periods using the previously defined methodology. The on-field irrigation data were aggregated on the monthly scale for the two considered years (2009 and 2010). The obtained monthly retrievals were compared to monthly aggregated ET_c considering rainfall values and registered consumed irrigation water volumes. It was also demonstrated that farmers irrigate mainly on July, August and to a lesser extent on September. Non-significant irrigation volumes were registered in the remaining part of the season. Figure 5.57 shows the comparison between monthly extrapolated $ET_{monthly}$, monthly irrigation volumes (I) retrieved, $ET_{c,monthly}$ and the precipitation (P). The figure shows that in the irrigation district 1/A the water application is managed under relatively high stress with an exception on May 2009 and 2010.

This fact hinders further applications of SEBAL in an approach similar to that applied on the Spanish case study. In such conditions and, as mentioned before, the upscaled *ET* values between different acquisition cannot take into account irrigation practices and rainfall close to the acquisition date, especially when few images are set to cover a relatively long irrigation period. However, the instantaneous and daily retrievals of

SEBAL can be used as an index of vegetation stress on the day of image acquisition.

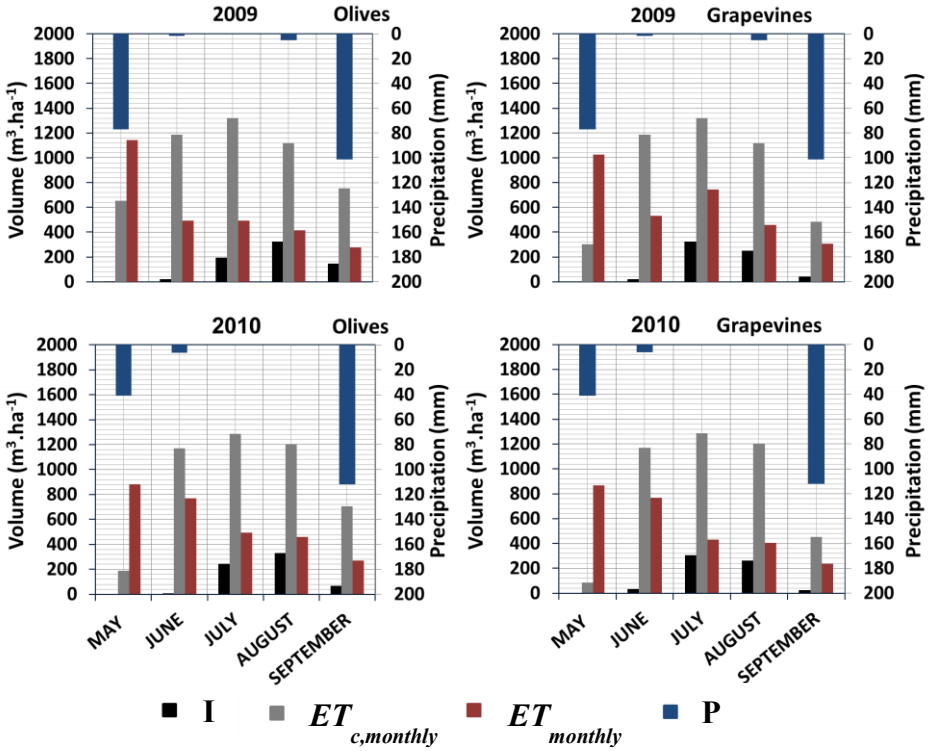

Figure 5.57: Comparison between $ET_{monthly}$ and $ET_{c,monthly}$, irrigation volumes (I) and precipitation (P)

Chapter 6: Conclusion

Accurate estimations of actual evapotranspiration, ET_a, play a key-role for irrigation water management and to monitor irrigation systems. At different scales of application, from fields to large districts, the knowledge of actual ET_a and its spatial distribution is crucial to optimize water and energy use in irrigation schemes. However, in-situ measurements of ET_a can be costly and time-consuming, especially for large scales of application. For these reasons and thanks to their great potential, Earth Observation and remote sensing techniques have been proposed as a valid alternative to describe the spatial distribution of surface evapotranspiration. Water user associations and national authorities commonly use the volumes of distributed water to assess irrigation system's performance, even if these measurements cannot account for the spatial variability of actual crop water requirements. In

single plots and/or in irrigation districts, linking water volumes delivered to the fields with estimations of remote sensed ET_a can have a great potential to develop new cost-effective indices of irrigation performance, as well as to reduce the waste of water.

Remote sensing based models were used to estimate the spatial and temporal distribution of ET_a over a landscape including various crops, soil physical characteristics and management practices. Landsat Thematic Mapper images were used to retrieve energy fluxes over two irrigation districts, the ''SAT Llano Verde'' irrigation district (Spain) and the district 1/A, in Italy, managed by the "Consorzio di Bonifica di Agrigento 3". Two remote sensing surface energy balance models, SEBAL and TSEB model, were used for ET_a spatial distribution retrieval. The latter, having the advantage of partitioning *ET* within the pixel, into soil and vegetation components, it was applied only to the Italian case study in which it is present sparse vegetation of arboreal plants (mainly olives and grapevines).

The SEBAL model was applied to both the Spanish and the Italian irrigation districts, even if outcomes were expected to be more reliable for the Spanish case characterized by homogeneous vegetation coverage.

The irrigation seasons were 2006-2007 and 2008 for the Spanish case; whereas two irrigation seasons (2009-2010) were taken into account for the Italian case study. These models allowed retrieving instantaneous ET_a spatial distribution that was then up-scaled to estimate daily values by assuming the self-preservation of the evaporative fraction. Daily acquisitions were finally employed to derive ET_a within longer periods by assuming a proportionality to temporal dynamics of the reference evapotranspiration (ET_0) computed using ground meteorological data.

The application of TSEB did not provide convincing results because of several factors, among which the high sensitivity of this method to uncertainties in satellite radiometric temperature retrievals as well as to the different input parameters necessary to run the model (canopy architecture and viewing geometry parameters).

Although in the Spanish case study accurate measurements to assess the model retrievals were missing, the SEBAL model was extensively validated in previously studies on this region by other researchers (Bastiaanssen et al., 1998).

On the other hand, in the irrigation district 1A (in Italy) the model retrieval were compared to eddy covariance fluxes measurements; thus allowing evaluating the reliability of the daily estimations and the upscaling approaches with particular attention to the analysis and interpretation of the temporal upscaling.

The flux tower 30 minutes data were analyzed to assess the diurnal changes of the evaporative fraction confirming that the self-preservation hypothesis was valid. The flux tower derived evaporative fraction was used to upscale instantaneous latent heat flux into daily values which were compared with the aggregated daily values, $ET_{D,EC}$. It was shown that at the time of image acquisitions interval (9:00 to 10:00 UTC) the evaporative fraction estimated successfully the daily *ET* within a range of acceptable error of ±15%.

The daily SEBAL estimates showed generally acceptable values when compared to the measured $ET_{D,EC}$ at the flux tower on the considered days. The flux tower data were also used to test the upscaling from daily- to the longer period-scales. It was shown that the up-scaled SEBAL retrievals followed the same trend of variation of the flux daily measured data. However, it was notable that this method of temporal upscaling couldn't take into account the preceding and successive precipitation events, which led to high uncertainties during May and September where significant amount of precipitation occurred; this is probably due to the long-time gaps between the acquisition days. Indeed, the effects of evapotranspiration from precipitation and irrigation events occurring in between satellite overpasses can be missed, and this lead to a significant bias in the temporal upscaling. This result coincided with other literature findings, where it was indicated that a return interval of no more than 5 days is necessary to accurately estimate the day to day changes of ET_D. However, finding determining an optimal acquisition rate is significantly complicated as it is connected to the availability of cloud-free images during the investigated period.

Up-scaling errors can reduce significantly the accuracy of *ET* long-term retrievals, which would hinder any application regarding the irrigation performance assessment. However, instantaneous and daily values can be a good indicator of the level of stress applied in the irrigation district. Comparing the *SEBAL* retrievals on acquisition days ($ET_{a,ID}$) to daily crop evapotranspiration (ET_c) obtained using the FAO 56 approach,

showed significant stress over the grapevines and olives of district 1/A, with an exception on the image acquisition on May where significant rainfall occurred.

The up-scaling can be theoretically valid under potential evapotranspiration conditions even with a single image acquisition per month, since in this case ET_0 is a good descriptor of actual ET variability. This was the case of the SAT Llano Verde irrigation district, characterized by dry climatic condition and intensive irrigation practices applied particularly to the horticultural crop cultivated in the region. It was confirmed from the irrigation managers that no stress was allowed on the crops cultivated in the region. In this case the model application allowed the comparison between the monthly registered water volumes downstream of each hydrant with the volume allocated to the evapotranspiration process, taking into consideration an irrigation efficiency of 85%. The above-mentioned comparison led to the possibility of assessing the irrigation performance at hydrant levels. In the Spanish case study, it was shown that the vast majority of farmers were applying an excess amount of water in comparison to SEBAL retrievals. An exception was the month of May where a significant amount of precipitation occurred. The comparison at the seasonal scale evidenced that a considerable amount of water, corresponding to 26.2, 28 and 16. 4% of total water consumption for the years 2006, 2007 and 2008 respectively, could have been saved.

In conclusion, it is possible to affirm that the latent heat flux estimated at the image acquisition time is a good descriptor of the actual vegetation water consumption. The upscaling over time allows to describe the actual ET temporal evolution where effective precipitation events or sufficient irrigation practice are applied. If crops are irrigated under a managed stress (like as in the Italian case study), the model fails to take into account preceding and succeeding effective rainfall or irrigation interventions; thus the periodic temporal upscaling fails to estimate accurately the real condition on those preceding or successive dates.

Finally, it was evidenced that some practical constraints are always present; a major drawback is that case-specific considerations need to be known prior to the application of some remote sensing based modeling approaches.

Further studies should be performed to assess the effect of the satellite cloud-free images availability on the temporal up-scaled outcomes.

Finally, In order to gain greater insight over problems related to the application of TSEB on the District 1/A case study, further analysis of the model sensitivity to surface remote sensing derived temperature and other modeling parameters is to be performed.

Among the prosperous potentials of Satellite RS, is the ability to observe large stretches of land and acquire worthwhile information that can be applied efficaciously in agro-hydrologic systems. If integrated with in situ irrigation data it can allow the monitoring of the irrigation performance at farm level and at large scale irrigation districts. However, it is to point out that these applications can become successful tools only if irrigation user associations were more involved in the exploitation of these novel technologies.

References

Allen, R. G., Pereira, L. S., Raes, D., & Smith, M. (1998). Crop evapotranspiration-Guidelines for computing crop water requirements-FAO Irrigation and drainage paper 56. *FAO, Rome*, *300*(9), D05109.

Allen, R. G., Tasumi, M., Trezza, R., Waters, R., & Bastiaanssen, W. (2002). SEBAL (Surface Energy Balance Algorithms for Land). *Advance Training and Users Manual–Idaho Implementation, version*, *1*, 97.

Allen, R. G., Tasumi, M., & Trezza, R. (2007). Satellite-based energy balance for mapping evapotranspiration with internalized calibration (METRIC)—Model. *Journal of irrigation and drainage engineering*, *133*(4), 380-394.

Allen, R. G., Tasumi, M., Morse, A., Trezza, R., Wright, J. L., Bastiaanssen, W., ... & Robison, C. W. (2007). Satellite-based energy

balance for mapping evapotranspiration with internalized calibration (METRIC)—Applications. *Journal of irrigation and drainage engineering*, *133*(4), 395-406.

Allen, R., Irmak, A., Trezza, R., Hendrickx, J. M., Bastiaanssen, W., & Kjaersgaard, J. (2011). Satellite-based ET estimation in agriculture using SEBAL and METRIC. *Hydrological Processes*, *25*(26), 4011-4027.

Anderson, M. C., Norman, J. M., Diak, G. R., Kustas, W. P., & Mecikalski, J. R. (1997). A two-source time-integrated model for estimating surface fluxes using thermal infrared remote sensing. *Remote sensing of environment*, *60*(2), 195-216.

Anderson, M. C., Kustas, W. P., & Norman, J. M. (2007). Upscaling flux observations from local to continental scales using thermal remote sensing. *Agronomy Journal*, *99*(1), 240-254.

Barsi, J. A., Barker, J. L., & Schott, J. R. (2003). An atmospheric correction parameter calculator for a single thermal band earth-sensing instrument. In *Geoscience and Remote Sensing Symposium, 2003. IGARSS'03. Proceedings. 2003 IEEE International* (Vol. 5, pp. 3014-3016). IEEE.

Barsi, J. A., Markham, B. L., Schott, J. R., Hook, S. J., & Raqueno, N. G. (2010, July). Twenty-five years of Landsat thermal band calibration. In *Geoscience and Remote Sensing Symposium (IGARSS), 2010 IEEE International* (pp. 2287-2290). IEEE.

Bastiaanssen, W. G., Menenti, M., Feddes, R. A., & Holtslag, A. A. M. (1998). A remote sensing surface energy balance algorithm for land (SEBAL). 1. Formulation. *Journal of hydrology*, *212*, 198-212.

Bastiaanssen, W. G., Pelgrum, H., Wang, J., Ma, Y., Moreno, J. F., Roerink, G. J., & Van der Wal, T. (1998). A remote sensing surface energy balance algorithm for land (SEBAL).: Part 2: Validation. *Journal of hydrology*, *212*, 213-229.

Bastiaanssen, W. G. M. (2000). SEBAL-based sensible and latent heat fluxes in the irrigated Gediz Basin, Turkey. *Journal of hydrology*, *229*(1), 87-100.

Bastiaanssen, W. G. M., Noordman, E. J. M., Pelgrum, H., Davids, G., Thoreson, B. P., & Allen, R. G. (2005). SEBAL model with remotely

sensed data to improve water-resources management under actual field conditions. *Journal of irrigation and drainage engineering*, *131*(1), 85-93.

Bhattarai, N., Shaw, S. B., Quackenbush, L. J., Im, J., & Niraula, R. (2016). Evaluating five remote sensing based single-source surface energy balance models for estimating daily evapotranspiration in a humid subtropical climate. *International Journal of Applied Earth Observation and Geoinformation*, 49, 75-86.

Bowen, I. S. (1926). The ratio of heat losses by conduction and by evaporation from any water surface. *Physical review*, *27*(6), 779.

Brutsaert, W., & Kustas, W. P. (1985). Evaporation and humidity profiles for neutral conditions over rugged hilly terrain. *Journal of climate and applied meteorology*, *24*(9), 915-923.

Brutsaert, W., & Sugita, M. (1992). Application of self-preservation in the diurnal evolution of the surface energy budget to determine daily evaporation. *Journal of Geophysical Research: Atmospheres*, *97*(D17), 18377-18382.

Brutsaert, W., & Chen, D. (1996). Diurnal variation of surface fluxes during thorough drying (or severe drought) of natural prairie. *Water Resources Research*, *32*(7), 2013-2019.

Beven, K. J. (2001). Rainfall-runoff modelling. *The primer*, 208-216. chapter Data for Rainfall-Runoff Modelling, 73-76. Wiley, Chichester. pp. 359.

Brutsaert, W. (2005).Evaporation In *Hydrology: an introduction*. Cambridge University Press. Cambridge, UK. ISBN: 13 978-0-521-82479-8, 605 pp.

Brutsaert, W. (2013). *Evaporation into the atmosphere: theory, history and applications* (Vol. 1). Springer Science & Business Media.

Cammalleri, C. (2011). Modelling water and energy balance of the land-atmosphere system*: A PHD thesis*. Università Degli Studi di Palermo, Palermo, Italia. https://iris.unipa.it/retrieve/handle/10447/95478/123287/Tesi_Dottorato_Cammalleri.pdf.

Campbell, G. S., & Norman, J. M. (2012). *An introduction to environmental biophysics*. Springer Science & Business Media.

Chávez, J. L., Neale, C. M., Prueger, J. H., & Kustas, W. P. (2008). Daily evapotranspiration estimates from extrapolating instantaneous airborne remote sensing ET values. *Irrigation Science*, *27*(1), 67-81.

Choi, M., Kustas, W. P., Anderson, M. C., Allen, R. G., Li, F., & Kjaersgaard, J. H. (2009). An intercomparison of three remote sensing-based surface energy balance algorithms over a corn and soybean production region (Iowa, US) during SMACEX. *Agricultural and Forest Meteorology*, *149*(12), 2082-2097.

Choudhury, B. J., Idso, S. B., & Reginato, R. J. (1987). Analysis of an empirical model for soil heat flux under a growing wheat crop for estimating evaporation by an infrared-temperature based energy balance equation. *Agricultural and Forest Meteorology*, *39*(4), 283-297.

Choudhury, B. J., & Monteith, J. L. (1988). A four-layer model for the heat budget of homogeneous land surfaces. *Quarterly Journal of the Royal Meteorological Society*, *114*(480), 373-398.

Choudhury, B. J., Ahmed, N. U., Idso, S. B., Reginato, R. J., & Daughtry, C. S. (1994). Relations between evaporation coefficients and vegetation indices studied by model simulations. *Remote sensing of environment*, *50*(1), 1-17.

Ciraolo, G., D'Urso, G., & Minacapillic, M. (2006, September). Actual evapotranspiration estimation by means of airborne and satellite remote sensing data. In *Proc. of SPIE Vol* (Vol. 6359, pp. 63590Y-1).

Chirouze, J., Boulet, G., Jarlan, L., Fieuzal, R., Rodriguez, J. C., Ezzahar, J., ... & Watts, C. (2014). Intercomparison of four remote-sensing-based energy balance methods to retrieve surface evapotranspiration and water stress of irrigated fields in semi-arid climate. *Hydrology and Earth System Sciences Discussions*, (18), 1165-1188.

Colaizzi, P. D., Kustas, W. P., Anderson, M. C., Agam, N., Tolk, J. A., Evett, S. R., & O'Shaughnessy, S. A. (2012). Two-source energy balance model estimates of evapotranspiration using component and composite surface temperatures. *Advances in water resources*, *50*, 134-151.

Colombo, R., Bellingeri, D., Fasolini, D., & Marino, C. M. (2003). Retrieval of leaf area index in different vegetation types using high resolution satellite data. *Remote Sensing of Environment*, *86*(1), 120-131.

Colwell, J. E. (1974). Vegetation canopy reflectance. *Remote sensing of environment*, *3*(3), 175-183.

Courault, D., Demarez, V., Guérif, M., Le Page, M., Simonneaux, V., Ferrant, S., & Veloso, A. (2017). Contribution of remote sensing for crop and water monitoring. In *Land Surface Remote Sensing in Agriculture and Forest* (pp. 113-177).

Cragoa, R., & Brutsaert, W. (1996). Daytime evaporation and the self-preservation of the evaporative fraction and the Bowen ratio. *Journal of Hydrology*, *178*(1-4), 241-255.

Crow, W. T., & Kustas, W. P. (2005). Utility of assimilating surface radiometric temperature observations for evaporative fraction and heat transfer coefficient retrieval. *Boundary-layer meteorology*, *115*(1), 105-130.

Culf, A. D., Foken, T., & Gash, J. H. (2004). The energy balance closure problem. In *Vegetation, water, humans and the climate* (pp. 159-166). Springer Berlin Heidelberg.

D'Urso, G. (2001). *Simulation and management of on-demand irrigation systems: a combined agrohydrological and remote sensing approach. Monography, Wageningen University*. ISBN 90-5808-399-3,174 pp.

Droogers, P., Immerzeel, W. W., & Lorite, I. J. (2010). Estimating actual irrigation application by remotely sensed evapotranspiration observations. *Agricultural Water Management*, *97*(9), 1351-1359.

FAO, F., & Organisation, A. (2011). The State of the World's Land and Water Resources for Food and Agriculture. *Managing systems at risk. Rome/London: FAO/Earthscan*.

Finnigan, J. J. (2004). A re-evaluation of long-term flux measurement techniques part II: coordinate systems. *Boundary-Layer Meteorology*, *113*(1), 1-41.

Fisher, J. B., Melton, F., Middleton, E., Hain, C., Anderson, M., Allen, R., ... & Kilic, A. (2017). The future of evapotranspiration: Global requirements for ecosystem functioning, carbon and climate feedbacks,

agricultural management, and water resources. Water Resources Research, 53(4), 2618-2626.

Foken, T., & Wichura, B. (1996). Tools for quality assessment of surface-based flux measurements. *Agricultural and forest meteorology*, *78*(1), 83-105.

Foken, T., Wimmer, F., Mauder, M., Thomas, C., & Liebethal, C. (2006). Some aspects of the energy balance closure problem. *Atmospheric Chemistry and Physics*, *6*(12), 4395-4402.

Foken, T. (2008). The energy balance closure problem: an overview. *Ecological Applications*, *18*(6), 1351-1367.

French, A. N., Jacob, F., Anderson, M. C., Kustas, W. P., Timmermans, W., Gieske, A., & Prueger, J. (2005). Surface energy fluxes with the Advanced Spaceborne Thermal Emission and Reflection radiometer (ASTER) at the Iowa 2002 SMACEX site (USA). *Remote Sensing of Environment*, *99*(1-2), 55-65.

Garner, B. j., and Ohmura, A. 1968. *A method of calculating the direct shortwave radiation income of slopes. Joumal of Applied Meteorology*, *7*(5), 796-800.

Gates, D.M., (1980). Biophysical Ecology, Springer-Verlag, New York, p. 26.

Gentine, P., Entekhabi, D., Chehbouni, A., Boulet, G., & Duchemin, B. (2007). Analysis of evaporative fraction diurnal behaviour. *Agricultural and forest meteorology*, *143*(1), 13-29.

Gieske, A. (2003). The iterative flux-profile method for remote sensing applications. *International Journal of Remote Sensing*, *24*(16), 3291-3310.

Goetz, S. J., Halthore, R. N., Hall, F. G., & Markham, B. L. (1995). Surface temperature retrieval in a temperate grassland with multiresolution sensors. *Journal of Geophysical Research: Atmospheres*, *100*(D12), 25397-25410.

Goody, R.M., (1964). Atmospheric Radiation, Oxford University Press, Oxford, 1964.

Goody, R. M. (1952). A statistical model for water-vapour absorption. *Quarterly Journal of the Royal Meteorological Society*, *78*(336), 165-169.

Goudriaan, J. (1977). *Crop micrometeorology: a simulation study* (Doctoral dissertation, Pudoc).

Hoedjes, J. C. B., Chehbouni, A., Jacob, F., Ezzahar, J., & Boulet, G. (2008). Deriving daily evapotranspiration from remotely sensed instantaneous evaporative fraction over olive orchard in semi-arid Morocco. *Journal of Hydrology*, *354*(1), 53-64.

Howell, T. A. (2001). Enhancing water use efficiency in irrigated agriculture. *Agron J*, *93*, 281-289.

Huckseflux Model HFP01SC Self-Calibrating Soil Heat Flux Plate, Revision: 8/12. Available online: http://s.campbellsci.com/documents/af/manuals/hfp01sc.pdf (accessed October 2017).

Huntingford, C., Verhoef, A., & Stewart, J. (2000). Dual versus single source models for estimating surface temperature of African savannah. *Hydrology and Earth System Sciences Discussions*, *4*(1), 185-191.

lfieri, J. G., Anderson, M. C., Kustas, W. P., & Cammalleri, C. (2017). Effect of the revisit interval and temporal upscaling methods on the accuracy of remotely sensed evapotranspiration estimates. *Hydrology and Earth System Sciences*, *21*(1), 83.

Jackson, R. D., Hatfield, J. L., Reginato, R. J., Idso, S. B., & Pinter, P. J. (1983). Estimation of daily evapotranspiration from one time-of-day measurements. *Agricultural Water Management*, *7*(1-3), 351-362.

Jin, Y., Schaaf, C. B., Gao, F., Li, X., Strahler, A. H., Zeng, X., & Dickinson, R. E. (2002). How does snow impact the albedo of vegetated land surfaces as analyzed with MODIS data?. *Geophysical Research Letters*, *29*(10).

Khadra, R., Moreno, M. A., Awada, H., & Lamaddalena, N. (2016). Energy and hydraulic performance-based management of large-scale pressurized irrigation systems. *Water resources management*, *30*(10), 3493-3506.

Khanal, S., Fulton, J., & Shearer, S. (2017). An overview of current and potential applications of thermal remote sensing in precision agriculture. *Computers and Electronics in Agriculture*, *139*, 22-32.

Kimes, D. S. (1984). Modeling the directional reflectance from complete homogeneous vegetation canopies with various leaf-orientation distributions. *JOSA A*, *1*(7), 725-737.

Kormann, R., & Meixner, F. X. (2001). An analytical footprint model for non-neutral stratification. Boundary-Layer Meteorology, 99(2), 207-224.

Kotchenova, S. Y., Vermote, E. F., Matarrese, R., & Klemm Jr, F. J. (2006). Validation of a vector version of the 6S radiative transfer code for atmospheric correction of satellite data. Part I: Path radiance. *Applied optics*, *45*(26), 6762-6774.

Kotchenova, S. Y., & Vermote, E. F. (2007). Validation of a vector version of the 6S radiative transfer code for atmospheric correction of satellite data. Part II. Homogeneous Lambertian and anisotropic surfaces. *Applied optics*, *46*(20), 4455-4464.

Kotchenova, S. Y., Vermote, E. F., Levy, R., & Lyapustin, A. (2008). Radiative transfer codes for atmospheric correction and aerosol retrieval: intercomparison study. *Applied Optics*, *47*(13), 2215-2226.

Kustas, W. P. (1990). Estimates of evapotranspiration with a one-and two-layer model of heat transfer over partial canopy cover. *Journal of Applied Meteorology*, *29*(8), 704-715.

Kustas, W. P., & Norman, J. M. (1996). Use of remote sensing for evapotranspiration monitoring over land surfaces. *Hydrological Sciences Journal*, *41*(4), 495-516.

Kustas, W. P., & Norman, J. M. (1997). A two-source approach for estimating turbulent fluxes using multiple angle thermal infrared observations. *Water Resources Research*, *33*(6), 1495-1508.

Kustas, W. P., & Norman, J. M. (1999). Evaluation of soil and vegetation heat flux predictions using a simple two-source model with radiometric temperatures for partial canopy cover. *Agricultural and Forest Meteorology*, *94*(1), 13-29.

Kustas, W. P., Norman, J. M., Anderson, M. C., & French, A. N. (2003). Estimating subpixel surface temperatures and energy fluxes from the

vegetation index–radiometric temperature relationship. *Remote sensing of environment*, *85*(4), 429-440.

Kustas, W. P., Norman, J. M., Schmugge, T. J., & Anderson, M. C. (2004). Mapping surface energy fluxes with radiometric temperature. *Thermal remote sensing in land surface processes*, 205-253.

Kustas, W., & Anderson, M. (2009). Advances in thermal infrared remote sensing for land surface modeling. *Agricultural and Forest Meteorology*, *149*(12), 2071-2081.

Larcher, W., (1983). Physiological Plant Ecology, corrected printing of the 2nd Edition, translated by M.A. Biederman-Thorson, Springer-Verlag, New York, p. 20.

Liang, S. (2004). Estimation of Surface Radiation Budget: II. Longwave. *Quantitative Remote Sensing of Land Surfaces*, 345-397.

Liu, H., Peters, G., & Foken, T. (2001). New equations for sonic temperature variance and buoyancy heat flux with an omnidirectional sonic anemometer. *Boundary-Layer Meteorology*, *100*(3), 459-468.

LSASAF., (2008).Vegetation parameters (FVC, LAI, FAPAR): product user manual. Version 2.1.

Malkmus, W. (1967). Random Lorentz band model with exponential-tailed S− 1 line-intensity distribution function. *JOSA*, *57*(3), 323-329.

Maltese, A., Capodicia, F., Ciraoloa, G., La Loggiaa, G., & Rallob, G. (2013, October). Assessing daily actual evapotranspiration through energy balance: an experiment to evaluate the self-preservation hypothesis with acquisition time. In *Proc. of SPIE Vol* (Vol. 8887, pp. 888718-1).

Markham, B. L., Boncyk, W. C., Helder, D. L., & Barker, J. L. (1997). Landsat-7 enhanced thematic mapper plus radiometric calibration. *Canadian Journal of Remote Sensing*, *23*(4), 318-332.

Markham, B. L. (1986). Landsat MSS and TM post-calibration dynamic ranges, exoatmospheric reflectances and at-satellite temperatures. *Landsat Technical Notes*, (1), 3-8.

Markham, B. L., Boncyk, W. C., Helder, D. L., & Barker, J. L. (1997). Landsat-7 enhanced thematic mapper plus radiometric calibration. *Canadian Journal of Remote Sensing*, *23*(4), 318-332.

Menenti, M., Visser, T. N. M., Morabito, J. A., & Drovandi, A. (1989). Appraisal of irrigation performance with satellite data and georeferenced information. *Irrigation Theory and Practice*, 785-801.

Minacapilli M, Agnese C, Blanda F, Cammalleri C, Ciraolo G, D'Urso G, Iovino M, Pumo D, Provenzano G, Rayo G., (2009). Estimation of actual evapotranspiration of Mediterranean perennial crops by means of remote-sensing based surface energy balance models. *Hydrology and Earth System Sciences*, *13*(7), 1061-1074.

Miller, J. B. (1967). A formula for average foliage density. *Australian Journal of Botany*, *15*(1), 141-144.

Moran, M. S., & Jackson, R. D. (1991). Assessing the spatial distribution of evapotranspiration using remotely sensed inputs. *Journal of Environmental Quality*, *20*(4), 725-737.

Morse, A., Tasumi, M., Allen, R. G., & Kramber, W. J. (2000). Application of the SEBAL methodology for estimating consumptive use of water and streamflow depletion in the Bear River Basin of Idaho through remote sensing. *Idaho Department of Water Resources–University of Idaho*.

Moncrieff, J., Clement, R., Finnigan, J., & Meyers, T. (2004). Averaging, detrending, and filtering of eddy covariance time series. In *Handbook of micrometeorology* (pp. 7-31). Springer, Dordrecht.

Monteith, J. L., & Unsworth, M. H. (1990). The radiation environment. *Principles of environmental physics, 2nd ed., Edward Arnold, London*, 36-57.

Robinson, N. (1966). Solar radiation. *Elsevier,*. Amsterdam/London/NY, USA

Nichols, W. E., & Cuenca, R. H. (1993). Evaluation of the evaporative fraction for parameterization of the surface energy balance. *Water Resources Research*, *29*(11), 3681-3690.

Norman, J. M., Kustas, W. P., & Humes, K. S. (1995). Source approach for estimating soil and vegetation energy fluxes in observations of

directional radiometric surface temperature. *Agricultural and Forest Meteorology*, *77*, 263-293.

Ortega, J. F., De Juan, J. A., & Tarjuelo, J. M. (2005). Improving water management: The irrigation advisory service of Castilla-La Mancha (Spain). *Agricultural Water Management*, *77*(1), 37-58.

Panin, G. N., Tetzlaff, G., & Raabe, A. (1998). Inhomogeneity of the Land Surface and Problems in the Parameterization of Surface Fluxes in Natural Conditions. *Theoretical and Applied Climatology*, *60*(1), 163-178.

Paulson, C. A. (1970). The mathematical representation of wind speed and temperature profiles in the unstable atmospheric surface layer. *Journal of Applied Meteorology*, *9*(6), 857-861.

Pereira, L. S., Allen, R. G., Smith, M., & Raes, D. (2015). Crop evapotranspiration estimation with FAO56: Past and future. *Agricultural Water Management*, *147*, 4-20.

Prata, A. J., Caselles, V., Coll, C., Sobrino, J. A., & Ottle, C. (1995). Thermal remote sensing of land surface temperature from satellites: Current status and future prospects. *Remote Sensing Reviews*, *12*(3-4), 175-224.

Priestley, C. H. B., & Taylor, R. J. (1972). On the assessment of surface heat flux and evaporation using large-scale parameters. *Monthly weather review*, *100*(2), 81-92.

Prueger, J. H., Hatfield, J. L., Parkin, T. B., Kustas, W. P., Hipps, L. E., Neale, C. M. U., ... & Cooper, D. I. (2005). Tower and aircraft eddy covariance measurements of water vapor, energy, and carbon dioxide fluxes during SMACEX. *Journal of Hydrometeorology*, *6*(6), 954-960.

Rinaldi, M., & He, Z. (2014). Decision support systems to manage irrigation in agriculture. *Adv. Agron*, *123*, 229-279.

Roerink, G. J., Su, Z., & Menenti, M. (2000). S-SEBI: A simple remote sensing algorithm to estimate the surface energy balance. *Physics and Chemistry of the Earth, Part B: Hydrology, Oceans and Atmosphere*, 25(2), 147-157.

Ross, J. (2012). *The radiation regime and architecture of plant stands* (Vol. 3). Springer Science & Business Media.

Rouse Jr, J. W., Haas, R. H., Deering, D. W., Schell, J. A., & Harlan, J. C. (1974). Monitoring the Vernal Advancement and Retrogradation (Green Wave Effect) of Natural Vegetation.[Great Plains Corridor].

Sauer, T. J., Norman, J. M., Tanner, C. B., & Wilson, T. B. (1995). Measurement of heat and vapor transfer coefficients at the soil surface beneath a maize canopy using source plates. *Agricultural and forest meteorology*, *75*(1-3), 161-189.

Schotanus, P., Nieuwstadt, F., & De Bruin, H. A. R. (1983). Temperature measurement with a sonic anemometer and its application to heat and moisture fluxes. *Boundary-Layer Meteorology*, *26*(1), 81-93

Senay, G. B., Bohms, S., Singh, R. K., Gowda, P. H., Velpuri, N. M., Alemu, H., & Verdin, J. P. (2013). Operational evapotranspiration mapping using remote sensing and weather datasets: A new parameterization for the SSEB approach. JAWRA *Journal of the American Water Resources Association*, 49(3), 577-591.

Senay, G. B., Schauer, M., Friedrichs, M., Velpuri, N. M., & Singh, R. K. (2017). Satellite-based water use dynamics using historical Landsat data (1984–2014) in the southwestern United States. *Remote Sensing of Environment*.

Sharma, A. R., Badarinath, K. V. S., & Roy, P. S. (2009). Comparison of ground reflectance measurement with satellite derived atmospherically corrected reflectance: A case study over semi-arid landscape. *Advances in Space Research*, *43*(1), 56-64.

Shuttleworth, W. J., & Gurney, R. J. (1990). The theoretical relationship between foliage temperature and canopy resistance in sparse crops. *Quarterly Journal of the Royal Meteorological Society*, *116*(492), 497-519.

Shuttleworth, W. J., Gurney, R. J., Hsu, A. Y., & Ormsby, J. P. (1989). FIFE: the variation in energy partition at surface flux sites. *IAHS Publ*, *186*(6).

Singh, R. K., & Senay, G. B. (2015). Comparison of four different energy balance models for estimating evapotranspiration in the Midwestern United States. *Water*, *8*(1), 9.

Sobolev, V. V. (1975). Light scattering in planetary atmospheres. *(Translation of Rasseianie sveta v atmosferakh planet, Moscow, Izdatel'stvo Nauka, 1972.) Oxford and New York, Pergamon Press (International Series of Monographs in Natural Philosophy. Volume 76), 1975. 263 p.*

Somma, G. (2003). *Synergistic use of energy and water balance approaches for improved hydrological modelling over heterogeneous agricultural landscapes in water scarce areas* (Doctoral dissertation, PhD thesis, Università Federico II, Naples (Italy), 158 pp).

Starks, P. J., Norman, J. M., Blad, B. L., Walter-Shea, E. A., & Walthall, C. L. (1991). Estimation of shortwave hemispherical reflectance (albedo) from bidirectionally reflected radiance data. *Remote sensing of Environment*, *38*(2), 123-134.

Steltzer, H., & Welker, J. M. (2006). Modeling the effect of photosynthetic vegetation properties on the NDVI–LAI relationship. *Ecology*, *87*(11), 2765-2772.

Stewart, J. B., Engman, E. T., Feddes, R. A., & Kerr, Y. H. (1998). Scaling up in hydrology using remote sensing: summary of a Workshop.

Su, Z. (2002). The Surface Energy Balance System (SEBS) for estimation of turbulent heat fluxes. Hydrology and earth system sciences, 6(1), 85-100.

Sugita, M., & Brutsaert, W. (1990). Regional surface fluxes from remotely sensed skin temperature and lower boundary layer measurements. *Water Resources Research*, *26*(12), 2937-2944.

Tachiiri, K. (2005). Calculating NDVI for NOAA/AVHRR data after atmospheric correction for extensive images using 6S code: a case study in the Marsabit District, Kenya. *ISPRS journal of photogrammetry and remote sensing*, *59*(3), 103-114.

Tasumi, M., Allen, R. G., & Trezza, R. (2008). At-surface reflectance and albedo from satellite for operational calculation of land surface energy balance. *Journal of hydrologic engineering*, *13*(2), 51-63.

Thom, A. S. (1971). Momentum absorption by vegetation. *Quarterly Journal of the Royal Meteorological Society*, *97*(414), 414-428.

Timmermans, W. J., Kustas, W. P., Anderson, M. C., & French, A. N. (2007). An intercomparison of the surface energy balance algorithm for land (SEBAL) and the two-source energy balance (TSEB) modeling schemes. *Remote Sensing of Environment*, *108*(4), 369-384.

Toureiro, C., Serralheiro, R., Shahidian, S., & Sousa, A. (2017). Irrigation management with remote sensing: Evaluating irrigation requirement for maize under Mediterranean climate condition. *Agricultural Water Management*, *184*, 211-220.

Troufleau, D., Lhomme, J. P., Monteny, B., & Vidal, A. (1997). Sensible heat flux and radiometric surface temperature over sparse Sahelian vegetation. I. An experimental analysis of the kB− 1 parameter. *Journal of Hydrology*, *188*, 815-838.

Twine, T. E., Kustas, W. P., Norman, J. M., Cook, D. R., Houser, P., Meyers, T. P., ... & Wesely, M. L. (2000). Correcting eddy-covariance flux underestimates over a grassland. *Agricultural and Forest Meteorology*, *103*(3), 279-300.

Van de Griend, A. A., & Owe, M. (1993). On the relationship between thermal emissivity and the normalized difference vegetation index for natural surfaces. *International Journal of remote sensing*, *14*(6), 1119-1131.

Van Wijk, M. T., & Williams, M. (2005). Optical instruments for measuring leaf area index in low vegetation: application in arctic ecosystems. *Ecological Applications*, *15*(4), 1462-1470.

Vermote, E. F., Tanré, D., Deuze, J. L., Herman, M., & Morcette, J. J. (1997). Second simulation of the satellite signal in the solar spectrum, 6S: An overview. *IEEE transactions on geoscience and remote sensing*, *35*(3), 675-686.

Vermote, E., Tanré, D., Deuzé, J. L., Herman, M., Morcrette, J. J., & Kotchenova, S. Y. (2006a). Second Simulation of a Satellite Signal in the Solar Spectrum—Vector (6SV); 6S User Guide Version 3. *NASA Goddard Space Flight Center: Greenbelt, MD, USA*.

Vermote, E. F., & Saleous, N. (2006b). Operational atmospheric correction of MODIS visible to middle infrared land surface data in the

case of an infinite Lambertian target. In *Earth Science Satellite Remote Sensing* (pp. 123-153). Springer, Berlin, Heidelberg.

Wagle, P., Bhattarai, N., Gowda, P. H., & Kakani, V. G. (2017). Performance of five surface energy balance models for estimating daily evapotranspiration in high biomass sorghum. ISPRS Journal of Photogrammetry and Remote Sensing, 128, 192-203.

Webb, E. K. (1970). Profile relationships: The log-linear range, and extension to strong stability. *Quarterly Journal of the Royal Meteorological Society*, *96*(407), 67-90.

Webb, E. K., Pearman, G. I., & Leuning, R. (1980). Correction of flux measurements for density effects due to heat and water vapour transfer. *Quarterly Journal of the Royal Meteorological Society*, *106*(447), 85-100.

Wilson, K., Goldstein, A., Falge, E., Aubinet, M., Baldocchi, D., Berbigier, P., & Grelle, A. (2002). Energy balance closure at FLUXNET sites. *Agricultural and Forest Meteorology*, *113*(1), 223-243.

Yang, Y., & Shang, S. (2013). A hybrid dual source scheme and trapezoid framework–based evapotranspiration model (HTEM) using satellite images: Algorithm and model test. *Journal of Geophysical Research: Atmospheres*, 118(5), 2284-2300.

Zdunkowski, W. G., Welch, R. M., & Korb, G. (1980). An investigation of the structure of typical two-stream-methods for the calculation of solar fluxes and heating rates in clouds. *Beiträge zur Physik der Atmosphäre*, *53*(2), 147-166.

Zhang, L., & Lemeur, R. (1995). Evaluation of daily evapotranspiration estimates from instantaneous measurements. *Agricultural and Forest Meteorology*, *74*(1), 139-154.

UNIVERSITÀ DEGLI STUDI DI PALERMO

DIPARTIMENTO DI INGEGNERIA CIVILE, AMBIENTALE, AEROSPAZIALE, DEI MATERIALI

PALERMO
FEBRUARY/2018